UCLA
UCLA Electronic Theses and Dissertations

Title

Electrochemical Control for Extracellular Microenvironments with High Spatiotemporal Resolutions

Permalink

https://escholarship.org/uc/item/7sz9k14p

Author

Wang, Jingyu

Publication Date

2024

Peer reviewed|Thesis/dissertation

eScholarship.org Powered by the California Digital Library
University of California

UNIVERSITY OF CALIFORNIA

Los Angeles

Electrochemical Control for Extracellular Microenvironments with High Spatiotemporal Resolutions

A dissertation submitted in partial satisfaction

of the requirements for the degree Doctor of Philosophy in Chemistry

by

Jingyu Wang

2024

© Copyright by

Jingyu Wang

2024

ABSTRACT OF THE DISSERTATION

Electrochemical Control for Extracellular Microenvironments

with High Spatiotemporal Resolutions

by

Jingyu Wang

Doctor of Philosophy in Chemistry

University of California, Los Angeles, 2024

Professor Chong Liu, Chair

Microorganisms often exist in complex assemblages, where chemical gradients play a crucial role in influencing their metabolic processes. These gradients, resulting from endogenous microbial activities, involve a dynamic transfer of nutrients, signaling molecules, and metabolic waste. Understanding the effects of such gradients on microbial physiology is important for advancing our knowledge of microbial systems. Traditional methods for creating artificial microenvironments to study these interactions, such as chamber systems, pipette injection, hydrogels, and microfluidic devices, have provided significant insights in the physiological heterogeneity in the microbial systems. However, existing platforms are limited by their spatial resolution and temporal response times. My research aims to improve the spatiotemporal

resolution of artificial microenvironments by developing a novel biocompatible electrochemical platform for the generation and regulation of chemical gradients. Leveraging the fast and controllable kinetics of electrochemistry, this platform will allow for higher resolution and quicker response times compared to conventional methods. Through meticulous electrochemical design and advanced simulation guidance, I have established and optimized the electrochemical platforms for controllable gradients of oxygen (O_2), hydrogen peroxide (H_2O_2) and pH.

My first research project focused on the electrochemical control of O_2 and H_2O_2 gradients (**Chapter 2**). O_2 and H_2O_2 as one of reactive oxygen species (ROS) are two critical biologically relevant species in extracellular microenvironment. To artificially creating O_2 and H_2O_2 gradients, I performed electrochemical oxygen reduction catalyzed by Au and Pt deposition layer on Si microwire arrays. Microwire electrodes allowed for customized morphology, facilitating the exploration of the relationship between the electrode morphology and the gradient profiles. However, the inverse design of the desired gradients is still challenging considering the large variations of extracellular O_2 and H_2O_2 gradients in different microbial systems. To address this challenge, a machine learned based inverse design strategy was developed to quickly program a desired concentration profile at the microscopic level. Finite element method (FEM) models and machine learning algorithms were integrated to corelated the electrochemical parameters with the gradient profiles, and the targeted microenvironments of O_2 and H_2O_2 generated through inverse design was experimentally validated. The concept of the inverse design assisted by artificial intelligence was demonstrated on both O_2 and H_2O_2 gradients, enhancing our ability to understand and control extracellular spaces with precise spatiotemporal resolution.

With the success in O_2 and H_2O_2 gradients, my research was extended to the investigation of pH microenvironment (**Chapter 3**). pH, which reflects the local proton availability, is a critical factor

in biological metabolism and physiology. To achieve a controllable pH gradient through electrochemical strategy, a proton-coupled electron transfer reaction (PCET) was meticulously designed and evaluated. Instead of using microwire electrodes, interdigitated electrodes consisting of a pair of microelectrode array strips was used to provide more flexibility in tuning the range and slope of the pH gradients. Key parameters, including oxidation and reduction potential, the gap between electrodes, and the electrolyte concentration, were systematically optimized to achieve the desired pH differential, guided by a comprehensive simulation model. The pH gradients generated by electrochemical reactions were mapped using confocal microscopy, revealing a high spatial resolution of ~10^0 μm and a rapid response time of ~10^1 s. Additionally, the biocompatibility of this electrochemical platform was evaluated, confirming its suitability for further applications in microbial systems.

During my graduate career, I have demonstrated that electrochemistry represents a highly promising approach for constructing controllable microenvironments within microbial systems, advancing the spatiotemporal resolution of the artificial gradients. This strategy can be extended to the regulation of various small molecules that play crucial roles in cellular physiology across diverse assemblages. The development of this platform provides a novel toolkit for investigating microbial behavior in heterogenous microenvironments, thereby contributing to the broader field of microbial physiology and ecology.

The dissertation of Jingyu Wang is approved.

Justin Ryan Caram

William M. Gelbart

Xiangfeng Duan

Chong Liu, Committee Chair

University of California, Los Angeles

2024

DEDICATION

I dedicate this thesis to my parents, Weihong Wang and Chunyan He, and my fiancé Sibo Wang.

Thank you for supporting me and being with me all the time. I love you all.

Table of Contents

Abstract of the Dissertation ii
Table of Contents vii
List of Figures ix
List of Tables xii
List of Supplemental Notes.....xiii
Acknowledgments xiv
Vita xvii

Chapter 1. General Introduction 1

Chapter 2. Electrochemical control for microscopic gradients of oxygen and hydrogen peroxide with machine learning–based inverse design
Abstract.....8
Introduction.....9
Results and Discussion.....13
Conclusion.....26
Materials and Methods.....27
References.....38
Supplementary Information.....46

Chapter 3. Electrochemical control for extracellular pH microenvironment with high spatiotemporal resolutions
Abstract.....66
Introduction.....67
Results and Discussion.....71

Conclusion.....85
Materials and Methods.....86
References.....96
Supplementary Information.....103
Supplementary References.....125

Chapter 4. Concluding Remarks.....127

List of Figures

Chapter 2. Electrochemical control for microscopic gradients of oxygen and hydrogen peroxide with machine learning–based inverse design

Figure 2.1. AI-based inverse design of electrochemically generated O_2 and H_2O_2 heterogeneities.....12
Figure 2.2. Spatiotemporal control of O_2 gradient on Pt-loaded microwire array.....16
Figure 2.3. Spatiotemporal control of H_2O_2 gradient on Au-loaded microwire array.....19
Figure 2.4. The development of inverse design for electrochemically generated O_2 and H_2O_2 gradients.....22
Figure 2.5. Experimental validations of MLPNN-assisted inverse design.....25
Figure S2.1. Scanning electron microscopy (SEM) images for the surface of wire array electrode without the deposition of Au/Pt catalysts.....48
Figure S2.2. Morphological characterization of Pt-coated wire array electrodes with k = (15, 4, 50) 49
Figure S2.3. Morphological characterization of Au-coated wire array electrodes with k = (15, 4, 50) 50
Figure S2.4. Linear scan voltammetry (LSV) measurement on Pt-coated wire array electrodes from 0.9 V *vs.* RHE to 0.4 V *vs.* RHE.....51
Figure S2.5. Linear scan voltammetry (LSV) measurement on Au-coated wire array electrodes from 0.9 V *vs.* RHE to 0.4 V *vs.* RHE.....52
Figure S2.6. Rotating ring-disk electrode (RRDE) voltammetry on Au-coated working electrodes.....53
Figure S2.7. Photo of a fluidic device for a confocal microscope.....54
Figure S2.8. Plot of measured normalized phosphorescence intensity I_{pn} under various O_2 concentration.....55
Figure S2.9. Plot of measured fluorescence intensity (I_f) under various H_2O_2 concentration on Au-coated wire array electrodes with morphology of k = (15, 4, 50) 56
Figure S2.10. Plot of measured I_f under various H_2O_2 concentration on Au-coated wire array electrodes with morphology of k = (30, 3, 50) 57

Figure S2.11. Plot of measured I_f under various H_2O_2 concentration on Au-coated wire array electrodes with morphology of k = (15, 4, 20) 58
Figure S2.12. Plot of measured I_f under various H_2O_2 concentration on Au-coated wire array electrodes with morphology of k = (17, 3, 30) 59
Figure S2.13. Simulated and experimental O_2 gradient and H_2O_2 gradient on Pt/Au-loaded wire array electrodes under E_{appl} = 0.5 V *vs.* RHE.....60
Figure S2.14. Cyclic voltammetry measurement in ZoBell's solution using Ag-pseudo reference electrode.....61
Figure S2.15. Fluorescence intensity I_f measurement under different morphologies.....62
Figure S2.16. I_f difference between the upstream and downstream of the wire array electrode.....63
Figure S2.17. Fluorescence mapping on Au-coated planar electrode.....64
Figure S2.18. Machine learning model selection for O_2 gradient prediction on Pt-loaded wire array electrodes.....65

Chapter 3. Electrochemical control for extracellular pH microenvironment with high spatiotemporal resolutions

Figure 3.1. The design of electrochemical PCET reaction for extracellular pH modulation.....70
Figure 3.2. Electrochemical characterizations of BQDS and DHBS.....74
Figure 3.3. Aerobic growth of *Pseudomonas aeruginosa* with the presence of BQDS and DHBS.....76
Figure 3.4. Steady-state pH gradient generated by DHBS-based electrochemistry in biological mediums.....79
Figure 3.5. Temporal responses of electrochemically controlled pH microenvironments.....83
Figure S3.1. Linear sweep voltammetry of BQDS and DHBS on rotating disk electrode.....110
Figure S3.2. The determination of minimum inhibition concentration of DHBS for *P. aeruginosa* PA14.....111
Figure S3.3. Half-maximal inhibitory concentration measurement of DHBS for PA14.....112
Figure S3.4. Photos of the flow device for the imaging of a confocal microscope.....113
Figure S3.5. pH calibration at different *z* planes in the microfluidic device measured under confocal microscope.....114
Figure S3.6. Cyclic voltammograms to assess the redox behavior of C-SNARF-4.....115

Figure S3.7. UV-Vis absorption spectra of C-SNARF-4 before and after electrochemical testing.....116
Figure S3.8. The repeatability of the spatial pH profiles generated under oscillating E_{appl} values.....117
Figure S3.9. The pH gradient in the *x*-*z* plane numerically calculated by the COMSOL model....118
Figure S3.10. ΔpH, the difference between pH_{red} and pH_{ox}, numerically calculated as a function of multiple parameters including E_{red}.....119
Figure S3.11. ΔpH, the difference between pH_{red} and pH_{ox}, numerically calculated as a function of multiple parameters with a smaller *d* value.....120
Figure S3.12. Calibration of the reference electrodes deployed in this study.....121
Figure S3.13. The effect of flow rate on temporal response of pH profiles.....122
Figure S3.14. Cyclic voltammetry (CV) of DHBS on gold interdigitated electrode (gap =10 μm) 123
Figure S3.15. Extracting exchange current density of Au electrode for numerical simulation.....124

List of Tables

Chapter 2. Electrochemical control for microscopic gradients of oxygen and hydrogen peroxide with machine learning–based inverse design

Table S2.1: Phosphate-buffered saline (PBS) 47

Chapter 3. Electrochemical control for extracellular pH microenvironment with high spatiotemporal resolutions

Table S3.1: Phosphate-buffered saline (PBS) solution.....105
Table S3.2: Phosphate-buffered growth medium.....106
Table S3.3: 3-(N-morpholino)propanesulfonic acid (MOPS)-buffered growth medium.....107
Table S3.4 Compare the spatial and temporal performances of pH gradients in this work and previous literatures.....108

List of Supplemental Notes

Chapter 2. Electrochemical control for microscopic gradients of oxygen and hydrogen peroxide with machine learning–based inverse design

Note S2.1: Fluorescence intensity correction in H_2O_2 concentration calibration experiment.....46

Chapter 3. Electrochemical control for extracellular pH microenvironment with high spatiotemporal resolutions

Note S3.1: Choice of electrode materials in the electrochemical microfluidic system.....103

Note S3.2: The selection of the focal plane for the pH quantification during the imaging of confocal microscopy.....104

Acknowledgements

I would like to acknowledge my advisor Prof. Chong Liu first for his invaluable mentorship throughout my graduate career. My journey with Prof. Liu began during a summer internship in his lab, where I was deeply impressed by the innovative work combining electrochemistry and microbiology. His decision to accept me as a graduate student marked the beginning of my exploration into the fascinating world of interdisciplinary research. Prof. Liu provided countless opportunities for me to acquire new skills across diverse fields, shaping my passion for interdisciplinary inquiry. Beyond research, his guidance extended to essential aspects of communication, collaboration, and time management, all of which have been critical to my development.

The completion of this dissertation would not have been possible without the support and help from the members of Prof. Liu's lab. Their kindness and encouragement made the challenging path of graduate school far less isolating. I am especially grateful to Dr. Shengtao Lu and Dr. Jiao Deng, who taught me crucial research skills and guided me during the early stages of my graduate work. I would also like to extend my heartfelt thanks to Dr. Danlei Xiang, an exceptional friend who stood by me through many difficult moments. Dr. Xun Guan is an enthusiastic friend, and I am grateful for all that I learned about microbiology through her. Dr. Yongchao Xie and Dr. Haiyuan Zou provided invaluable assistance during the later years of my graduate studies, and I am grateful for their support. Additionally, I would like to thank Dr. Roselyn Rodrigues, Dr. Ben Natinsky, Dr. Jesus Iñiguez, Dr. Brandon Jolly, and Dr. Hongyuan Sheng for the many moments we shared in the office and during group meetings, which made this journey memorable.

For my research collaborators, I would like to thank my lab mates, Dr. Yi Chen and Dr. Ben Hoar, for our collaborative work published on *PNAS*. I am also thankful to Prof. Sam Emaminejad, Dr. Xuanbing Cheng, Jialun Zhu, Zongqi Li at the Department of Electrical and Computer Engineering for our work on enzymatic sensors. Additionally, I deeply appreciate the collaboration with Prof. Dianne Newman, Dr. Haiyuan Zou, and Dr. Yifan Gao about the NO gradients, which enriched my research and broadened my perspective.

I am especially grateful to my committee members: Prof. Justin Caram, Prof. William Gelbart, and Prof. Xianfeng Duan for their guidance and support throughout my PhD journey. Their insights and feedback were instrumental in the completion of my dissertation, pushing me to think critically and creatively.

I am also grateful to the professional staff across various facilities who helped me a lot in my research journey. My sincere thanks go to Dr. Ignacio Martini and Dr. Yu Chen at MIC, Dr. Haley Marks at CNSI, Brian Matthews and Hoc Ngo at Nanolab. Their expertise and assistance were were essential to the completion of my experiments. In addition, I want to extend my deep thanks to Dr. Johnny Pang. I enjoyed the time working as his TA and am grateful for his responsibility and care. My appreciation also extends to the many individuals whose names I am unable to list comprehensively but whose kindness and support did not go unnoticed. The small acts of help and encouragement from they made a significant difference, and I am deeply thankful for every moment of assistance.

I owe an immense debt of gratitude to my parents, Weihong Wang and Chunyan He. Their unwavering support and belief in me have been my anchor through challenging times. I am endlessly thankful for their love. To my fiancé, Sibo Wang, thank you for sharing this journey with

me. We have shared countless moments together, and your presence has been a pillar of strength in both my personal and academic life.

Thank you to everyone who has been a part of this journey. Completing my dissertation and achieving a Ph.D. in Chemistry would not have been possible without your contributions and support. I am deeply grateful to all of you.

VITA

EDUCATION

University of California, Los Angeles (UCLA) Los Angeles, CA, US
Doctor of Philosophy Track, Chemistry, GPA: 3.92/4.00 Sep. 2019 - Sep 2024
University of Science and Technology of China (USTC) Hefei, Anhui, China
Bachelor of Science, Chemical Physics, Special Class of the Gifted Young Sep. 2015 - June 2019

RESEARCH EXPERIENCE

Graduate research at UCLA Department of Chemistry and Biochemistry Advisor: Prof. Chong Liu

Electrochemical pH gradient for microbial system Nov. 2021 - Present

- Developed an electrochemical-biological hybrid systems for controllable pH microenvironment. Designed proton-coupled-electron-transfer reactions for local pH change and characterized their electrochemical properties. Built a finite-element-analysis model to simulated electrochemical systems in the flow device and optimized the pH difference of the gradient. Conducted operando measurement of spatial pH distribution in electrochemical system.

Machine Learning Assisted Kinetic Analysis for CO_2 Reduction Aug. 2021 - July 2023

- Demonstrated a machine-learning assisted method to extract of kinetic information from discrete data points. Fabricated and characterized Au catalysts on planar electrodes and Si micro wire array electrodes. Measured the electrochemical performance and analyze the electrochemical kinetic.

Inverse Design of Electrochemical O_2 and H_2O_2 gradient Oct. 2020 - Apr. 2022

- Developed a machine-learning based inverse design strategy to predict the electrode morphology for a desired O_2 or H_2O_2 gradient and demonstrated better spatiotemporal control for extracellular space.

Electrochemical CO Generation in Microbial System Jan. 2021 - Sep. 2021

- Developed a biocompatible electrochemical platform for on-demand CO generation by CO_2 reduction catalyzed by metal phthalocyanines on nanotubes.

Electrocatalytic Methane Oxidation to Methanol Under Mild Conditions Sep. 2019 - Nov. 2020

- Investigated electrochemical methane oxidation to methanol by hydroxyl radicals generated from oxygen reduction catalyzed by Au-Pd nanoparticles on Si nanowires at ambient temperature.

Undergraduate research at USTC, Department of Chemistry Advisor: Prof. Changzheng Wu

Platinum nanofoams for Robust Fuel-Cell Oxygen Reduction Electrocatalysts Sep. 2016 - Mar. 2017

- Synthesized grain-boundary-rich Pt nanofoams at high temperature annealing condition and achieved a robust electrocatalysis performance for acid oxygen reduction reaction (ORR).

Nanowire Catalysts for Efficient Alkaline Hydrogen Evolution Reaction April. 2017 - Nov. 2018

- Synthesized CoP nanowires on carbon clothes and demonstrated an enhanced activity for alkaline hydrogen evolution reaction (HER).

PUBLICATIONS

- **Wang, J.,** Xie, Y., Zou, H., Chen, Y., Liu, C.* *Electrochemical control with high spatiotemporal resolutions for extracellular pH microenvironment*, submitted.
- Cheng, X.†, Li, Z.†, Zhu, J†, **Wang**, J., Huang, R., Lin, S., Forman, S., Gromilina, E., Puri, S., Patel P., Bahramian, M., Tan, J., Hojaiji, H., Jelinek, D., Voisin, L., Zhang, A., Lei, L, Coller, H., Reyes, B., Matsumoto, J., Lu, D., Liu, C., Milla, C., Emaminejad, S.* *Unlocking oxidoreductase library for in-vivo biomonitoring*, submitted.
- Xie, Y., Erşan, S., Guan, X., **Wang, J.**, Sha, J., Xu, S., Wohlschlegel, J. A., Park, J. O., Liu, C.* *Unexpected metabolic reallocation of CO_2 fixation in H_2-mediated materials-biology hybrids*, ***Proc. Natl. Acad. Sci. U.S.A.*** **2023**, *120*(42), e2308373120.

- Chen, Y.†, **Wang, J.†,** Hoar, B. B.†, Lu, S., Liu, C.* *Machine-learning-based inverse design for electrochemically controlled microscopic gradients of O_2 and H_2O_2*, ***Proc. Natl. Acad. Sci. U.S.A.* 2022,** *119,* e2206321119
- Cheng, H., Liu, S., Hao, Z., **Wang, J.,** Liu, B., Liu, G., Wu X., Chu W., Wu C.*, Xie Y. *Optimal coordination-site exposure engineering in porous platinum for outstanding oxygen reduction performance.* ***Chem. Sci.* 2019**, *10*(21), 5589-5595
- Xu, K., Cheng, H., Lv, H., **Wang, J.,** Liu, L., Liu, S., Wu X., Chu W., Wu C.*, Xie Y. *Controllable Surface Reorganization Engineering on Cobalt Phosphide Nanowire Arrays for Efficient Alkaline Hydrogen Evolution Reaction.* ***Adv. Mater.* 2018**, *30*, 1703322

CONFERENCE & PRESENTATIONS

- Southern California Inorganic Photochemistry Conference (SCIP), **Oral** — Santa Catalina Island, CA
  Electrochemical Platform of Controllable pH Gradients in Microbial Systems — 04/2024
- Southern California Electrochemistry Conference for Students (SCECS), **Oral** — Irvine, CA
  Electrochemical Platform of Controllable pH Gradients in Microbial Systems — 04/2024
- International Society for Microbial Electrochemical Technologies Conference, **Poster** — Houston, TX
  Electrochemical Platform of Controllable pH Gradients in Microbial Systems — 04/2024
- Amgen Women in Chemistry Graduate Student Research Symposium, **Poster** — Thousand Oaks, CA
  Electrochemical Platform of Controllable pH Gradients in Microbial Systems — 03/2024
- Electrochemistry Gordon Research Seminar (GRS), **Poster** — Ventura, CA
  Electrochemical Platform of Controllable pH Gradients in Microbial Systems — 01/2024
- Electrochemistry Gordon Research Conference (GRC), **Poster** — Ventura, CA
  Electrochemical Platform of Controllable pH Gradients in Microbial Systems — 01/2024

TEACHING EXPERIENCE

UCLA Department of Chemistry and Biochemistry

- **Advanced Inorganic Chemistry** (instructor: Prof. Chong Liu, student rating: 8.08/9.00)
- **General Chemistry Lab** (instructor: Dr. Johnny W. Pang, averaged student rating: 8.24/9.00)

USTC Department of Chemistry

- **Physical Chemistry Experiments** (instructor: Prof. Guangming Liu)

SERVICE

Reviewer of *ACS Applied Materials & Interfaces* and *RSC Sustainability* — 2024

Judge for International Science and Engineering Fair — 2024

Volunteer at Chinese Academy of Sciences Public Science Day, USTC — 2016, 2017

HONORS & AWARDS

- Evelyn Pan Dissertation Award — 2024
- UCLA Doctoral Student Travel Grants $1,000 — 2024
- Dafni Amirsakis Memorial Award — 2023
- UCLA Dissertation Year Fellowship, $20,000 plus standard tuition and fees — 2023
- USTC Outstanding Graduates Awards — 2019
- Scholarship for Annual Excellent Undergraduates — 2016, 2017, 2018
- Silver Medal winner in 2017 International Genetically Engineered Machine Competition — 2017
- Scholarship for Excellent Freshmen, tuition and fees for four years — 2015

Chapter 1. General Introduction

Motivation: Complexity of heterogeneous microenvironments in microbial systems

Heterogeneous microenvironments in microbial systems play a critical role in shaping the physiological behavior of cells within complex assemblages.[1,2] Multicellularity, a feature observed across phylogenetic lines, enables cells to adhere to and communicate with one another,[3] leading to the formation of structural constraints that generate physical and chemical gradients. These gradients arise from both endogenous metabolic activities and external limitations on solute diffusion, influencing the development and function of multicellular structures.[4] In microbial biofilms, such gradients of oxygen,[5] nutrients,[6] waste products,[7] and signaling molecules[8] create distinct microenvironments, fostering a diverse range of physiological states within closely packed bacterial communities. This micro-scale heterogeneity means that bacterial cells in biofilms can exhibit significant physiological divergence due to the localized chemical landscape. Even the neighboring cells could express the cell-to-cell variation in response to the local environment,[9] further contributing to the complex heterogeneity observed within biofilms. Such variability can arise from differences in gene expression, protein production, and metabolic activity, all of which are modulated by the localized microenvironment.[2] Understanding these processes requires a detailed mapping of extracellular gradients and a thorough investigation of the intricate relationship of the bacteria physiological activity and local microenvironment within these structured communities.

While it is increasingly recognized that individual cells within a population can exhibit remarkable heterogeneity in their behavior and responses to local environments, revealing the in-depth relationship between microbial physiology and microenvironmental conditions demands more than merely observing bacterial responses in natural systems. Firstly, the natural microenvironment is influenced by bacterial metabolism,[1] which is inherently uncontrollable. To conduct more complex

studies, particularly under specific or extreme conditions, a controllable gradient is necessary. Secondly, natural microbial systems often contain multiple chemical gradients, which may change in a coupled manner.[10,11] This complexity makes it challenging to investigate the effects of a specific gradient independently. Therefore, it is crucial to create artificial gradients that are well-controlled and independent of other gradients. By designing controllable gradients, researchers can gain deeper insights into the intricate relationship between microbial cells and their microenvironments, enabling more precise studies of these complex systems.

Precedence: Electrochemistry in artificial concentration gradient generators

The generation of chemical concentration gradients is a necessary technique to study cellular responses to the local microenvironments. Historically, various methods such as chamber systems, pipette injectors, hydrogel, membrane channel, and microfluidic multi-injectors have been employed to create gradients for in vitro studies.[12] These traditional techniques have significantly advancing our understanding of cellular behavior and have inspired the development of more sophisticated gradient generator systems. Among these techniques, microfluidic technology by means of laminar-flow mixing has gained popularity due to its high spatial control, approximately 10^2 μm, and its efficiency in minimizing reagent consumption.[13] However, the growing interest in single-cell physiology and metabolism has revealed limitations in these conventional methods, especially regarding their spatial and temporal resolution.

One major constraint is the spatial resolution. Considering the size of bacterial cells, which usually ranges from 1 to 10 μm,[14] a finer spatial resolution at the micrometer scale is necessary to accurately study cellular responses at the single-cell level. Additionally, temporal control of the gradient is increasingly important. The dynamic nature of microbial systems and their responses to sudden perturbations are crucial for understanding the adaptability, resilience, and antimicrobial resistance

of microbial communities under fluctuating environmental conditions.[15,16] Thus, there is a pressing need for gradient generators that can rapidly alter the gradient profile, providing real-time control over the extracellular environment.

Electrochemistry is a promising technique to address these challenges, given its fast and controllable kinetics. Microfabrication techniques allow for the design and fabrication of electrodes at the microscopic level,[17] facilitating the generation of chemical gradients with spatial resolutions on the order of micrometers. Furthermore, the customization of electrode morphology provides more flexibility in the shape of artificial gradients, tailored to the specific needs of the microbial systems. When coupled with advanced imaging techniques, such as confocal microscopy, electrochemically generated gradients can be mapped with spatial resolutions of less than 1 μm,[18] offering unparalleled precision for single-cell studies. The fast-switching nature of electrochemical systems also permits the rapid perturbation of extracellular microenvironments (~10 sec),[19] faster than the timescales of cellular translation and transcription responses.[20] These characteristics make electrochemical gradient generators particularly well-suited for high-precision biochemical studies, enabling real-time analysis at the single-cell level.

This work: Novel electrochemical platforms for concentration gradients with high spatiotemporal resolutions

Electrochemical techniques offer significant advantages for creating concentration gradients of biologically relevant molecules with high spatiotemporal resolution. My thesis explores this potential through the development of electrochemical platforms of O_2, H_2O_2, and protons. The design involved careful selection of electrochemical reactions and customization of electrode morphology to achieve desired gradient profiles. The gradients were visualized and quantified using microscopy, demonstrating their spatial precision, while the system's temporal response was also thoroughly

evaluated. To enhance understanding, complementary techniques such as COMSOL simulations and machine learning models were applied.

In **Chapter 2**, I present the electrochemical control of O_2 and H_2O_2 gradients, where selectivity was achieved through catalyst choice. A comprehensive dataset of O_2 and H_2O_2 gradients on microwire electrodes was established with the assistance of COMSOL simulations and a multilayer neural network model. This enabled an inverse design approach to program specific gradient profiles, facilitating the creation of well-programmed gradients at microscopic level for complex microbial systems. **Chapter 3** extends this work to electrochemically generated pH microenvironments. The use of interdigitated electrodes provided higher flexibility in controlling gradient shapes, and the system's rapid temporal response makes it suitable for studying bacterial responses to swift perturbations. Biocompatibility evaluations confirm the system's suitability for further exploration in microbial systems.

References

1 Jo, J., Price-Whelan, A. & Dietrich, L. E. Gradients and consequences of heterogeneity in biofilms. *Nat. Rev. Microbiol.* **20**, 593-607 (2022).

2 Stewart, P. S. & Franklin, M. J. Physiological heterogeneity in biofilms. *Nat. Rev. Microbiol.* **6**, 199-210 (2008).

3 Lyons, N. A. & Kolter, R. On the evolution of bacterial multicellularity. *Curr. Opin. Microbiol.* **24**, 21-28 (2015).

4 Ellison, D. *et al.* Cell–cell communication enhances the capacity of cell ensembles to sense shallow gradients during morphogenesis. *Proc. Natl. Acad. Sci. U. S. A.* **113**, E679-E688 (2016).

5 De Beer, D., Stoodley, P., Roe, F. & Lewandowski, Z. Effects of biofilm structures on oxygen distribution and mass transport. *Biotechnol. Bioeng.* **43**, 1131-1138 (1994).

6 Williamson, W. M., Close, M. E., Leonard, M. M., Webber, J. B. & Lin, S. Groundwater biofilm dynamics grown in situ along a nutrient gradient. *Groundwater* **50**, 690-703 (2012).

7 Damgaard, L. R., Nielsen, L. P. & Revsbech, N. P. Methane microprofiles in a sewage biofilm determined with a microscale biosensor. *Water Res.* **35**, 1379-1386 (2001).

8 Bellin, D. L. *et al.* Electrochemical camera chip for simultaneous imaging of multiple metabolites in biofilms. *Nat. Commun.* **7**, 10535 (2016).

9 Martins, B. M. & Locke, J. C. Microbial individuality: how single-cell heterogeneity enables population level strategies. *Curr. Opin. Microbiol.* **24**, 104-112 (2015).

10 Okabe, S., Itoh, T., Satoh, H. & Watanabe, Y. Analyses of spatial distributions of sulfate-reducing bacteria and their activity in aerobic wastewater biofilms. *Appl. Environ. Microbiol.* **65**, 5107-5116 (1999).

11 Jo, J., Price-Whelan, A., Cornell, W. C. & Dietrich, L. E. Interdependency of respiratory metabolism and phenazine-associated physiology in *Pseudomonas aeruginosa* PA14. *J. Bacteriol.* **202**, 10.1128/jb. 00700-00719 (2020).

12 Somaweera, H., Ibraguimov, A. & Pappas, D. A review of chemical gradient systems for cell analysis. *Anal. Chim. Acta* **907**, 7-17 (2016).

13 Wang, X., Liu, Z. & Pang, Y. Concentration gradient generation methods based on microfluidic systems. *RSC Adv.* **7**, 29966-29984 (2017).

14 Levin, P. A. & Angert, E. R. Small but mighty: cell size and bacteria. *Cold Spring Harb. Perspect. Biol.* **7**, a019216 (2015).

15 Parrilli, E., Tutino, M. L. & Marino, G. Biofilm as an adaptation strategy to extreme conditions. *Rend. Lincei. Sci. Fis. Nat.* **33**, 527-536 (2022).

16 Gebreyohannes, G., Nyerere, A., Bii, C. & Sbhatu, D. B. Challenges of intervention, treatment, and antibiotic resistance of biofilm-forming microorganisms. *Heliyon* **5** (2019).

17 Huang, X. J., O'Mahony, A. M. & Compton, R. G. Microelectrode arrays for electrochemistry: approaches to fabrication. *Small* **5**, 776-788 (2009).

18 Jung, H. S. *et al.* CMOS electrochemical pH localizer-imager. *Sci. Adv.* **8**, eabm6815 (2022).

19 Chen, Y., Wang, J., Hoar, B. B., Lu, S. & Liu, C. Machine learning–based inverse design for electrochemically controlled microscopic gradients of O_2 and H_2O_2. *Proc. Natl. Acad. Sci. U. S. A.* **119**, e2206321119 (2022).

20 Fröhlich, F. *et al.* Multi-experiment nonlinear mixed effect modeling of single-cell translation kinetics after transfection. *NPJ Syst. Biol. Appl.* **4**, 42 (2018).

Chapter 2. Electrochemical control for microscopic gradients of oxygen and hydrogen peroxide with machine learning–based inverse design

This chapter is a version of Chen, Y.†; Wang, J.†; Hoar, B. B. †; Lu, S.; Liu, C. "Mach-learning-based inverses design of electrochemically controlled microscopic gradients of O_2 and H_2O_2." *Proc. Natl. Acad. Sci. U.S.A.* **2022**, 119(32), e2206321119 (†, equal contribution)

Abstract

A fundamental understanding for the extracellular microenvironments of O_2 and reactive oxygen species (ROS) such as H_2O_2, ubiquitous in microbiology, demands high-throughput methods of mimicking, controlling, and perturbing gradients of O_2 and H_2O_2 at microscopic scale with high spatiotemporal precision. However, paucity exists for a high-throughput strategy of microenvironment design, and it remains challenging to achieve O_2 and H_2O_2 heterogeneities with the microbiologically desirable spatiotemporal resolutions. Here we report machine-learning-based inverse design of electrochemically generated microscopic O_2 and H_2O_2 profiles that are relevant for microbiology. Microwire arrays with suitably designed electrochemical catalysts enables the independent control of O_2 and H_2O_2 profiles with spatial resolution of $\sim 10^1$ μm and temporal resolution of $\sim 10^0$ sec. Neural networks aided by data augmentation inversely design the experimental conditions needed for targeted O_2 and H_2O_2 microenvironments while being order-of-magnitude faster. Integrating artificial intelligence with electrochemically controlled concentration heterogeneity creates a viable fast-response platform towards better understanding the extracellular space with desirable spatiotemporal control.

Introduction

Ubiquitous spatiotemporal heterogeneity of natural environments fosters the diverse and fascinating biology that our world embraces and motivates researchers to mimic natural environments with high spatiotemporal resolution.[1-5] Given their close relevance in biochemical metabolisms, dioxygen (O_2) and hydrogen peroxide (H_2O_2) as a surrogate of reactive oxygen species (ROS) are two ubiquitous biologically relevant species in extracellular medium.[1, 6] Their extracellular spatial and temporal distributions, particularly at microscopic scale ranging from 1 μm to 100 μm,[7-11] are critical for signal transduction, protein expression, biochemical redox balance, and regulation for cellular metabolism with extensive ecological, environmental, and biomedical implications (Fig. 2.1A).[1, 3, 8-13] A programmable creation of the spatiotemporal concentration profiles of O_2 and H_2O_2 offers the freedom to mimic, control and perturb the microenvironments of O_2 and H_2O_2 and hence advance our understanding in microbiology.

Despite the recent progresses,[14-18] there remain major technical challenges, particularly in the achievable spatiotemporal resolution and high-throughput design of concentration profiles to suit a plethora of scenarios in microbiology. Approaches based on microfluidics and hydrogels have been able to achieve concentration gradients of O_2 and H_2O_2 through the provision of either O_2/H_2O_2 source,[14, 19-21] O_2/H_2O_2 scavenging agents,[15, 22, 23] or a combination of both[24] across liquid-impermeable barriers such as agar layers or polymeric thin films.[25, 26] Yet such approaches dependent on passive mass transport and diffusion across more than 10^2 μm are inherently incapable of achieving spatial features of less than 100 μm and temporal resolution smaller than ~10^1 seconds, the prerequisites to investigate microbiology at cluster or single-cell levels.[10-12] Moreover, the large variations of extracellular O_2 and H_2O_2 gradients in different microbial systems demand an inverse-design strategy, which with minimal expenditure quickly programs a desired

concentration profile catering to a specific biological scenario.[2-5] The current lack of inverse-design protocol impedes the adoption of controllable extracellular heterogeneity to mimic and investigate microbial systems that are of environmental, biomedical, and sustainability-related significances.

We envision that the integration of electrochemically generated concentration gradients with inverse design based on machine learning (ML) will address the aforementioned challenges (Fig. 2.1B). Electrochemistry offers a venue of transducing electric signals into microscopic concentration profiles within $10^0 \sim 10^2$ μm away from electrodes' surface, following the specific electrode reaction kinetics and the mass-transport governing equations in the liquid phase.[27] Proper designs of electrodes' microscopic spatial arrangement and electrochemical kinetics lead to concentration gradients that are spatiotemporally programmable by time-dependent electric signals of varying voltages.[28] Such benefits of electrochemically generated concentration gradients lead us to employ electrochemistry as a tool to spatiotemporally control the concentration profiles in the extracellular medium. In one example, we found that wire arrays electrochemically active towards O_2 reduction create anoxic microenvironment about 20 μm away from the aerobic external bulk environments, modulate the size and extent of O_2 depletion in the anoxic microenvironment by wire array's morphology and applied electrochemical potential (Eappl), and hence enable O_2-sensitive rhizobial N_2 fixation in ambient air powered by renewable electricity.[29] Moreover, while not reported before as far as we know, electrochemically generated concentration heterogeneity is commensurate with ML-based inverse design,[30, 31] thanks to the mathematically well-defined electrochemical processes that can be numerically simulated.[32, 33] We recently reported neural networks, trained by numerically simulated data, that explore the influence of electrode geometry on electrochemical N_2 fixation and achieve optimized morphologies of wire array electrodes

untenable without such ML-based strategy.[34] An inverse design for the electrochemically generated gradients will quickly program desirable microenvironments of O_2 and ROS with high spatiotemporal resolutions, thanks to the well reported electrochemical transformation related to O_2 and H_2O_2 with high electrochemical selectivity.[35, 36]

In this work, we report an inverse design based on neural networks for independent electrochemical creation of O_2 and ROS microscopic gradients that are relevant and mimic their extracellular heterogeneities in microbial systems. We hypothesize that careful design of electrocatalysis of O_2 reduction reaction (ORR) can either facilitate four-electron ORR on Pt electrocatalyst for a controllable O_2 spatiotemporal profile, or promote two-electron ORR on Au electrocatalyst for a programmable generation of H_2O_2 gradient without significantly perturbing the O2 one, thanks to their concentration differences in biological mediums (10^{-1}~10^{1} μM for H_2O_2 and 10^{1}~10^{2} μM for O_2).[2, 7-11] Electrochemically active microwire array electrodes as exemplary model systems (Fig. 2.1C) are experimentally shown to achieve tunable heterogeneities of O_2 and H_2O_2 independently, with spatial resolution of ~10^{1} μm and temporal resolution of ~10^{0} sec, and are suitable as a platform of independently perturbing biologically relevant O_2 and H_2O_2 profiles in microbial systems. We further established and experimentally validated two neural networks that inversely design the wire array electrodes' morphologies towards targeted microenvironments of O_2 and H_2O_2, respectively, which is at least one order of magnitude faster than trial-and-error numerical simulation and two orders of magnitudes faster than experimental explorations. The demonstrated inverse design of electrochemically generated controlled gradients not only demonstrates a full electrochemical control of concentration profiles in an electrode's proximity but also establishes an approach of spatiotemporally mimicking and perturbing extracellular space guided by artificial intelligence.

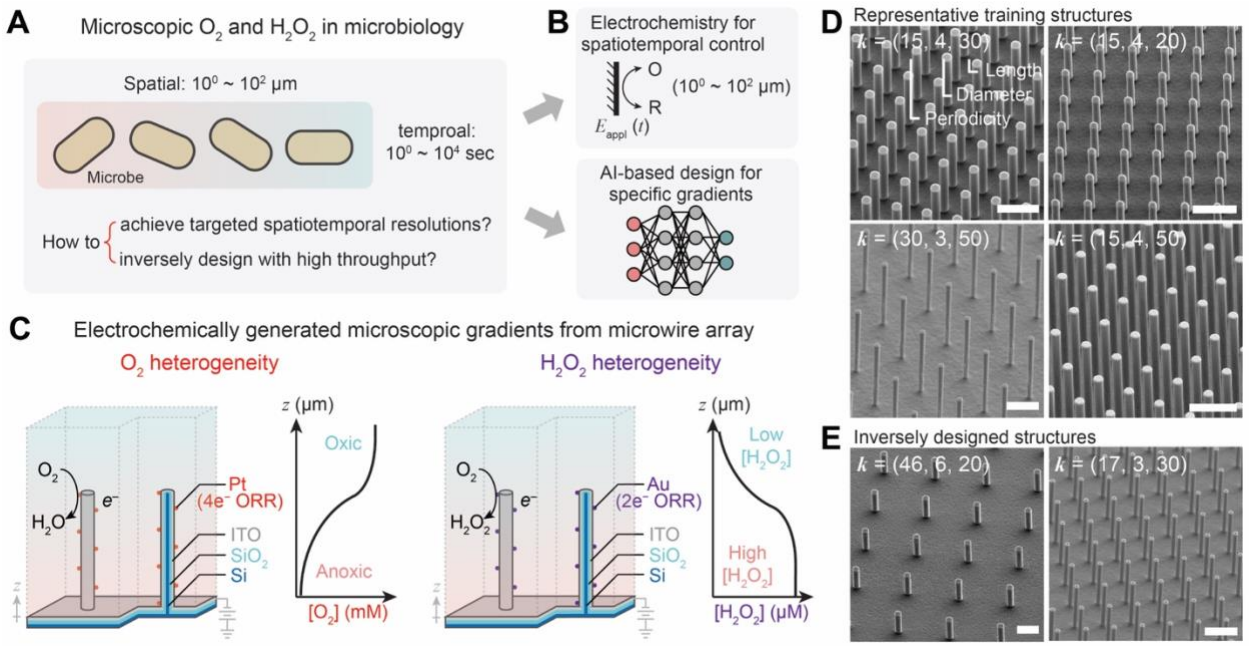


Figure 2.1. AI-based inverse design of electrochemically generated O_2 and H_2O_2 heterogeneities. A, The ubiquitous spatiotemporal heterogeneities of O_2 and H_2O_2 in microbiology and the challenges posed in this research topic. **B**, The combination of electrochemistry and machine-learning-based inverse design offers a viable approach of mimicking and control the heterogeneities of O_2 and H_2O_2 in microbiology. O, oxidant; R, reductant; E_{appl} (t), the time-dependent electrochemical voltages applied on electrodes. **C**, The design of the electrochemically active microwire array electrodes for the generation of O_2 and H_2O_2 gradients. $4e^-$ ORR & $2e^-$ ORR, four-electron and two-electron oxygen reduction reaction into H_2O and H_2O_2, respectively; ITO, indium tin oxide. **D** and **E**, 45-degree tilting images of scanning electron microscopy for the representative microwire arrays used for the training of machine-learning model (**D**) and the ones inversely designed for targeted O_2 and H_2O_2 gradients (**E**). $\boldsymbol{k} = (P, D, L)$, the morphological vector that includes the periodicity (P), diameter (D) and length (L) of the synthesized wire arrays in the unit of μm. Scale bars are 20 μm.

Results and Discussion

Wire array electrodes for electrochemically generation of O_2 and H_2O_2 gradients

We applied microwire electrode array loaded with selective ORR electrocatalysts to establish customizable O_2 or H_2O_2 gradients (Fig. 2.1C). Si-based microwire arrays in a square lattice were constructed through photolithography and reactive ion-etching in a five-step fabrication process (see "Materials and Methods" section). After thermal annealing to generate an electrically insulating oxide layer, indium-doped tin oxide (ITO) of 500 nm was deposited via sputtering near conformally onto the wire array, followed by the deposition of about 7-nm Pt and Au for the generation of O_2 and H_2O_2 gradients via selective ORR, respectively. Here the deposition of electrically conducted ITO layer ensures a uniform distribution of applied electrochemical potential (E_{appl}). We employed Pt as the selectively electrocatalysts of four-electron ORR[35, 37, 38] in the generation of O_2 gradients, while Au for two-electron ORR[35, 39, 40] in the generation of H_2O_2 gradients. The morphologies (Fig. 2.1D, 2.1E, and S2.1) and compositions (Fig. S2.2 and Fig. S2.3) of the established wire array were characterized and confirmed by scanning electron microscopy (SEM) equipped with energy dispersive X-ray spectroscopy (EDS), with a vector k = (P, D, L) presenting the wire arrays' periodicity (P), diameter (D), and length (L), respectively, in the unit of μm.

The prepared wire array electrodes coated with Pt and Au exhibit desirable electrochemical properties for creating O_2 and H_2O_2 heterogeneities, respectively. In phosphate buffer saline (PBS) solution, linear scan voltammograms (20 mV/s) of the deposited Pt electrocatalysts on the wire array (Fig. S2.4) exhibited an onset potential of ORR at around 0.8 V vs. reversible hydrogen electrode (RHE). Linear scan voltammograms of the deposited Au electrocatalysts showed a similar onset potential of ORR at around 0.6 V *vs.* RHE (Fig. S2.5). Experiments of rotating ring-

disk electrode for the Au electrocatalysts (Fig. S2.6) displayed a selectivity of H_2O_2 generation from O_2 reduction up to 50% at 0.5 V vs. RHE. Thanks to the reaction-diffusion model in the electrolyte and the electrochemical boundary conditions imposed by the microwire morphology,[29, 41, 42] the Pt and Au-loaded wire array electrode transduces electric voltages E_{appl} into concentration gradients of O_2 and H_2O_2, respectively, at microscopic length scales.

Electrochemical generation and control of O_2 concentration profiles

The Pt-deposited microwire array electrode is capable of spatiotemporally controlling the electrochemically generated O_2 gradient. Thanks to its triplet-triplet quenching with $^3O2$,[43] the phosphorescence emission of tris(1,10-phenanthroline)ruthenium(II), $Ru(phen)_3^{2+}$, from the inter-system crossing after optical excitation between 350~500 nm,[44] was utilized to spatiotemporally probe the local concentration of O_2 ($[O_2]$) (Fig. 2.2A). The constructed microwire array electrode was housed in a home-made fluidic device (Fig. S2.7) under a confocal microscope with a 470-nm optical excitation (see "Materials and Methods" section). Under a constant flow of aerated PBS solution with 0.15 mM $Ru(phen)_3^{2+}$ ($[O_2]$ = 0.246 mM saturated with ambient air[45]), the phosphorescence emission intensity (I_p, 610~650 nm), inversely proportional to the value of $[O_2]$, was collected and a calibration curve was established for the quantification of local $[O_2]$ values (see "Materials and Methods" section, Fig. S2.8). When $\boldsymbol{k}$ = (15, 4, 50) for the wire array (Fig. 2.2B and 2.2C), the three-dimensional I_p mapping were recorded in a time sequence when the Pt-coated wire array was initially under an open-circuit condition (t < 15 sec), subject to an electrochemical potential (E_{appl} = 0.5 V *vs.* RHE) from t = 15 and 45 sec, and reverted back to the open-circuit condition when t > 45 sec (see "Materials and Methods" section). The side-views of the three- dimensional I_p mapping were displayed when E_{appl} was initially absent (t = 0 sec), E_{appl} = 0.5 V *vs.* RHE (t = 16 sec), and E_{appl} was absent again at t = 48 sec ("t = 0", "t = 16 sec", and "t

= 48 sec" in Fig. 2.2B, respectively). The intensity of I_p was noticeably stronger within the wire array when E_{appl} = 0.5 V *vs.* RHE in comparison to the Ip values under the open-circuit conditions before and after the presence of E_{appl}. As I_p is inversely proportional to the local values of [O_2], this observation qualitatively suggested a decrease of [O_2] hence a O_2 gradient covering the wire array region with microscopic resolution under a reductive electrochemical potential.

The averaged [O_2] values ($[O_2]_{avg}$) at different distances above the bottom of the wire array z = 5, 50, 100 μm were quantified and displayed as a function of time t in Fig. 2.2C. While negligible change of $[O_2]_{avg}$ was recorded at z = 100 μm (black in Fig. 2.2C), which was quite far away from the wire array, at z = 5 and 50 μm (blue and red in Fig. 2.2C, respectively) significant changes of $[O_2]_{avg}$ up to complete anoxic condition were observed, concurrent with the temporal presence of E_{appl}. Such data suggest that the established O_2 gradient can be temporally switched by electrochemical potentials faster than the temporal resolution of the confocal microscopy under the tested conditions (~2.7 sec). The electrochemically established O_2 gradient for wire array $\boldsymbol{k}$ = (30, 3, 50) were similarly quantified at E_{appl} = 0.4, 0.5, and 0.6 V *vs.* RHE as a function of the distance above the bottom of wire array (z) (black, red, and blue in Fig. 2.2D, respectively). The steepness of the generated O_2 gradient increased at lower Eappl values under which the electrochemical activities of O_2 consumption on Pt was more pronounced thanks to the increased magnitude of reductive overpotential (Fig. S2.4). Such an E_{appl} -dependent O_2 gradient showed that electrochemical input was capable of spatially controlling and yielding a desirable O_2 gradient for potential biological applications given biologically relevant [O_2] values and the spatial resolutions detected here.[2-4, 46, 47] The electrochemically driven O_2 gradients were also quantified at E_{appl} = 0.5 V *vs.* RHE for $\boldsymbol{k}$ = (15, 4, 50), (30, 3, 50), and (30, 3, 30) (black, red, and blue in Fig. 2.2E, respectively). Noticeably different O_2 gradients were observed, suggesting the capability of

wire array morphology to yield a specific O_2 gradient. Particularly, a strictly O_2-free local environment in aerated medium was established for $\boldsymbol{k}$ = (15, 4, 50). Such a customizable O_2 gradient will be of interests for the study of communal interactions for the study of communal interactions among microorganisms of varying degrees of O_2 demands that are prevalent in nature.[2]

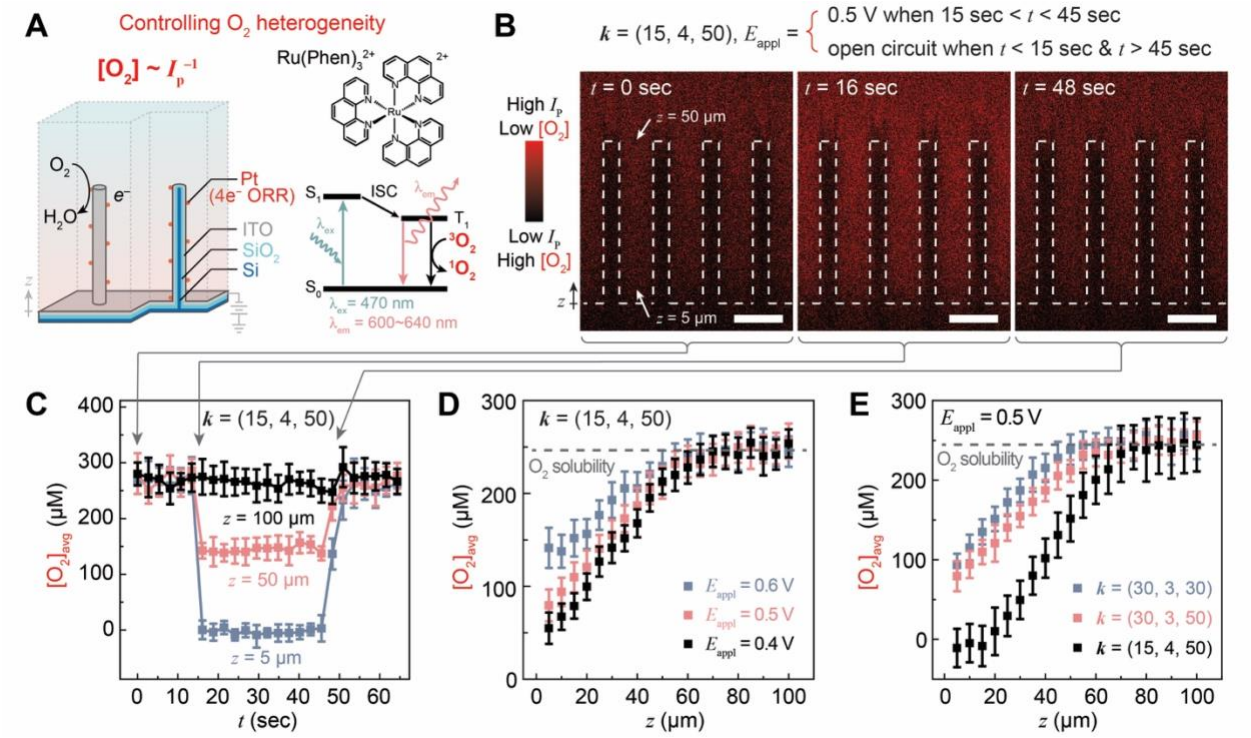


Figure 2.2. Spatiotemporal control of O_2 gradient on Pt-loaded microwire array. A, Design of Pt-loaded microwire array and the fundamentals of spatiotemporal mapping local O_2 concentrations ($[O_2]$) based on the intensity of phosphorescence emission (I_p) from tris(1,10-phenanthroline)ruthenium(II) ($Ru(phen)_3^{2+}$). $^3O_2$ and $^1O_2$, the triplet and singlet dioxygen molecule, respectively; S_0 and S_1, the ground state and the first excited singlet state, respectively; T_1, the first excited triplet state; ISC, intersystem crossing; λ_{ex} and λ_{em}, the wavelengths of optical excitation and emission, respectively. **B** and **C**, Cross-sectional I_p profiles on wire array $\boldsymbol{k}$ = (15, 4, 50) at t = 0, 16, and 48 secs (**B**) and the subsequent temporal evolution of averaged local O_2

concentrations ($[O_2]_{avg}$) at different distances z from the base of wire array (**C**). The values of E_{appl} is against reversible hydrogen electrode (RHE). The microwires are depicted in dashed lines in **B**. Scale bars are 15 μm. **D**, Plots of $[O_2]_{avg}$ versus z under different values of E_{appl} for wire array $\boldsymbol{k}$ = (15, 4, 50). **E**, Plots of $[O_2]_{avg}$ versus z in wire arrays of different $\boldsymbol{k}$ when E_{appl} = 0.5 V. Error bars represent standard deviations across multiple separate measurements in the device ($n \geq 3$).

Electrochemical generation and control of H_2O_2 concentration profiles

We can similarly establish the gradients of H_2O_2, a potent reactive oxygen species (ROS) relevant to biology,[48] with the use of electrochemically active wire array electrodes and H_2O_2-yielding Au ORR electrocatalysts. The local concentration of generated H_2O_2 ($[H_2O_2]$) was quantified based on the fluorogenic rection that converts non-fluorescent 10-acetyl-3,7-dihydroxyphenoxazine (Amplex Red) to fluorophore resorufin (λ_{ex} = 550 nm; λ_{em} = 590 ~ 650 nm) catalyzed by horseradish peroxidase (HRP)[49]. Under the similar setup mentioned above (Fig. S7), the emission intensities of resorufin (I_f), hence the local $[H_2O_2]$ value, were determined for Au-coated wire array electrode under the confocal microscopy, assisted by the corresponding calibration curves (Fig. S2.9 to Fig. S2.12, see "Materials and Methods" section). When $\boldsymbol{k}$ = (15, 4, 50) for the wire array (Fig. 32.B and 32.C), the three-dimensional I_f mapping was similarly recorded in a time sequence when the Au-coated wire array was initially under an open-circuit condition (t < 20 sec), subject to an electrochemical potential (E_{appl} = 0.5 V *vs.* RHE) from t = 20 and 50 sec, and reverted back to the open-circuit condition when t > 50 sec (see "Materials and Methods" section). The side-views of the three-dimensional If mapping was also displayed when E_{appl} was initially absent (t = 0 sec), E_{appl} = 0.5 V *vs.* RHE (t = 22 sec), and E_{appl} was absent again at t = 52 s ("t = 0 sec", "t = 22 sec", and "t = 52 sec" in Fig. 2.3B, respectively). While the absence of E_{appl} correlates with the absence of fluorescent emission from resorufin ("t = 0 sec" and "t = 52 sec" in Fig. 2.3B), the

presence of E_{appl} = 0.5 V vs. RHE ("t = 22 sec" in Fig. 2.3B) yielded significant fluorescent emission near the wire array that suggested electrochemical generation of H_2O_2. Meanwhile, concurring monitoring of [O_2] suggests that the local [O_2] are not significantly perturbed (Fig. S2.13A) due to the relatively lower current density of ORR on the Au-based electrocatalysts under similar E_{appl} values (Fig. S2.4 and S2.5). This suggests that the electrochemically controlled H_2O_2 gradient is nearly independent to aeration of the liquid medium, thanks to the catalytically selective generation of H_2O_2 and the low value of observed [H_2O_2] (at most up to 30 μM) relevant for biological studies[8, 48, 50] in comparison to the air-saturated O_2 solubility in water (246 μM).[45]

The averaged change of [H_2O_2] values ([H_2O_2]$_{avg}$) at different distances above the bottom of the wire array z = 5, 50, 90 μm were quantified and displayed as a function of time t in Fig. 2.3C. At all z values, the time-dependent generation of [H_2O_2]$_{avg}$ measured from I_f were well correlated with the presence of E_{appl}. A more gradual yet still relatively fast transition of the measured I_f (~10 sec) hence [H_2O_2]$_{avg}$ were observed, which was presumably due to limited temporal resolution of the fluorogenic reaction that was needed to track local [H_2O_2].[51] Nonetheless, such data indicated the capability of temporally controlling the formation of H_2O_2 electrochemically, which can be handy as a perturbation to study the microbial response towards H_2O_2 -based ROS.[52] We also determined the electrochemically induced H_2O_2 gradient for wire array $\boldsymbol{k}$ = (15, 4, 50) at E_{appl} = 0.45, 0.5, and 0.55 V vs. RHE (black, red, and blue in Fig. 2.3D, respectively). Significantly, different local accumulation of H_2O_2 up to 30 μM for different E_{appl} values were observed despite the 50 mV change of E_{appl}. Such observation suggests that the generated H_2O_2 gradient is highly sensitive and subsequently tunable by electrochemical driving forces. In addition, the morphology of wire array electrodes impacts the generated H_2O_2 gradient. The characterized H_2O_2 gradients for $\boldsymbol{k}$ = (15, 4, 50), (30, 3, 50), and (15, 4, 20) (black, red, and blue in Fig. 2.3E, respectively) were

noticeably different at the same E_{appl} = 0.5 V vs. RHE. The achievable range of H_2O_2 gradients at the microscopic level is commensurate with biologically observed ROS microenvironments,[8] heralding the utility of the electrochemically generated H_2O_2 gradients in microbial studies.

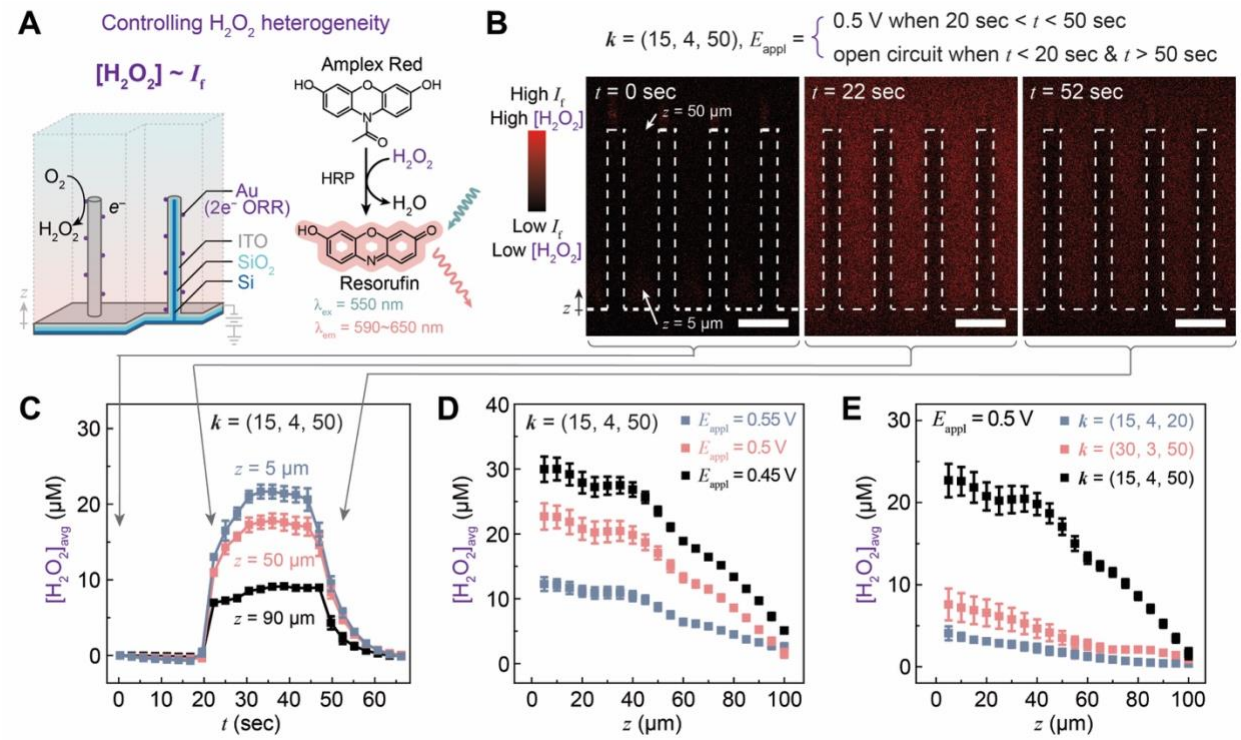


Figure 2.3. Spatiotemporal control of H_2O_2 gradient on Au-loaded microwire array. A, Design of Au-loaded microwire array and the fundamentals of spatiotemporal mapping local H_2O_2 concentrations ($[H_2O_2]$) based on the intensity of fluorescence emission (I_p) in the fluorogenic reaction from Amplex Red to resorufin catalyzed by horseradish peroxidase (HRP). **B** and **C**, Cross-sectional I_f profiles on wire array $\boldsymbol{k}$ = (15, 4, 50) at t = 0, 22, and 52 secs (**B**) and the subsequent temporal evolution of averaged local H_2O_2 concentrations ($[H_2O_2]_{avg}$) at different distances z from the base of wire array (**C**). The values of E_{appl} is against RHE. The microwires are depicted in dashed lines in **B**. Scale bars are 15 μm. **D**, Plots of $[H_2O_2]_{avg}$ versus z under different values of E_{appl} for wire array $\boldsymbol{k}$ = (15, 4, 50). **E**, Plots of $[H_2O_2]_{avg}$ versus z in wire arrays of different

$\boldsymbol{k}$ when E_{appl} = 0.5 V. Error bars represent standard deviations across multiple separate measurements in the device ($n \geq 3$).

Establishing neural networks for an inverse design strategy

We seek to establish computational models that can inversely predict the values of E_{appl} and $\boldsymbol{k}$ = (P, D, L) of the Pt- and Au-loaded wire array electrodes for targeted corresponding O_2 and H_2O_2 gradients ([O_2](z) and [H_2O_2](z)), respectively. Such an inverse design strategy of O_2 and H_2O_2 microenvironments is proposed to be much more time-efficient in comparison with the classical trial-and-error approach (Fig. 2.4A), and will find plentiful applications given the high variabilities of biological applications in both spatial and temporal domains.[2, 3, 8] Critical inside such computational models are neural networks, trained with sufficient amounts of data, which correlate {E_{appl}, $\boldsymbol{k}$ = (P, D, L)} with the [O_2](z) and [H_2O_2](z) distributions. In such a regard, we employed numerical simulations based on finite-element methods (FEM)[32] to augment the available data (Fig. 2.4B). FEM-based electrochemical simulations have been widely used in the understanding and design of electrochemical applications with satisfactory accuracies.[32,33, 53-55] We established electrochemical microkinetic models that include the mass transport of redox species and the electrochemical reduction of O_2 for the Pt and Au electrocatalysts (see "Materials and Methods" section). FEM-based numerical simulations were conducted with COMSOL Multiphysics (version 5.3) for the O_2 and H_2O_2 gradients near the Pt- and Au-loaded wire array electrodes, respectively. Experimental $[O_2]_{avg}$ and $[H_2O_2]_{avg}$ values were compared with simulation results at different heights above the base of wire array (z), as shown in the exemplary case when consistent results of O_2 and H_2O_2 gradients were observed for $\boldsymbol{k}$ = (30, 3, 50) and E_{appl} = 0.5 V vs. RHE (Fig. S2.13B and Fig. S13C). The mean squared errors (MSEs) between FEM-based simulations and experimental results are 9.81×10^{-4} mM^2 and 4.84×10^{-6} mM^2 for O_2 and H_2O_2 gradients,

respectively (see "Materials and Methods" section). Such consistence of results between experimental characterization and FEM-based simulations motivates us to use the augmented data from FEM-based simulations to establish neural networks to inversely predict O_2 and H_2O_2 gradients.

The established neuron networks display good accuracies for the $[O_2](z)$ and $[H_2O_2](z)$ distributions near the wire array electrodes loaded with Pt and Au electrocatalysts. We previously constructed multi-layer perception neuron networks (MLPNNs) that expand the explorable parameter space of wire array electrode morphologies in electrocatalytic reduction of N2.34 Here, we constructed MLPNNs that predicts $[O_2](z)$ and $[H_2O_2](z)$ based on inputs of $\{E_{appl}, \boldsymbol{k} = (P, D, L)\}$, which were trained based on 10,000 data points augmented from the FEM-based simulations (see "Materials and Methods" section). As model-training process proceeds with an increasing number of epochs, monotonic decreases of the average MSE between the training and predicted data points (AMSE) for both the data sets of validation and training (red and black dots, respectively) were observed in Fig. 2.4C and 2.4D for the O_2 and H_2O_2 gradients near Pt- and Au-loaded wire array electrodes, respectively. The fact that the values of AMSEs against the validation date sets were similar to the ones from the training date sets in Fig. 2.4C and 2.4D indicates that there was no overfitting in the machine-learning process.[56] In the end, near-unity coefficients of determination ($R^2 \rightarrow 1$) were observed for both MLPNNs (MLPNN 1 that predict O_2 gradients and MLPNN 2 that predict H_2O_2 gradients) (Fig. 2.4E and 2.4F, respectively). The values of AMSEs from the MLPNNs reach 1.74×10^{-4} mM^2 and 1.81×10^{-6} mM^2 for the prediction of $[O_2](z)$ and $[H_2O_2](z)$ based on inputs of $\{E_{appl}, \boldsymbol{k} = (P, D, L)\}$, respectively. Such small values of AMSEs suggest good accuracies of the developed neural networks for the inverse design of desirable O_2 and H_2O_2 microenvironments.

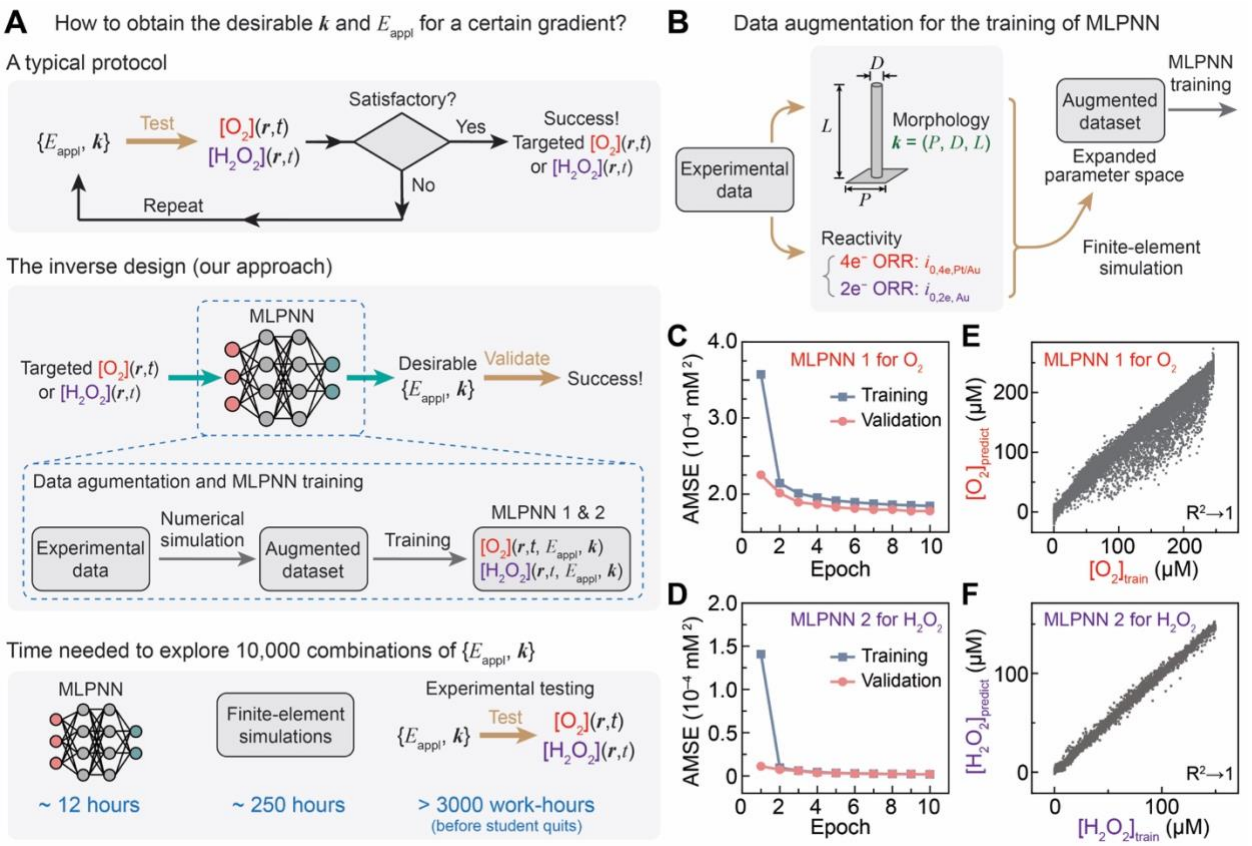


Figure 2.4. The development of inverse design for electrochemically generated O_2 and H_2O_2 gradients. A, Comparison between the conventional protocol and our inverse design approach for the development of suitable experimental conditions, represented as $\{E_{appl}, \boldsymbol{k}\}$, in order to achieve desirable spatiotemporal distributions of O_2 and H_2O_2 concentrations ($[O_2](\boldsymbol{r}, t)$ and $[H_2O_2](\boldsymbol{r}, t)$, respectively). MLPNN 1 & 2, multiple-layer perceptron neural networks for O_2 and H_2O_2 gradients, respectively. **B**, Protocols of data augmentation for the establishment of MLPNN. $i_{0,4e,Pt/Au}$ and $i_{0,2e,Au}$, the exchange current densities of four-electron and two-electron ORRs on Pt and/or Au electrocatalysts. **C** and **D**, The average mean squared error (AMSE) in the training (blue) and validation (pink) datasets at different epochs for the gradients of O_2 (MLPNN 1 in **C**) and H_2O_2 (MLPNN 2 in **D**). **E** and **F**, Comparisons between the MLPNN-predicted values ($[O_2]_{predict}$ and

$[H_2O_2]_{predict}$) and training values ($[O_2]_{train}$ and $[H_2O_2]_{train}$) for the local average concentrations of O_2 (**E**) and H_2O_2 (**F**), respectively. R^2, coefficient of determination.

Exemplary inverse design of O_2 and H_2O_2 microenvironments near wire array electrodes

Exemplary inverse design processes with direct biological relevance were experimentally tested with good predictabilities for the establishment of desirable O_2 and H_2O_2 microenvironments. In microbiology and microbial ecology, it is desirable to establish well-defined microenvironments whose sizes are 20~100 μm in order to mimic natural heterogenous distribution of biologically relevant extracellular species such as nutrients and other microbial resources.[57] Within such length scales, establishing microoxic niche (i.e. $[O_2]$ ~ 100 μM) in the midst of an oxic external environment (Fig. 2.5A), prevalent in aquatic, terrestrial, and host-associated environments, is challenging yet desirable to understand the physiology and ecology of microaerophiles and advance our understanding of microbiomes;[2] extracellular H_2O_2 whose concentration can achieve 15 μM[58] (Fig. 2.5B) is also of particular interests in order to study microbial sensing, communal signaling, metabolic regulation, and genetic expression towards ROS.[48, 59] In such biological contexts, we aim to inversely design one O_2 gradient ($\Delta[O_2]$ ~ 100 μM and Δz ~ 40 μm) and one H_2O_2 gradient ($\Delta[H_2O_2]$ ~ 15 μM and Δz ~ 100 μm) based on our developed MLPNNs (Fig. 2.5A and 2.5B). We utilized the established MLPNNs that predict $[O_2](z)$ and $[H_2O_2](z)$ under different inputs of $\{E_{appl}, \boldsymbol{k} = (P, D, L)\}$ and we scored the similarity percentages between the MLPNNs-predicted O_2 and H_2O_2 gradients and the desirable ones. Fig. 2.5C and 2.5D exemplarily display the sliced mappings of similarity scores for the aforementioned O_2 and H_2O_2 gradients on Pt and Au-loaded wire arrays, respectively, as a function of $\boldsymbol{k} = (P, D, L)$ at E_{appl} = 0.5 V vs. RHE. Such a multi- dimensional mapping, composed of 10,000 data points each in Fig. 2.5C and 2.5D, showcases the parameter spaces that are predicted to yield the desirable O_2 and H_2O_2

microenvironments within a certain relative uncertainty threshold (red region) (see "Materials and Methods" section). It is intriguing to note that there existed multiple different wire array morphologies to yield the same desirable O_2 and H_2O_2 gradients, which may not be straightforward intuitively. We estimated that the determination of O_2/H_2O_2 gradients for one parameter coordinate in the space of $\{E_{appl}, \boldsymbol{k} = (P, D, L)\}$ will take ~4 sec for the MLPNNs-based method, ~90 sec from FEM-based simulations, and ~20 mins for the confocal characterization alone at one specific E_{appl} for a single wire-array morphology notwithstanding any time spent in any preceding protocols (see "Materials and Methods" section). Therefore, a comprehensive exploration of the parameter space $\{E_{appl}, \boldsymbol{k} = (P, D, L)\}$ with more than 10^4 trials as shown above is only possible with the use of MLPNN-based inverse design, because only the MLPNN is capable of screening 10,000 parameter combinations within a reasonable amount of time in practice (~12 hours) in comparison to the ones based on FEM (~250 hours, i.e. ~10 days) and experimental characterization (at least 3000 work-hours without considering any practical concerns) (Fig. 2.4A).

We also conducted a spot check for the predicted O_2 and H_2O_2 microenvironments by experimentally validations. Pt-based wire array electrode with $\boldsymbol{k}$ = (46, 6, 20) was picked from Fig. 2.5C as a desirable geometry, experimentally prepared (Fig. 2.1E), and experimented tested for the established O_2 gradient at E_{appl} = 0.5 V *vs.* RHE. Satisfactory consistency with MSE = 5.63×10^{-4} mM^2 was achieved between the experimental and targeted values of $[O_2](z)$ (dots and line in Fig. 2.5E, respectively). Similarly, Au-based wire array electrode with k = (17, 3, 30) was picked from Fig. 2.5D, experimentally prepared (Fig. 2.1E), and experimented tested for the H_2O_2 gradient at E_{appl} = 0.45 V *vs.* RHE. We also observed satisfactory consistency with MSE = 7.22×10^{-6} mM^2 between the experimental and targeted values of $[H_2O_2](z)$ (dots and line in Fig. 2.5F, respectively). While we were unable to experimentally exhaust all of the predicted parameter space

for the desirable microenvironments of O_2 and H_2O_2, our experimental validations offer convincing evidence for the validity of the developed MLPNN-based inverse design for future microbiology-related research.

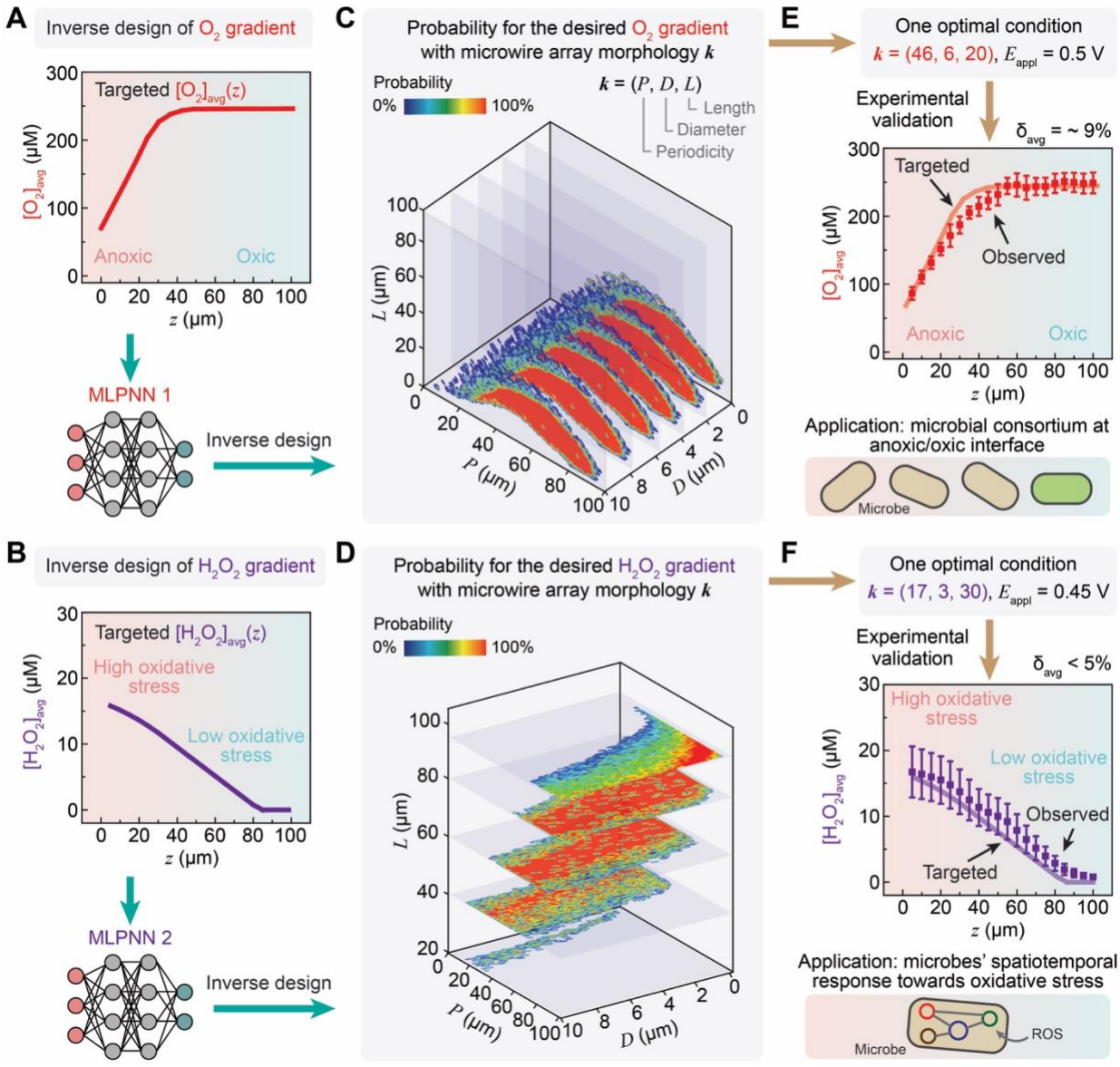


Figure 2.5. Experimental validations of MLPNN-assisted inverse design. A and **B**, Targeted O_2 and H_2O_2 gradients ($[O_2]_{avg}(z)$ in **A** and $[H_2O_2]_{avg}(z)$ in **B**, respectively) for exemplary inverse design assisted by the developed MLPNNs. **C** and **D**, the three-dimensional contour plots of the probabilities that MLPNN-predicted $[O_2]_{avg}(z)$ (**C**) and $[H_2O_2]_{avg}(z)$ (**D**) match the targeted ones as

a function of P, D, L when E_{appl} = 0.5 V *vs.* RHE. **E** and **F**, Experimental characterizations of $[O_2]_{avg}(z)$ and $[H_2O_2]_{avg}(z)$ (scattered points) in comparison with the targeted ones (lines) when $\{E_{appl}, \boldsymbol{k}\}$ = (0.5, 46, 6, 20) in **E** and (0.45, 17, 3, 30) in **F** on Pt- and Au-loaded microwire arrays, respectively. The potential applications of those yielded gradients in microbiology are noted. Error bars represent standard deviations across multiple separate measurements in the device ($n \geq 3$).

Conclusion

In summary, we presented an ML-based inverse design strategy of O_2 and H_2O_2 concentration profiles with the use of electrochemical catalysis of ORR. We demonstrated a proof-of-concept closed-loop protocol of inversely designing O_2 and H_2O_2 gradients with properly designed microwire electrodes in PBS solution, the go-to culturing medium in microbiology. By achieving concentration differences and spatial resolutions that are relevant to microbial microenvironments, the demonstrated O_2 and H_2O_2 gradients are applicable for studies in microbiology. While the reported research focuses on one specific form of electrochemical boundary conditions, namely microwire array, the reported inverse-design procedures are generally applicable for any electrochemical systems that can be parameterized and analyzed by neural networks. As mass transport and concentration profiles in electrode's proximity are important components in electrochemistry, this work demonstrates the power of machine-learning-based inverse design in electrochemistry. Moreover, our results will lead to a general platform that inversely design suitable electrochemical systems for any targeted environments of O_2 and H_2O_2 in microbiology. Future research will focus on the platform's application of in vivo microbial communities and fundamental insights that can be fetched thanks to our system's unique capabilities. Moreover, since electrochemistry is capable of modulating any redox active species such as extracellular Fe(II)/(III) species,[60] as well as other extracellular metabolites sensitive

towards oxidative stress such as pyocyanin,[61-63] our inverse design approach based on electrochemistry is capable of controlling the other microenvironments beyond O_2 and ROS and is generally applicable in the study of ubiquitous microenvironments in extracellular medium.

Materials and Methods

Chemicals

Indium-doped tin oxide (ITO)-coated glass slide (06499-AB) was purchased from SPI Supplies (30 ~ 60 Ω, 22 × 40 mm). Silver (Ag) paste (16040-30) was purchased from Ted Pella. Si wafers (*p*-type, boron-doped, <100>, 1~10 Ω•cm^{-1}) were purchased from University Wafer, Inc. Platinum (Pt) wires (CHI 115) and glassy carbon electrodes (CHI 104, diameter = 3 mm) were purchased from CH Instruments. Unless specially mentioned, all chemicals and materials were purchased from Sigma-Aldrich or VWR.

Experimental establishment of testing platform

Modified from a previously published protocol,[29] the experimental testing platform as shown in Fig. S2.7 consists of a fluidic cell with a three-electrode system, in order to electrochemically generate desirable gradients of O_2 and H_2O_2. As the working electrode in the setup, microwire array electrodes were fabricated similarly as previously described.[29] The microwire arrays were fabricated by photolithography with the use of deep reactive-ion etching process (DRIE). After treated in hexamethyldisilazane (HMDS) vapor for 10 minutes, pre-cleaned Si wafers were coated by photoresist (MicroChemicals, AZ5214E; 3000 rpm spin-coating) with a soft baking (100 °C for 75 sec), exposed in the hard contact mode by a contact aligner (Carl Suss MA6), hard-baked (120 °C, 5 min), and developed to generate the periodic patterns for the array (mixture of MicroChemicals AZ400K water, 1:4 volume ratio). After created by DRIE (Unaxis Versaline

FDSE III), microwire arrays of desirable lengths were annealed under ambient air at 1050 °C for 9.5 hours to yield the insulating oxide layer, coated by 500-nm ITO through reactive sputtering (Denton Discovery 550 sputtering System), and finally deposited with a 2-nm layer of Pt or Au by a Anatech Hummer 6.2 sputtering system. The structure of wire array and the element distribution were examined by a SEM (JEOL JSM-6700F) equipped with energy dispersive X-ray spectroscopy (EDS, Ametek). Patterned ITO-coated glass slides were used as the counter electrodes in the established testing platform, after the selective removal of ITO by 6 M HCl = in undesirable areas on the glass slides. Ag paint as the pseudo-reference electrode was applied on select area of the ITO-coated slides as to cover a 5 mm × 5 mm square with a layer of silver, serving as the reference electrode, while Pt was deposited on other ITO-coated areas for the creation of counter electrode in the setup. An optically transparent fluidic cell of 250-μm-large height was constructed by assembling the microwire array electrodes with the pre-fabricated ITO glass slides, while a Gamry Interface 1010B potentiostat was used to enforce electrochemical driving force. The setup was mounted on an inverted laser confocal microscope (Leica SP8 SMD) with sufficient working distance (680 μm) and syringe pump was used to maintain a fixed iquid flow rate. As we particularly ensure the accuracy of applied electrochemical potentialscyclic voltammetry in a standard ZoBell's solution (3.3 mM $K_3Fe(CN)_6$, 3.3 mM $K_4Fe(CN)_6$, and 0.1 M KCl, 0.43 V vs. Standard Hydrogen Electrode (SHE)) was employed to calibrate the electrochemical potential of Ag-based pseudo reference electrode as shown in Fig. S14.[64, 65] The Ag-based pseudo-reference electrode was calibrated as 0.75 V *vs.* RHE in PBS solution at pH = 7.4.

Electrochemical characterization of the deposited electrocatalysts

While the deposited Pt electrocaalysts have been characterized in our prior report,[15] experiments were conducted to analyze the electrocatalytic activities of ORR for the coated Au electrocatalysts. An experiment of rotating ring-disk electrode (Pine Research, Inc., AFE6R1PT) was conducted in PBS solution using a setup with a Pt-wire counter electrode, Ag/AgCl (1M KCl) reference electrode and a modulated speed rotator (Pine Research, Inc., AFMSRCE). While Pt ring electrode was kept at 1.9 V vs. RHE, linear scan voltammograms (20 mV/s) were recorded between 0.4 V and 1.4 V vs. RHE with different rotating speeds (100 rpm, 225 rpm, 400 rpm, 625 rpm, 900 rpm, 1225 rpm, 1600 rpm, and 2025 rpm) in electrolytes saturated with O_2 and N_2, respectively. The measurements in N_2-saturated solution were used as signal background.

Quantification and calibration of O_2 concentration profiles

Aerated PBS solution consisting of 150 μM $Ru(phen)_3Cl_2$ solution was prepared in the dark, and fed into the assembled testing platform at a flow rate of 0.8 mL/min. The phosphorescence intensity mapping under the confocal microscopy was measured in a one-minute time sequence. During the one-minute confocal microscopy measurement, a programmed 30-sec electrolysis with a particular potential on the working electrode from t = 15 sec to t = 45 sec. The excitation wavelength was set as 470 nm and we gathered emission intensity from 600 nm to 640 nm as phosphorescence emission intensity I_p. We defined the phosphorescence emission intensity with no potential applied as I_0. Normalized phosphorescence emission intensity I_{pn} was defined as $I_{pn} = I_p/I_0$. The phosphorescence emission intensity distribution was further translated into the concentration profiles based the linear relationship between O_2 concentration and I_{pn} that was experimentally determined. $Ru(phen)_3Cl_2$-containing PBS solutions of different O_2 concentrations, ranging from $[O_2]$ = 25 μM to 375 μM, was prepared by bubbling N_2/O_2 mixture of tunable ratio through the solution, and pumped into the assembled fluidic device (0.8 mL/min) for calibration.

Quantification and calibration of H_2O_2 concentration profiles

Aerated PBS solution consisting of 0.2 U/mL HRP and 120 μM Amplex Red (1× working solution) was prepared in the dark, and fed into the assembled testing platform at a flow rate of 0.8 mL/min. The fluorescent intensity mapping under the confocal microscopy was conducted in a one-minute time sequence. During the one-minute confocal microscopy measurement, a programmed 30-sec electrolysis with a particular potential on the working electrode from t = 20 sec to t = 50 sec. The excitation wavelength was set as 550 nm and we gathered emission intensity from 590 nm to 650 nm as fluorescence emission intensity I_f. The fluorescence emission intensity distribution was further translated into the concentration profiles based on the corresponding calibration curves. In the experiments of calibrating H_2O_2 concentrations, darkly prepared PBS solution consisting of 0.4 U/mL HRP and 240 μM Amplex Red was combined with PBS solution of different H_2O_2 concentrations, ranging from 5 μM to 60 μM, and was pumped into the assembled devices for the measurement of confocal microscopy. We found that the H_2O_2-induced fluorescence intensity I_f is also dependent on the specific morphologies of wire array ($\boldsymbol{k}$) and the distance away from the bottom of wire array (z) (Fig. S15). Therefore, individual calibration curves were determined for every z locations in wire arrays with all possible $\boldsymbol{k}$ values (Fig. S9-S12). Specific I_f correction was made to compensate the difference between calibration experiment and gradient optical detection due to practical restriction (Supplementary note 1, Fig. S16).

FEM-based numerical simulations for O_2 gradient and H_2O_2 gradients

FEM simulation of both O_2 gradient and H_2O_2 gradient was achieved in "electroanalysis" module in COMSOL Multiphysics (Version 5.3).

Geometry description: The shape of wire was represented by a column with diameter of D and length of L. We located each wire in the center a cuboid of $P \times P \times 200$ μm and the difference

between the cuboid and column was geometrically defined the electrolyte. For each point in the electrolyte, if its distance from the top of the wire not smaller than the diffusion distance, d_{D}, we considered it belonged to the bulk electrolyte in which [O_2] = 246 μM independent of time. The boundary surface was defined as the area of which the distance to the top of the wire is d_{D}. On the boundary surface, the [O_2] was the same as that in the bulk. Periodic boundary condition was applied to describe the wire array. The value of d_{D} was set as 20 μm for O_2 gradient simulation on Pt-loaded wire array electrodes.[29] For O_2 gradient and H_2O_2 gradient simulation on Au-loaded wire array electrodes, d_{D} was measured as 50 μm (Fig. S17).

Transport properties: The diffusion of oxygen and hydrogen peroxide was simulated based on the following equations (1) and (2). $D_{\mathrm{O_2}}$ and $D_{\mathrm{H_2O_2}}$ are the diffusion coefficients of oxygen and hydrogen peroxide in aqueous solution, which were 2.2×10^{-9} m^2/s and 1.5×10^{-9} m^2/s respectively.

$$\frac{\partial[\mathrm{O_2}]}{\partial t} = D_{\mathrm{O_2}}\nabla^2[\mathrm{O_2}] \qquad (1)$$

$$\frac{\partial[\mathrm{H_2O_2}]}{\partial t} = D_{\mathrm{H_2O_2}}\nabla^2[\mathrm{H_2O_2}] \qquad (2)$$

Electroanalysis: The potential window of E_{appl} is from 0.6 V *vs.* RHE to 0.2 V *vs.* RHE.

On the surface of Pt-loaded wire array electrodes, 4e-ORR took place within the potential window.

$$O_2 + 4H^+ + 4e^- \rightarrow 2H_2O$$

On the electrode surface of Au-loaded wire array electrodes, 2e-ORR and 4e-ORR took place at the same time with potential-dependent selectivity.

$$\text{2e-ORR: } O_2 + 2H^+ + 2e^- \rightarrow H_2O_2$$

$$\text{4e-ORR: } O_2 + 4H^+ + 4e^- \rightarrow 2H_2O$$

On the surface of Pt-loaded wire array electrodes, the supply-consumption equilibrium was simulated as the equations (3) and (4) in the formalism of concentration-dependent Tafel kinetics,[27]

$$i_{\mathrm{loc}} = i_{4\mathrm{e}} = -i_{0,4\mathrm{e,Pt}} \frac{[\mathrm{O_2}]}{C_{\mathrm{O_2}}} \exp\left(\frac{-\alpha_c F \eta_{\mathrm{Pt}} n_{4\mathrm{e}}}{\mathrm{RT}}\right) \qquad (3)$$

$$J_{\mathrm{O_2}} = \frac{i_{\mathrm{loc}}}{4\mathrm{F}} \qquad (4)$$

Here $i_{4\mathrm{e}}$ denotes the current density of 4e-ORR, $i_{0,4\mathrm{e,Pt}}$ denotes the exchange current density of 4e-ORR, i_{loc} denotes the local current density of 4-electron reduction of O_2 on the electrode surface, $J_{\mathrm{O_2}}$ denotes the local flux of O_2 consumption from electrolyte, and η_{Pt} is the over potential that is defined as the difference between E_{appl} and the standard redox potential of O_2/H_2O, $E^0_{\mathrm{O_2/H_2O}}$ (1.23 V *vs.* RHE). The α_c equals 0.5 as the transfer coefficient, *F* denotes the Faraday constant, *R* is the gas constant, *T* is the temperature, and $n_{4\mathrm{e}}$ is electron transfer number before the rate determining step of 4e-ORR, of which the value is 1 (Fig. S4). The local oxygen concentration is denoted as $[O_2]$. $C_{\mathrm{O_2}}$ is oxygen concentration in air-saturated water at *T*. The above equation follows the textbook equations that accounting for the mass transport and chemical stoichiometry at electrode interfaces.[27] On Pt- loaded wire array electrodes, $i_{0,4\mathrm{e,Pt}}$ is found to be 3.0×10^{-6} A/m^2 (Fig. S2.4).

On the electrode surface of Au-loaded wire array electrodes, the supply-consumption equilibrium was simulated as the equations (5)-(7).

$$i_{\mathrm{loc}} = i_{4\mathrm{e}} + i_{2\mathrm{e}} = -i_{0,4\mathrm{e,Au}} \frac{[\mathrm{O_2}]}{C_{\mathrm{O_2}}} \exp\left(\frac{-\alpha_c F \eta_{\mathrm{Au}} n_{4\mathrm{e}}}{\mathrm{RT}}\right) - i_{0,2\mathrm{e,Au}} \frac{[\mathrm{O_2}]}{C_{\mathrm{O_2}}} \exp\left(\frac{-\alpha_c F \eta_{\mathrm{Au}} n_{2\mathrm{e}}}{\mathrm{RT}}\right) \quad (5)$$

$$J_{\mathrm{O_2}} = \frac{i_{4\mathrm{e}}}{4\mathrm{F}} + \frac{i_{2\mathrm{e}}}{2\mathrm{F}} \quad (6)$$

$$J_{\mathrm{H_2O_2}} = -\frac{i_{2e}}{2F} \quad (7)$$

While most of the definitions of variables in the case of Au-loaded wire array electrodes with equation (5), (6), and (7) are the same as the Pt-loaded case in equation (3) and (4), we noted that i_{loc} instead stands for the local current density of both 2-electron and 4-electron reduction of O_2 on the electrode surface, i_{2e}, the current density of 2e-ORR, and n_{2e} is electron transfer number before the rate determining step of 2e-ORR, of which the value is 0.7 (Fig. S5). On Au-loaded wire array electrodes, the catalysis selectivity of Au towards 4e-ORR and 2e-ORR are dictated by the exchange current densities $i_{0,4e,Au}$ and $i_{0,2e,Au}$ respectively. The $i_{0,4e,Au}$ is 2.0×10^{-8} A/m^2, and $i_{0,2e,Au}$ is 8.0×10^{-7} A/m^2, based on literature and measurement (Fig. S5).[69, 70]

Based on comparison with experimental gradients, the average mean squared error (AMSE) of O_2 gradient simulation and H_2O_2 gradient simulation on Pt-loaded wire array electrodes Au-loaded wire array electrodes is 1.05×10^{-3} mM^2 and 1.55×10^{-5} mM^2 respectively. The range of E_{appl} was set within the ORR potential windows, from 0.6 V *vs.* RHE to 0.2 V *vs.* RHE. Besides, a three-dimensional block was defined in the space of (P, D, L) as the range of morphology, from P = 1 to 100 μm, L = 1 to 150 μm, and D = 0.2 to 10 μm. By using Simulink in Matlab, we were able to generate random **k** value within the morphology space and calculate the corresponding gradient curves. To fulfill the machine learning functions, gradient profiles under 10000 experimental conditions were included in the dataset for each developed multiple-layer perceptron neural networks respectively.

Model selection and training

The implementation of all machine-learning code was done on on a MacBook Pro with a 1.4 GHz quad-core Intel Core i5 processor and 8GB of RAM, with code specifically deployed using the

JupyterLab Notebook, a Python-based programming platform widely used in data science and machine learning.[34] In this paper, we selected multi-layer perception neuron networks (MLPNNs) as the machine learning model for inverse design. We use FEM-simulated gradients to develop the MLPNNs. Gradient data was imported from FEM results in the form of .csv files and combined into library of data. Prior to the model development, a random 20% of the data was split from the whole dataset for later model validation. The rest of the data was split as training data and validation data of which the percentage were 65% and 15% respectively. Multiple cycles of model training, each cycle termed as one epoch, were conducted in order to develop the targeted MLPNNs. In each epoch, MLPNNs will be trained from the training data, followed by a validation process in the validation data set used to provide estimates of final model accuracy after each round of training. The total machine learning process will include ten epochs of forward and backward propagations. The accuracies of the developed MLPNNs model as a function of epoch numbers are plotted in Fig. 2.4C and 2.4D.

As described in the section above, the training data set was a collection of concentration gradient under different E_{appl} and $\boldsymbol{k}$ value. We used average mean squared error (AMSE) and standard deviation (SD), more detailly defined below from equations (8) to (11), to quantify the ability of machine learning models to correctly reveal the connection between gradient curves and the two impacting factors, E_{appl} and **k**. In model selection, we selected multiple-layer perceptron neural networks for gradient prediction due to the low AMSE and SD value gradient prediction (Fig. S2.18).

For both O_2 and H_2O_2 gradient, the predicted curve included 20 local concentration data along the wire array from Z = 5 μm to 100 μm every 5 μm. Z is defined as the distance from the bottom of wire array. In O_2 gradient prediction, MSE and SD are defined as the following equations.

$$\mathrm{MSE_O} = \frac{1}{20}\sum_{n=1}^{20}([\mathrm{O_2}]_{\mathrm{NNs}} - [\mathrm{O_2}]_{\mathrm{real}})^2 \quad (8)$$

$$\mathrm{SD_O} = \sqrt{\frac{1}{N}\sum_{n=1}^{N}\left(\mathrm{MSE_{O}}_n - \mathrm{AMSE_o}\right)^2} \quad (9)$$

In equations (8) and (9), $[\mathrm{O_2}]_{\mathrm{NNs}}$ stands for the predicted oxygen concentration from MLPNNs predicting O_2 gradient on Pt-loaded wire array. $[\mathrm{O_2}]_{\mathrm{real}}$ is the oxygen concentration in the simulation data set. $\mathrm{MSE_O}$ is defined based on the average square of concentration difference over the whole gradient profiles. $\mathrm{AMSE_o}$ is the average MSE over the whole data set. We calculated the SD over data under a wide range of experimental conditions to evaluate the overall precision of predictions from MLPNNs predicting O_2 gradient on Pt-loaded wire array.

MSE and SD in H_2O_2 gradient were defined in a similar pattern. In equations (10) and (11), $[\mathrm{H_2O_2}]_{\mathrm{NNs}}$ stands for the predicted oxygen concentration from MLPNNs predicting H_2O_2 gradient on Au-loaded wire array. $[\mathrm{H_2O_2}]_{\mathrm{real}}$ is the hydrogen peroxide concentration in the simulation data set. $\mathrm{MSE_H}$ is defined based on the average square of concentration difference over the whole gradient profiles. $\mathrm{AMSE_H}$ is the average MSE over the whole data set.

$$\mathrm{MSE_H} = \frac{1}{20}\sum_{n=1}^{20}([\mathrm{H_2O_2}]_{\mathrm{NNs}} - [\mathrm{H_2O_2}]_{\mathrm{real}})^2 \quad (10)$$

$$\mathrm{SD_H} = \sqrt{\frac{1}{N}\sum_{n=1}^{N}\left(\mathrm{MSE_{H}}_n - \mathrm{AMSE_H}\right)^2} \quad (11)$$

Morphology prediction for desired O_2 gradient and H_2O_2 gradient

In morphology prediction for desired O_2 gradient, we assigned the E_{appl} = 0.5 V *vs.* RHE. Initially, MLPNNs predicting O_2 gradient on Pt-loaded wire array randomly selected one morphology in the morphology space and calculated the corresponding O_2 gradient. The similarity score between the calculated O_2 gradient and target O_2 gradient, S_{O}, was quantified by equation (12). In the prediction process, the neural networks would find out the top 10,000 morphologies with highest S_{O} values. In equation (12), $[\mathrm{O_2}]_{\mathrm{T}}$ was the local oxygen concentration in the target O_2 gradient and $[\mathrm{O_2}]_{\mathrm{NNs}}$ was the calculated local oxygen concentration. Similarity score, S_O, is the average relative error among a collection of different z values, C_O. C_O = [5, 10, 15, 25, 35, 45, 70], unit is μm.

$$S_{\mathrm{O}} = 1 - 100\% \times \frac{1}{20}\sum_{\mathrm{n=1}}^{20} \frac{|[\mathrm{O_2}]_{\mathrm{NNs}} - [\mathrm{O_2}]_{\mathrm{T}}|}{[\mathrm{O_2}]_{\mathrm{T}}} \quad (12)$$

In morphology prediction for desired H_2O_2 gradient, we assigned the E_{appl} = 0.45 V *vs.* RHE. Initially, MLPNNs predicting H_2O_2 gradient on Au-loaded wire array randomly selected one morphology in the morphology space and calculated the corresponding H_2O_2 gradient. The similarity score between the calculated H_2O_2 gradient and target H_2O_2 gradient, S_{H}, was quantified by equation (13). In the prediction process, the neural networks would find out the top 10000 morphologies with highest S_{H} values. In equation (13), $[\mathrm{H_2O_2}]_{\mathrm{T}}$ was the local hydrogen peroxide concentration in the target H_2O_2 gradient and $[\mathrm{H_2O_2}]_{\mathrm{NNs}}$ was the calculated local hydrogen peroxide concentration. Similarity score, S_H, is the average relative error among a collection of different z values, C_H. C_H = [5, 20, 30, 40, 55, 70, 80], unit is μm.

$$S_{\mathrm{H}} = 1 - 100\% \times \frac{1}{20}\sum_{\mathrm{n=1}}^{20} \frac{|[\mathrm{H_2O_2}]_{\mathrm{NNs}} - [\mathrm{H_2O_2}]_{\mathrm{T}}|}{[\mathrm{H_2O_2}]_{\mathrm{T}}} \quad (13)$$

In the sliced mapping of H_2O_2 similarity score, the similarity score at L = 5 μm was the average of from L = 0 μm to 10 μm. The similarity score at L = 20 μm was the average of from L = 10 μm to 30 μm. The similarity score at L = 40 μm was the average of from L = 30 μm to 50 μm. The similarity score at L = 60 μm was the average of from L = 50 μm to 70 μm. gradient prediction. The similarity score at L = 80 μm was the average of from L = 70 μm to 90 μm. gradient prediction. The similarity score at L = 95 μm was the average of from L = 90 μm to 100 μm.

References

1. M. T. Madigan, J. M. Martinko, J. Parker, “Microbial Ecosystems” in Brock Biology of Microorganisms. 15th edition, M. T. Madigan, J. M. Martinko, J. Parker, (Pearson Prentice Hall, Upper Saddle River, NJ, 2018), pp. 651–686.
2. R. L. Morris, T. M. Schmidt, Shallow breathing: bacterial life at low O_2. *Nat. Rev. Microbiol.* **11,** 205−212 (2013).
3. P. S. Stewart, M. J. Franklin, Physiological heterogeneity in biofilms. *Nat. Rev. Microbiol.* **6,** 199−210 (2008).
4. T. J. Battin, K. Besemer, M. M. Bengtsson, A. M. Romani, A. I. Packmann, The ecology and biogeochemistry of stream biofilms. *Nat. Rev. Microbiol.* **14,** 251−263 (2016).
5. I. Guzmán-Soto et al., Mimicking biofilm formation and development: Recent progress in *in vitro* and *in vivo* biofilm models. *iScience* **24,** 102443 (2021).
6. J. M. Berg, J. L. Tymoczko, L. Stryer, G. J. Gatto Jr, “Oxidative Phosphorylation” in Biochemistry. 8th edition, J. M. Berg, J. L. Tymoczko, L. Stryer, G. J. Gatto Jr, (Macmillan, 2015), pp. 523–564.
7. D. de Beer, P. Stoodley, F. Roe, Z. Lewandowski, Effects of biofilm structures on oxygen distribution and mass transport. *Biotechnol. Bioeng.* **43,** 1131−1138 (1994).
8. J. A. Imlay, Where in the world do bacteria experience oxidative stress? *Environ. Microbiol.* **21,** 521−530 (2019).
9. Z. Lu, R. Sethu, J. A. Imlay, Endogenous superoxide is a key effector of the oxygen sensitivity of a model obligate anaerobe. *Proc. Natl. Acad. Sci. U.S.A.* **115,** E3266 (2018).
10. D. Klementiev Alexander, Z. Jin, M. Whiteley, R. Parsek Matthew, Micron scale spatial measurement of the O_2 gradient surrounding a bacterial biofilm in real time. *mBio* **11,**

e02536−20 (2020).

11. L. S. Downing, R. Nerenberg, Effect of oxygen gradients on the activity and microbial community structure of a nitrifying, membrane-aerated biofilm. *Biotechnol. Bioeng.* **101,** 1193−1204 (2008).

12. D. Dar, N. Dar, L. Cai, D. K. Newman, Spatial transcriptomics of planktonic and sessile bacterial populations at single-cell resolution. *Science* **373,** eabi4882 (2021).

13. M. Carmona et al., Monitoring cytosolic H_2O_2 fluctuations arising from altered plasma membrane gradients or from mitochondrial activity. *Nat. Commun.* **10,** 4526 (2019).

14. C. Virgile et al., Engineering bacterial motility towards hydrogen-peroxide. *PLoS One* **13,** e0196999 (2018).

15. D. M. Lewis, M. R. Blatchley, K. M. Park, S. Gerecht, O_2-controllable hydrogels for studying cellular responses to hypoxic gradients in three dimensions *in vitro* and *in vivo*. *Nat. Protoc.* **12,** 1620−1638 (2017).

16. P. C. Thomas, S. R. Raghavan, S. P. Forry, Regulating oxygen levels in a microfluidic device. *Anal. Chem.* **83,** 8821−8824 (2011).

17. M. Polinkovsky, E. Gutierrez, A. Levchenko, A. Groisman, Fine temporal control of the medium gas content and acidity and on-chip generation of series of oxygen concentrations for cell cultures. *Lab Chip* **9,** 1073−1084 (2009).

18. K. Campbell, A. Groisman, Generation of complex concentration profiles in microchannels in a logarithmically small number of steps. *Lab Chip* **7,** 264−272 (2007).

19. M. L. Rexius-Hall, G. Mauleon, A. B. Malik, J. Rehman, D. T. Eddington, Microfluidic platform generates oxygen landscapes for localized hypoxic activation. *Lab Chip* **14,** 4688−4695 (2014).

20. J. L. Moran, P. M. Wheat, N. A. Marine, J. D. Posner, Chemokinesis-driven accumulation of active colloids in low-mobility regions of fuel gradients. *Sci. Rep.* **11,** 4785 (2021).

21. J. F. Lo, E. Sinkala, D. T. Eddington, Oxygen gradients for open well cellular cultures via microfluidic substrates. *Lab Chip* **10,** 2394−2401 (2010).

22. H.-H. Hsu, P.-L. Ko, H.-M. Wu, H.-C. Lin, C.-K. Wang, Y.-C. Tung, Study 3D endothelial cell network formation under various oxygen microenvironment and hydrogel composition combinations using upside-down microfluidic devices. *Small* **17,** 2006091 (2021).

23. M. R. Blatchley, F. Hall, S. Wang, H. C. Pruitt, S. Gerecht, Hypoxia and matrix viscoelasticity sequentially regulate endothelial progenitor cluster-based vasculogenesis. *Sci. Adv.* **5,** eaau7518 (2019).

24. Y.-A. Chen et. al., Generation of oxygen gradients in microfluidic devices for cell culture using spatially confined chemical reactions. *Lab Chip* **11,** 3626−3633 (2011).

25. M. D. Brennan, M. L. Rexius-Hall, L. J. Elgass, D. T. Eddington, Oxygen control with microfluidics. *Lab Chip* **14,** 4305−4318 (2014).

26. D. B. Weibel, G. M. Whitesides, Applications of microfluidics in chemical biology. *Curr. Opin. Chem. Biol.* **10,** 584−591 (2006).

27. A. J. Bard, L. R. Faulkner, "MASS TRANSFER BY MIGRATION AND DIFFUSION" in Electrochemical Methods: Fundamentals and Applications, 2nd edition, A. J. Bard, L. R. Faulkner, (Wiley, New York, NY, 2000), pp. 137−155.

28. J. Huskens, S. O. Krabbenborg, Electrochemically Generated Gradients, *Angew. Chem. Int. Ed.*, **53,** 9152−9167 (2014)

29. S. Lu, X. Guan, C. Liu, Electricity-powered artificial root nodule. *Nat. Commun* **11,** 1505 (2020).

30. A. Géron, “Introduction to Artificial Neural Networks with Keras” in Hands-on machine learning with Scikit-Learn, Keras, and TensorFlow: Concepts, tools, and techniques to build intelligent systems, A. Géron, (O'Reilly Media, Inc., Sebastopol, CA, 2019), pp. 279−313.

31. A. Mansouri Tehrani et al., Machine learning directed search for ultraincompressible, superhard materials. *J. Am. Chem. Soc.* **140,** 9844−9853 (2018).

32. J. Newman, K. E. Thomas-Alyea, “NUMERICAL SOLUTION OF COUPLED, ORDINARY DIFFERENTIAL EQUATIONS” in Electrochemical systems, 3rd edition, J. Newman, K. E. Thomas-Alyea, (Wiley, New York, NY, 2012), pp. 611−634.

33. E. J. F. Dickinson, H. Ekström, E. Fontes, COMSOL Multiphysics®: Finite element software for electrochemical analysis. A mini-review. *Electrochem. Commun.* **40,** 71−74 (2014).

34. B. B. Hoar, S. Lu, C. Liu, Machine-learning-enabled exploration of morphology influence on wire-array electrodes for electrochemical nitrogen fixation. *J. Phys. Chem. Lett.* **11,** 4625−4630 (2020).

35. A. Kulkarni, S. Siahrostami, A. Patel, J. K. Nørskov, Understanding catalytic activity trends in the oxygen reduction reaction. *Chem. Rev.* **118,** 2302−2312 (2018).

36. D. Zhao et al., Atomic site electrocatalysts for water splitting, oxygen reduction and selective oxidation. *Chem. Soc. Rev.* **49,** 2215−2264 (2020).

37. J.-C. Dong et al., In situ Raman spectroscopic evidence for oxygen reduction reaction intermediates at platinum single-crystal surfaces. *Nat. Energy* **4,** 60−67 (2019).

38. T. Kumeda, H. Tajiri, O. Sakata, N. Hoshi, M. Nakamura, Effect of hydrophobic cations on the oxygen reduction reaction on single–crystal platinum electrodes. *Nat. Commun.* **9,** 4378 (2018).

39. S. C. Perry et al., Electrochemical synthesis of hydrogen peroxide from water and oxygen. *Nat. Rev. Chem.* **3,** 442−458 (2019).

40. J. L. Terrell et al., Bioelectronic control of a microbial community using surface-assembled electrogenetic cells to route signals. *Nat. Nanotechnol.* **16,** 688−697 (2021).

41. C. Xiang, A. C. Meng, N. S. Lewis, Evaluation and optimization of mass transport of redox species in silicon microwire-array photoelectrodes. *Proc. Natl. Acad. Sci. U.S.A.* **109,** 15622−15627 (2012).

42. C. Xiang et al., Modeling, simulation, and implementation of solar-driven water-splitting devices. *Angew. Chem. Int. Ed.* **55,** 12974−12988 (2016).

43. X.-d. Wang, O. S. Wolfbeis, Optical methods for sensing and imaging oxygen: materials, spectroscopies and applications. *Chem. Soc. Rev.* **43,** 3666−3761 (2014).

44. J. Varchola et al., Temperature and oxygen-concentration dependence of singlet oxygen production by RuPhen as induced by quasi-continuous excitation. *Photochem. Photobiol. Sci.* **13,** 1781−1787 (2014).

45. N. I. Kolev, "Solubility of O_2, N_2, H_2 and CO_2 in water" in Multiphase flow dynamics 4: Turbulence, Gas Adsorption and Release, Diesel Fuel Properties, N. I. Kolev, (Springer, Berlin Heidelberg, 2012), pp. 209−239.

46. M. Ackermann, A functional perspective on phenotypic heterogeneity in microorganisms. *Nat. Rev. Microbiol.* **13,** 497−508 (2015).

47. J. J. Harrison, H. Ceri, R. J. Turner, Multimetal resistance and tolerance in microbial biofilms. *Nat. Rev. Microbiol.* **5,** 928−938 (2007).

48. J. A. Imlay, The molecular mechanisms and physiological consequences of oxidative stress: lessons from a model bacterium. *Nat. Rev. Microbiol.* **11,** 443−454 (2013).

49. N. Schürmann et al., Myeloperoxidase targets oxidative host attacks to *Salmonella* and prevents collateral tissue damage. *Nat. Microbiol.* **2,** 16268 (2017).

50. L. C. Seaver, J. A. Imlay, Hydrogen peroxide fluxes and compartmentalization inside growing *Escherichia coli. J. Bacteriol.* **183,** 7182−7189 (2001).

51. G. H. Seong, J. Heo, R. M. Crooks, Measurement of enzyme kinetics using a continuous-flow microfluidic system. *Anal. Chem.* **75,** 3161−3167 (2003).

52. A. Sen, J. A. Imlay, How microbes defend themselves from incoming hydrogen peroxide. *Front. Immunol.* **12,** 667343 (2021).

53. M. F. Lagadec, R. Zahn, V. Wood, Characterization and performance evaluation of lithium-ion battery separators. *Nat. Energy* **4,** 16−25 (2019).

54. P. Peljo, M. D. Scanlon, T. J. Stockmann, Simulations employing finite element method at liquid|liquid interfaces. *Curr. Opin. Electrochem.* **7,** 200−207 (2018).

55. C. Lin, R. G. Compton, Understanding mass transport influenced electrocatalysis at the nanoscale via numerical simulation. *Curr. Opin. Electrochem.* **14,** 186−199 (2019).

56. T. Dietterich, Overfitting and undercomputing in machine learning. *ACM Comput. Surv.* **27,** 326−327 (1995).

57. R. Stocker, Marine microbes see a sea of gradients. *Science* **338,** 628−633 (2012).

58. N. S. Jakubovics, S. R. Gill, M. M. Vickerman, P. E. Kolenbrander, Role of hydrogen peroxide in competition and cooperation between *Streptococcus gordonii* and *Actinomyces naeslundii*. *FEMS Microbiol. Ecol.* **66,** 637−644 (2008).

59. Z. Lu, J. A. Imlay, When anaerobes encounter oxygen: mechanisms of oxygen toxicity, tolerance and defence. *Nat. Rev. Microbiol.* **19,** 774−785 (2021).

60. E. D. Melton, E. D. Swanner, S. Behrens, C. Schmidt, A. Kappler, The interplay of

microbially mediated and abiotic reactions in the biogeochemical Fe cycle. *Nat. Rev. Microbiol.* **12,** 797−808 (2014).

61. M. E. Hernandez, D. K. Newman, Extracellular electron transfer. *Cell. Mol. Life Sci.* **58,** 1562−1571 (2001).

62. A. Price-Whelan, L. E. P. Dietrich, D. K. Newman, Rethinking 'secondary' metabolism: physiological roles for phenazine antibiotics. *Nat. Chem. Biol.* **2,** 71−78 (2006).

63. E. K. Perry, L. A. Meirelles, D. K. Newman, From the soil to the clinic: the impact of microbial secondary metabolites on antibiotic tolerance and resistance. *Nat. Rev. Microbiol.* **20,** 129−142 (2022).

64. D. K. Nordstrom, Thermochemical redox equilibria of ZoBell's solution. *Geochim. Cosmochim. Acta* **41,** 1835–1841 (1977).

65. C. E. ZoBell, Studies on redox potential of marine Sediments. *AAPG Bull.* **30,** 477–513 (1946).

66. G. Shalev, S. W. Schmitt, G. Brönstrup, S. Christiansen, Maximizing the ultimate absorption efficiency of vertically-aligned semiconductor nanowire arrays with wires of a low absorption cross-section. *Nano Energy* **12,** 801−809 (2015).

67. H. Alaeian, A. C. Atre, J. A. Dionne, Optimized light absorption in Si wire array solar cells. *J. Opt.* **14,** 024006 (2012).

68. L. Yu et al., Understanding Light Harvesting in Radial Junction Amorphous Silicon Thin Film Solar Cells. *Sci. Rep.* **4,** 4357 (2014).

69. G. Gotti, D. Evrard, K. Fajerwerg, P. Gros, Oxygen reduction reaction features in neutral media on glassy carbon electrode functionalized by chemically prepared gold nanoparticles. *J. Solid State Electrochem.* **20,** 1539−1550 (2016).

70. C. Villena, J. Losada, B. Alonso, C. M. Casado, M. P. G. Armada, Easy preparation of electrode surfaces with dispersed size-controlled Au nanoparticles by electrodeposited PPI-dendrimers as templates. *J. Electrochem. Soc.* **164,** H396−H406 (2017).

Supplementary Information

Supplementary Notes

Note S2.1: Fluorescence intensity correction in H_2O_2 concentration calibration experiment

In the H_2O_2 concentration calibration experiment, H_2O_2 solution mixed with 2× working solution (PBS solution consisting of 0.4 U/mL HRP and 240 μM Amplex Red) in a mixing tee (IDEX, U-466). In the H_2O_2 gradient measurement experiment, the mixing area was the working electrode area. In the calibration experiment setup, it required extra time for liquid to travel from mixing tee to the working electrode resulting in higher fluorescence emission intensity in calibration experiments under the same H_2O_2 concentration. The relationship between increased fluorescence intensity and extra time was revealed by measuring the I_f difference between the upstream and downstream of the wire array electrode (Figure S2.15). In each calibration experiment, I_f was corrected based on the relationship.

Supplementary Tables

Table S2.1: Phosphate-buffered saline (PBS)

Component	Concentration (g/L)
NaCl	8
KCl	0.2
Na_2HPO_4	1.44
KH_2PO_4	0.24

Supplementary Figures

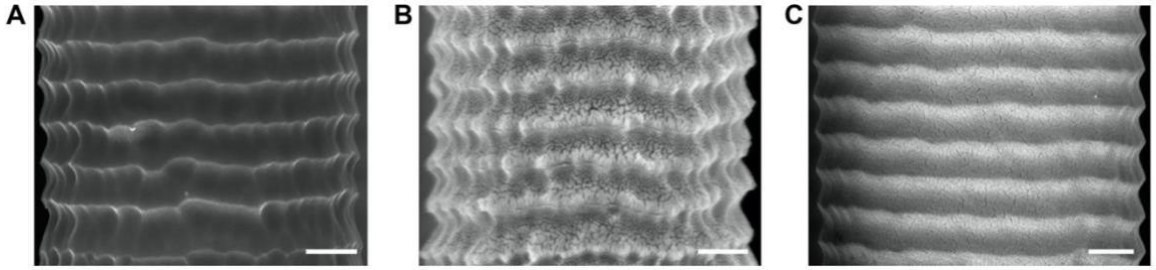


Figure S2.1. Scanning electron microscopy (SEM) images for the surface of wire array electrode without the deposition of Au/Pt catalysts (*A*), loaded with Pt electrocatalyst (*B*), and loaded with Au electrocatalyst (*C*). Scale bar, 500 nm.

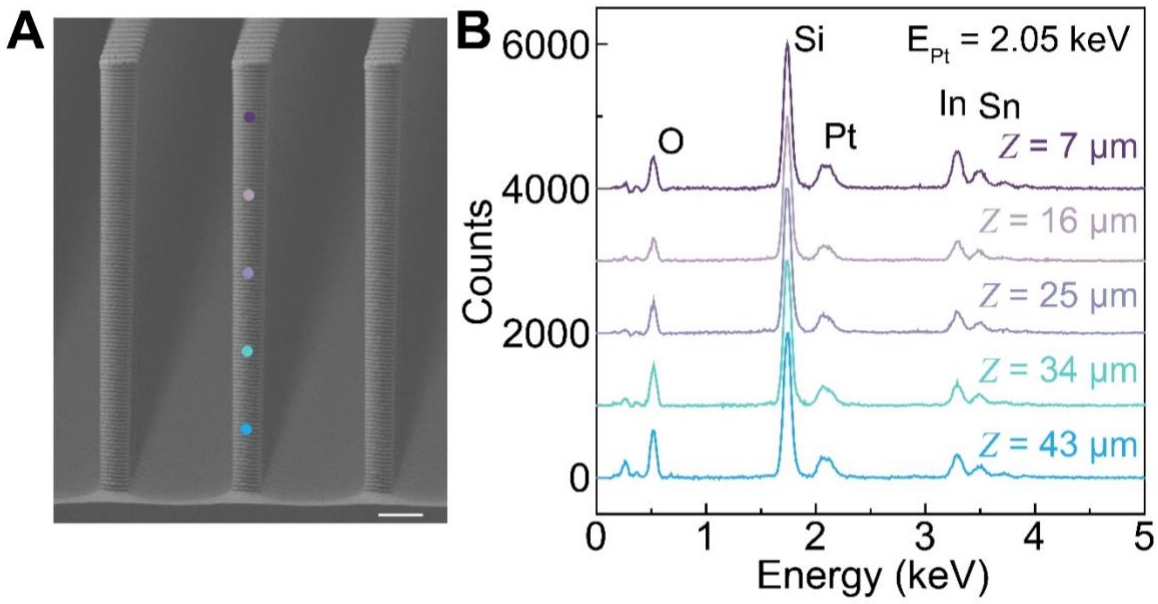


Figure S2.2. Morphological characterization of Pt-coated wire array electrodes with k = (15, 4, 50) A The cross-sectional scanning electron microscopy (SEM) image depicting the side view of wire array with **k** = (15, 4, 50) **B** Energy-dispersive X-ray spectroscopy (EDS) spectra taken at different height along the Pt-coated wire array in **A**. A homogenous distribution of Pt, In and Sn was observed along the prepared microwire array. Scale bar, 5 µm.

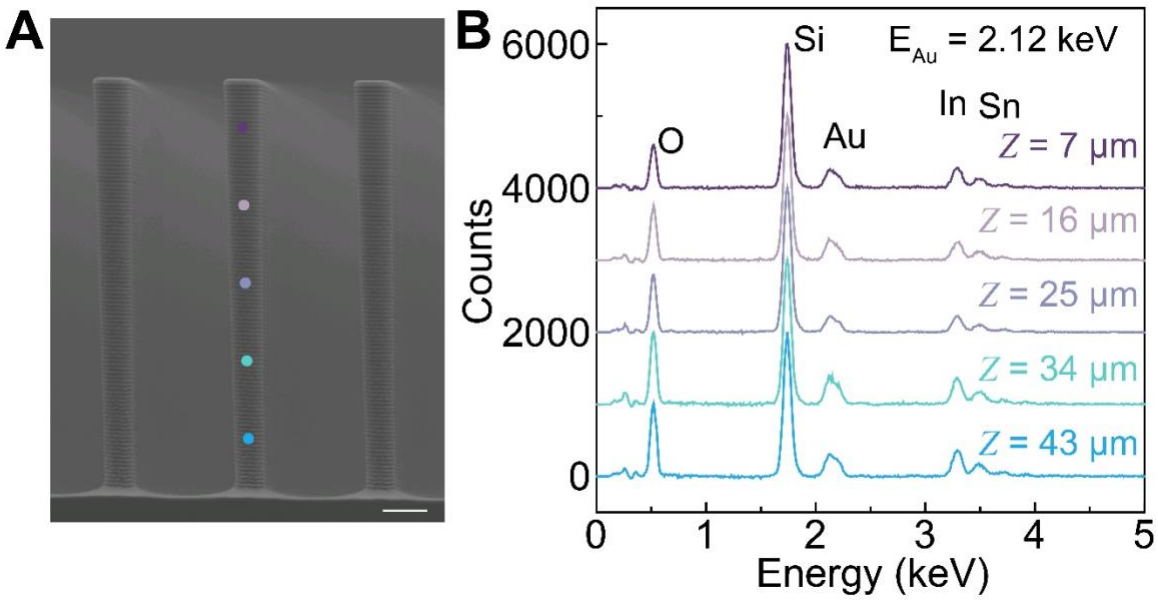
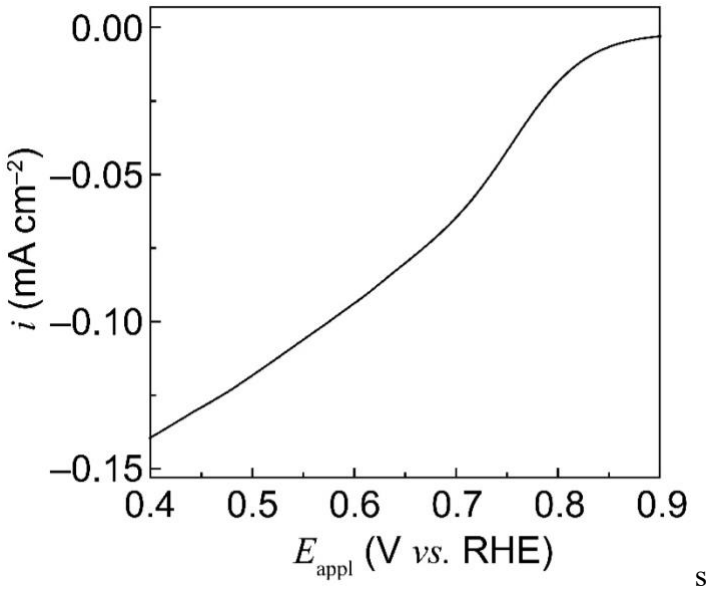


Figure S2.3. Morphological characterization of Au-coated wire array electrodes with k = (15, 4, 50) A The cross-sectional scanning electron microscopy (SEM) image depicting the side view of wire array with **k** = (15, 4, 50) **B** Energy-dispersive X-ray spectroscopy (EDS) spectra taken at different height along the Pt-coated wire array in **A**. A homogenous distribution of Au, In and Sn was observed along the prepared microwire array. Scale bar, 5 μm.



s

Figure S2.4. Linear scan voltammetry (LSV) measurement on Pt-coated wire array electrodes from 0.9 V *vs.* RHE to 0.4 V *vs.* RHE. The calculated Tafel slope was 110 mV/decade, and the estimated exchange current density was estimated to be 3×10^{-7}mA/cm^2.

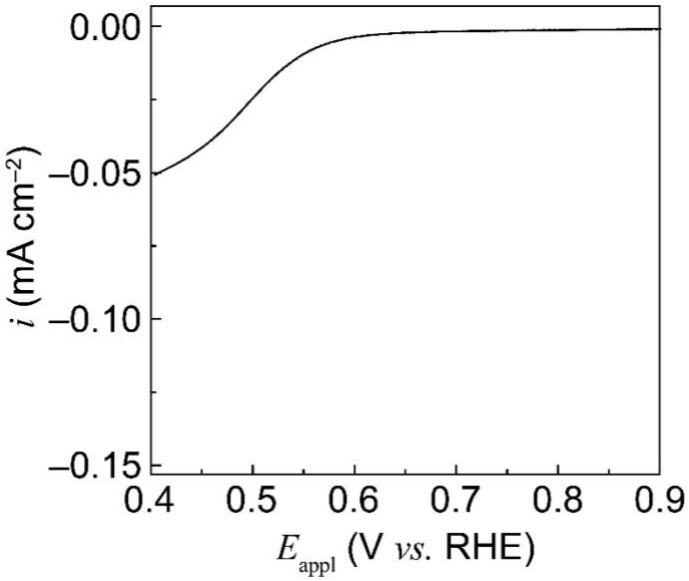


Figure S2.5. Linear scan voltammetry (LSV) measurement on Au-coated wire array electrodes from 0.9 V *vs.* RHE to 0.4 V *vs.* RHE. The fitted slope (176 mV/decade) supported electron transfer number and exchange current density of two-electron ORR and four-electron ORR on Au-coated wire array electrodes in simulation.

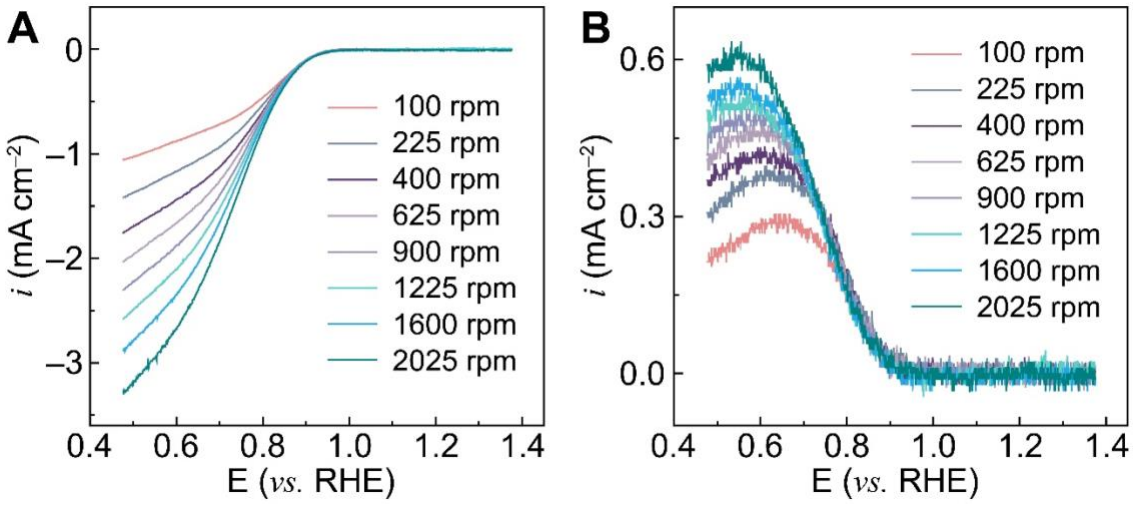


Figure S2.6. Rotating ring-disk electrode (RRDE) voltammetry on Au-coated working electrodes. A Voltammetry measurement on an Au-coated disk electrode. **B** Voltammetry measurement on the a Pt ring electrode. The electrochemical potential applied on the Pt ring electrode was 1.9 V *vs.* RHE during the measurement.

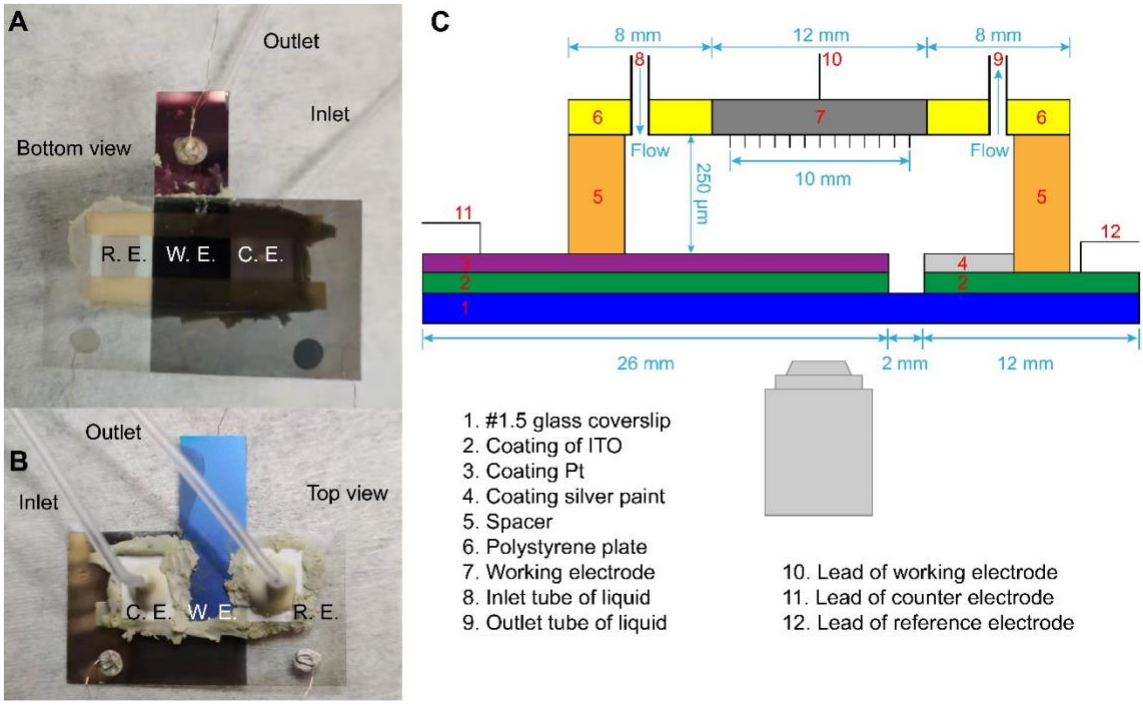


Figure S2.7. Photo of a fluidic device for a confocal microscope. A The bottom view of the fluidic device **B** The top view of the fluidic device **C** The device setup for confocal microscope. The objective lens is shown here in a setting of an inverted confocal laser scanning microscope. W. E., working electrode. C. E., counter electrode. R. E., reference electrode.

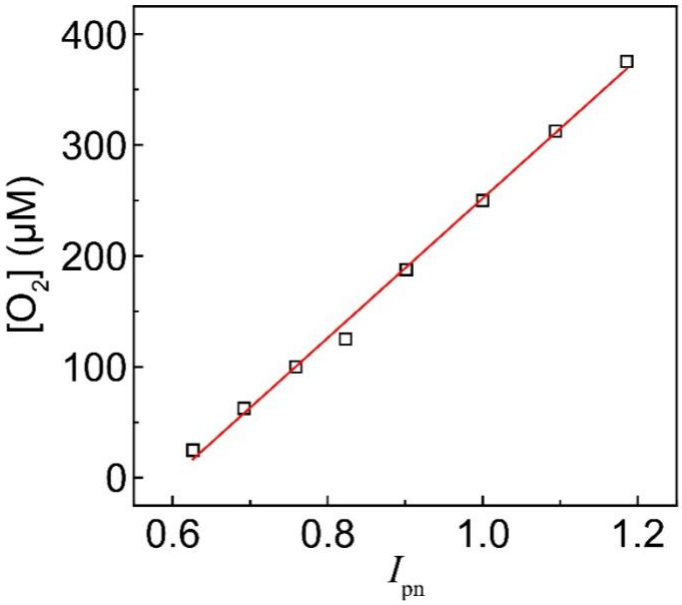


Figure S2.8. Plot of measured normalized phosphorescence intensity I_{pn} under various O_2 concentration. The I_{pn} of tris(1,10-phenanthroline)ruthenium(II), $Ru(Phen)_3^{2+}$ (Phen = 1,10-Phenanthroline) from 600 nm to 640nm (see "Materials and method" section) was measured under different O_2 concentration, which functioned as the standard curve for $[O_2]$ calibration.

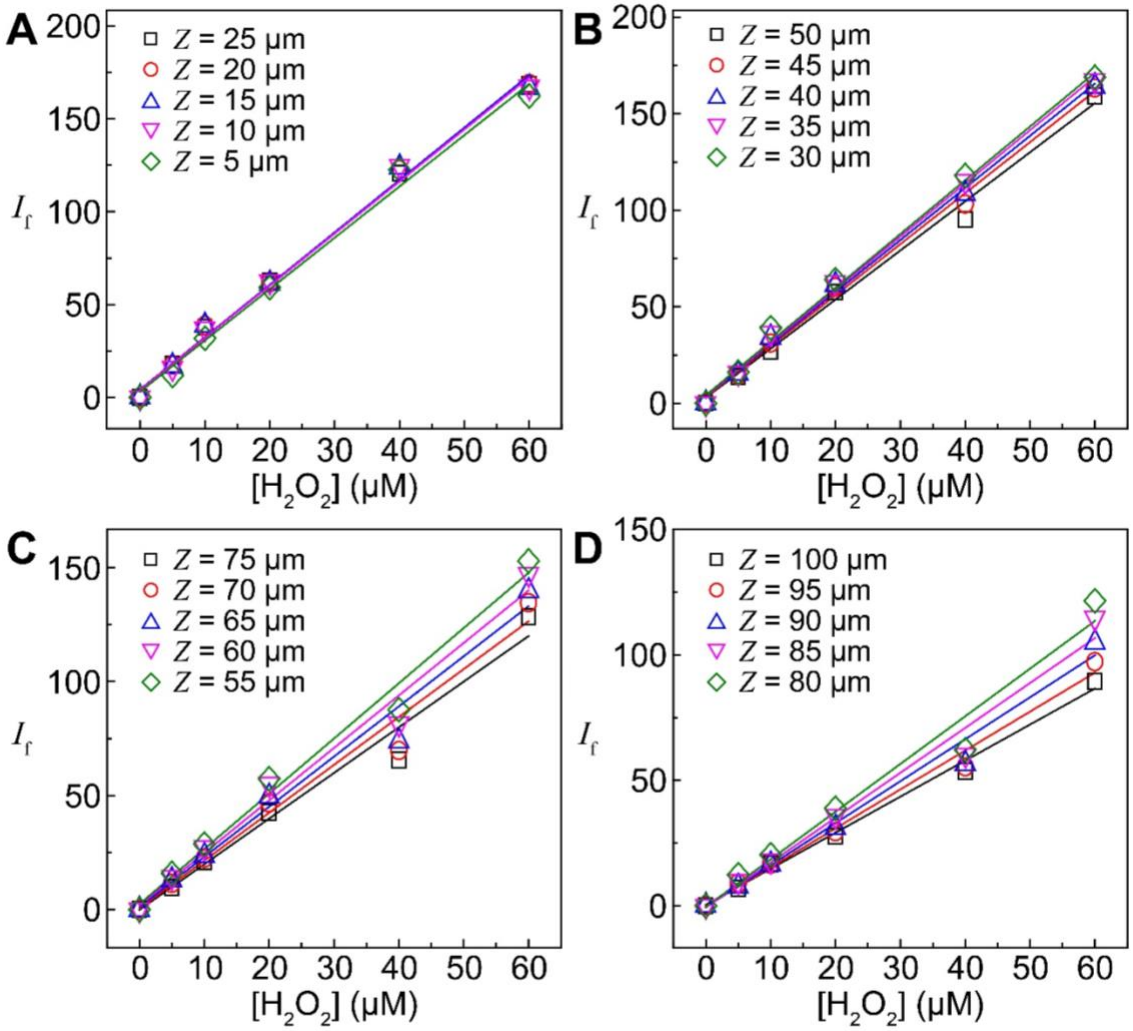


Figure S2.9. Plot of measured fluorescence intensity (I_f) under various H_2O_2 concentration on Au-coated wire array electrodes with morphology of k = (15, 4, 50). The local fluorescence intensity of resorufin from 590 nm to 650 nm (see "Materials and method" section) was measured under different H_2O_2 concentration. Z is the distance between measured region and the base of the wire array. The relationship between I_f and local H_2O_2 concentration ($[H_2O_2]$) was used for $[H_2O_2]$ calibration on Au-coated wire array electrodes. Morphological vector **k** = (P, D, L) presented the wire arrays' periodicity (P), diameter (D), and length (L), respectively, and unit is μm. **A** Calibration curves for region from Z = 5 μm to 25 μm. **B** Calibration curves for region from Z = 30 μm to 50 μm. **C** Calibration curves for region from Z = 55 μm to 75 μm. **D** Calibration curves for region from Z = 80 μm to 100 μm.

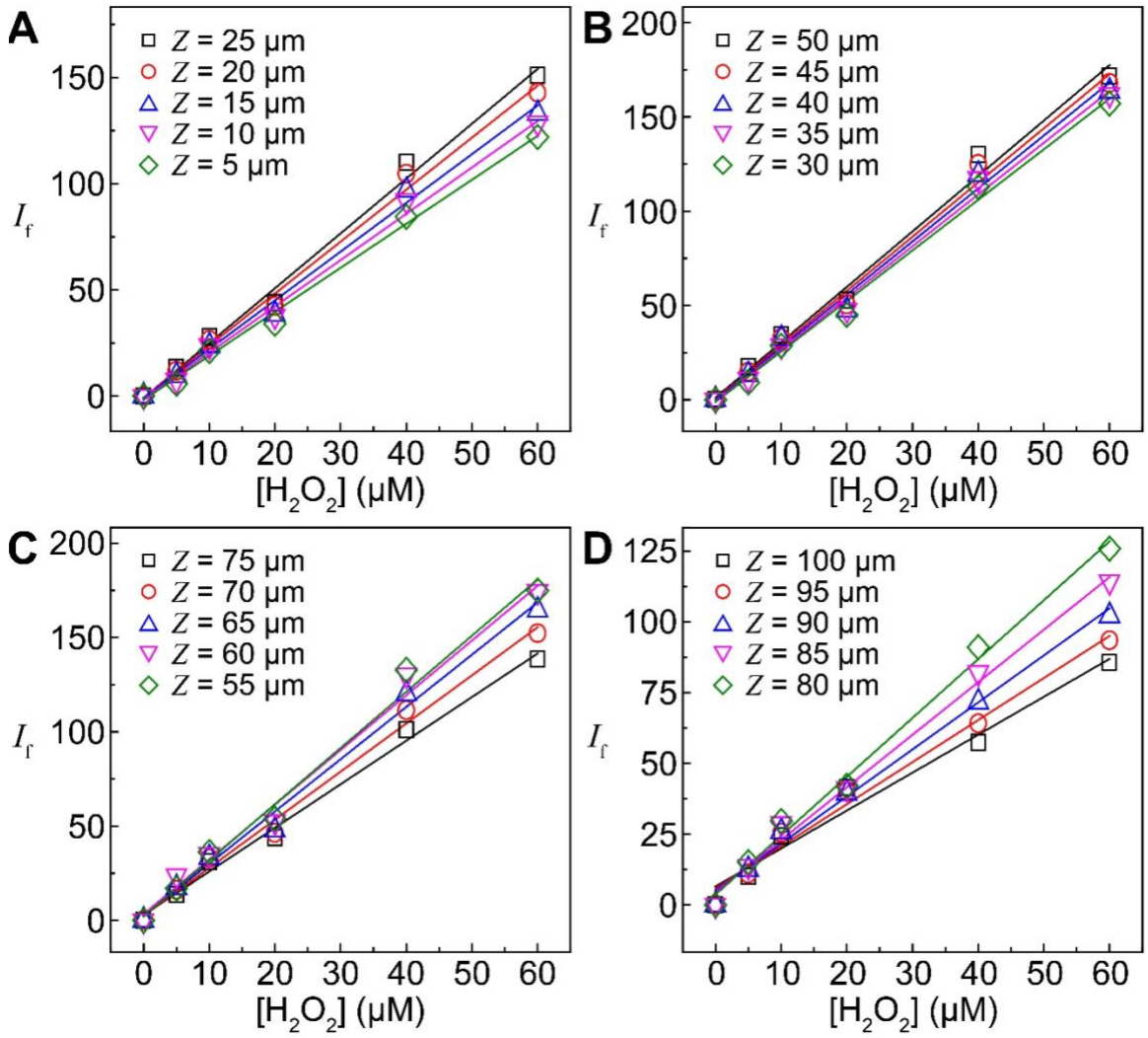


Figure S2.10. Plot of measured I_f under various H_2O_2 concentration on Au-coated wire array electrodes with morphology of k = (30, 3, 50). The local fluorescence intensity of resorufin from 590 nm to 650 nm (see "Materials and method" section) was measured under different H_2O_2 concentration. Z is the distance between measured region and the base of the wire array. The relationship between I_f and $[H_2O_2]$ was used for $[H_2O_2]$ calibration on Au-coated wire array electrodes. **A** Calibration curves for region from Z = 5 μm to 25 μm. **B** Calibration curves for region from Z = 30 μm to 50 μm. **C** Calibration curves for region from Z = 55 μm to 75 μm. **D** Calibration curves for region from Z = 80 μm to 100 μm.

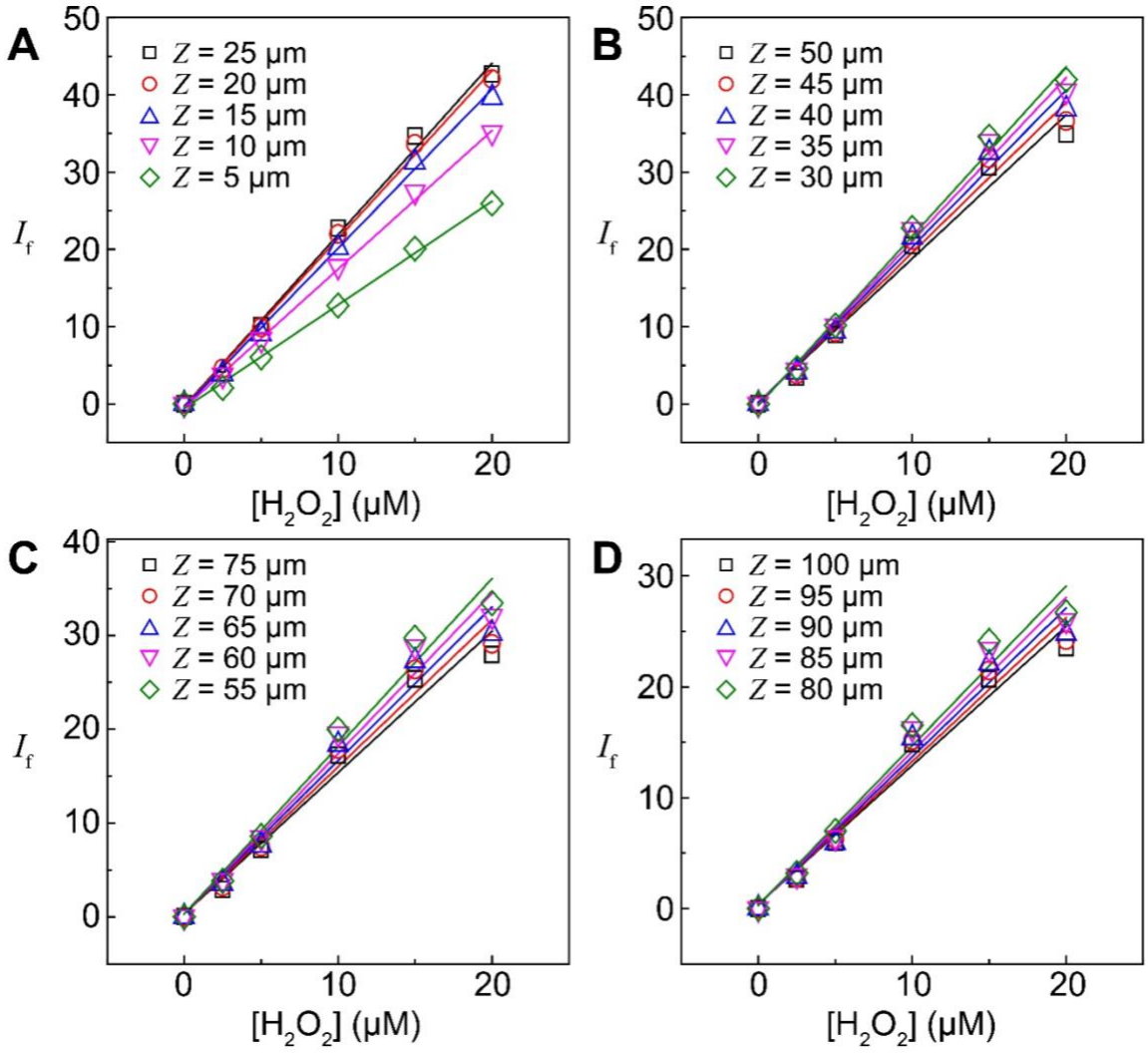


Figure S2.11. Plot of measured I_f under various H_2O_2 concentration on Au-coated wire array electrodes with morphology of k = (15, 4, 20). The local fluorescence intensity of resorufin from 590 nm to 650 nm (see "Materials and method" section) was measured under different H_2O_2 concentration. Z is the distance between measured region and the base of the wire array. The relationship between I_f and [H_2O_2] was used for [H_2O_2] calibration on Au-coated wire array electrodes. **A** Calibration curves for region from Z = 5 μm to 25 μm. **B** Calibration curves for region from Z = 30 μm to 50 μm. **C** Calibration curves for region from Z = 55 μm to 75 μm. **D** Calibration curves for region from Z = 80 μm to 100 μm.

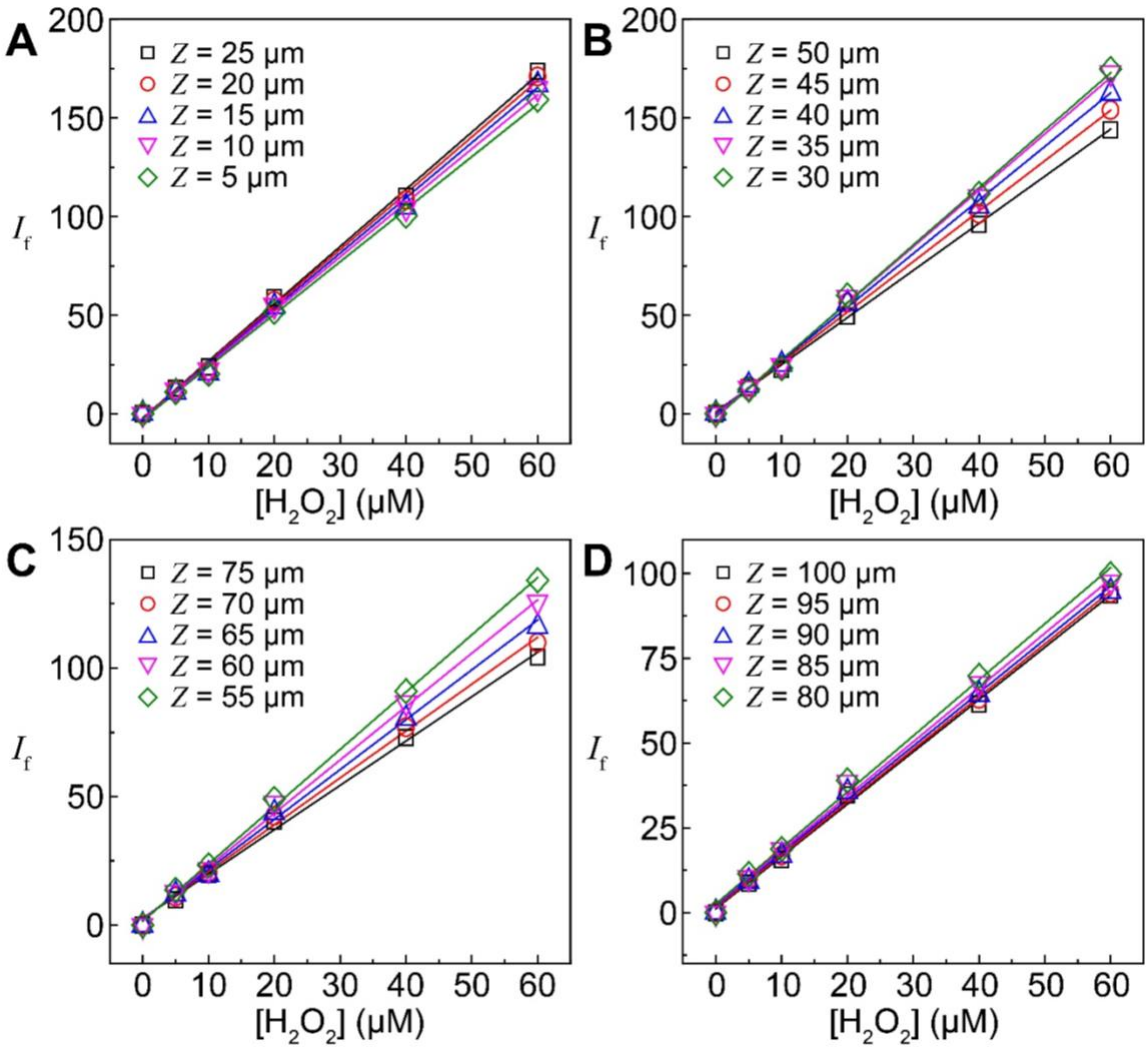


Figure S2.12. Plot of measured I_f under various H_2O_2 concentration on Au-coated wire array electrodes with morphology of k = (17, 3, 30). The local fluorescence intensity of resorufin from 590 nm to 650 nm (see "Materials and method" section) was measured under different H_2O_2 concentration. Z is the distance between measured region and the base of the wire array. The relationship between I_f and $[H_2O_2]$ was used for $[H_2O_2]$ calibration on Au-coated wire array electrodes. **A** Calibration curves for region from Z = 5 μm to 25 μm. **B** Calibration curves for region from Z = 30 μm to 50 μm. **C** Calibration curves for region from Z = 55 μm to 75 μm. **D** Calibration curves for region from Z = 80 μm to 100 μm.

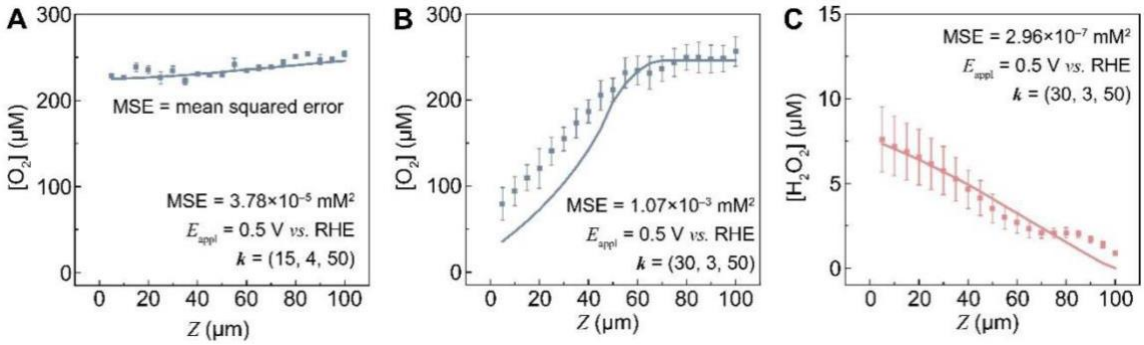


Figure S2.13. Simulated and experimental O_2 gradient and H_2O_2 gradient on Pt/Au-loaded wire array electrodes under E_{appl} = 0.5 V *vs.* RHE. A Simulated and experimental O_2 gradient on Au-loaded wire array electrodes with $\boldsymbol{k}$ = (15, 4, 50). **B** Simulated and experimental O_2 gradient on Pt-loaded wire array electrodes with $\boldsymbol{k}$ = (30, 3, 50). **C** Simulated and experimental H_2O_2 gradient on Au-loaded wire array electrodes with $\boldsymbol{k}$ = (30, 3, 50). All the dots are experimental data and all the lines are corresponding simulated gradients. Although O_2 gradients on Au-loaded wire array electrodes (**A**) are small perturbations (around 0.2 μM/μm), the simulation still achieved low mean squared error. MSE, mean squared error. Error bars represent standard deviations across multiple separate measurements in the device ($n \geq 3$).

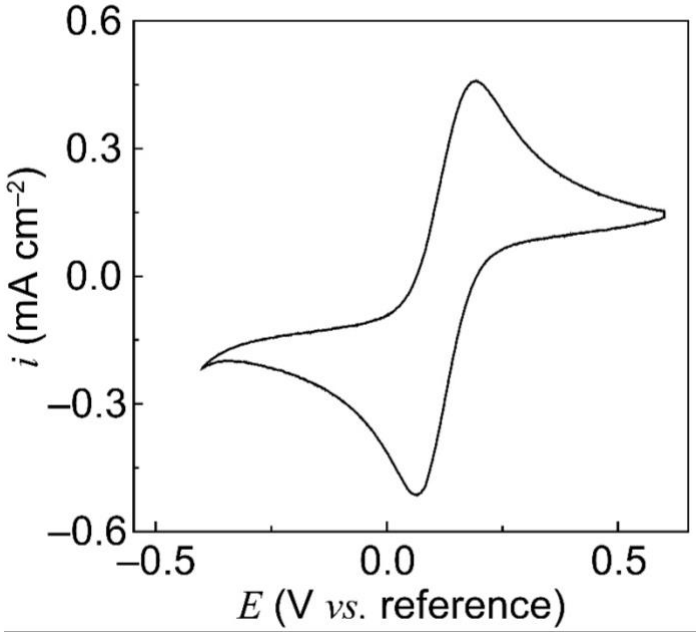


Figure S2.14. Cyclic voltammetry measurement in ZoBell's solution using Ag-pseudo reference electrode. Besides, a platinum wire and a glassy carbon electrode were used as the counter electrode and the working electrode respectively. The cyclic voltammetry measurement was conducted from 0.6 V *vs.* reference to –0.4 V *vs.* reference at a scan rate of 20 mV/s.

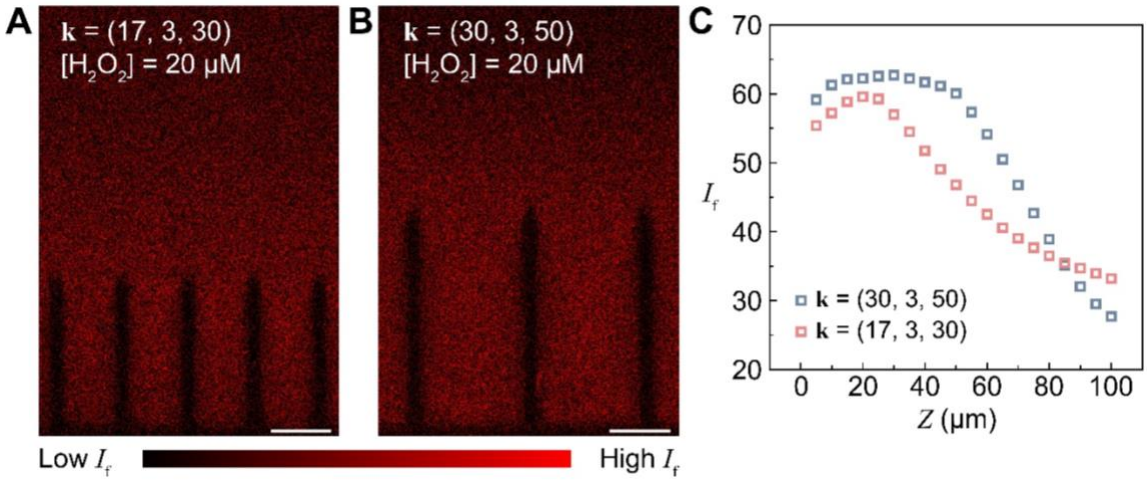


Figure S2.15. Fluorescence intensity I_f measurement under different morphologies. A Confocal image with **k** = (17, 3, 30) when [H_2O_2] = 20 μM **B** Confocal image with **k** = (30, 3, 50) when [H_2O_2] = 20 μM **C** I_f mapping comparison between 2 morphologies when [H_2O_2] = 20 μM, suggesting I_f is related to both morphology and location. Scale bar, 15 μm.

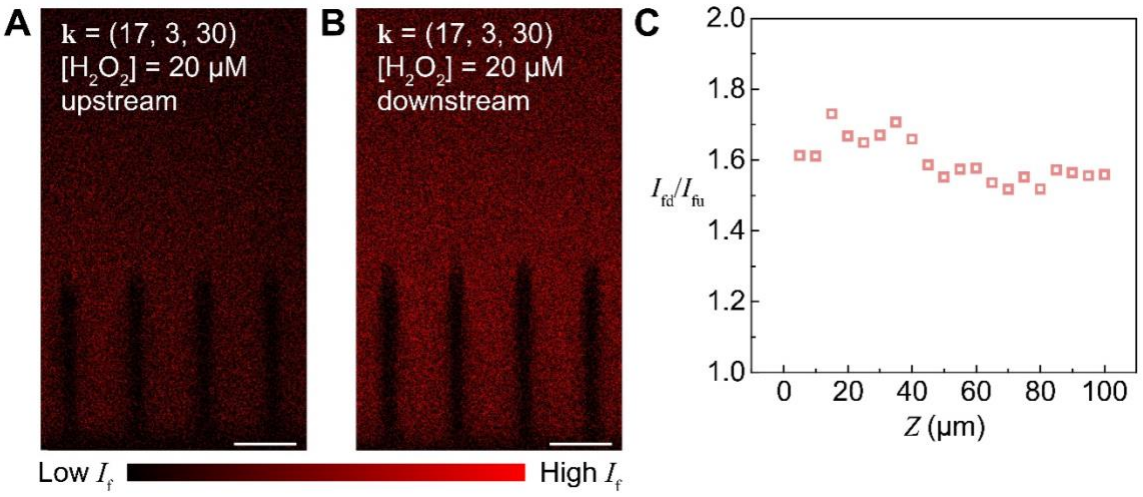


Figure S2.16. I_f difference between the upstream and downstream of the wire array electrode. **A** Confocal image with **k** = (17, 3, 30) when [H_2O_2] = 20 μM taken at the upstream of the wire array electrode **B** Confocal image with **k** = (17, 3, 30) when [H_2O_2] = 20 μM taken at the downstream of the wire array electrode **C** The ratio between fluorescence intensity at the downstream and fluorescence intensity at the upstream (I_{fd}/I_{fu}) at different location. The average ratio is around 1.6. The travel time from upstream to downstream was calculated as 0.84 s, suggesting I_f will increase by 1.9 times each second.

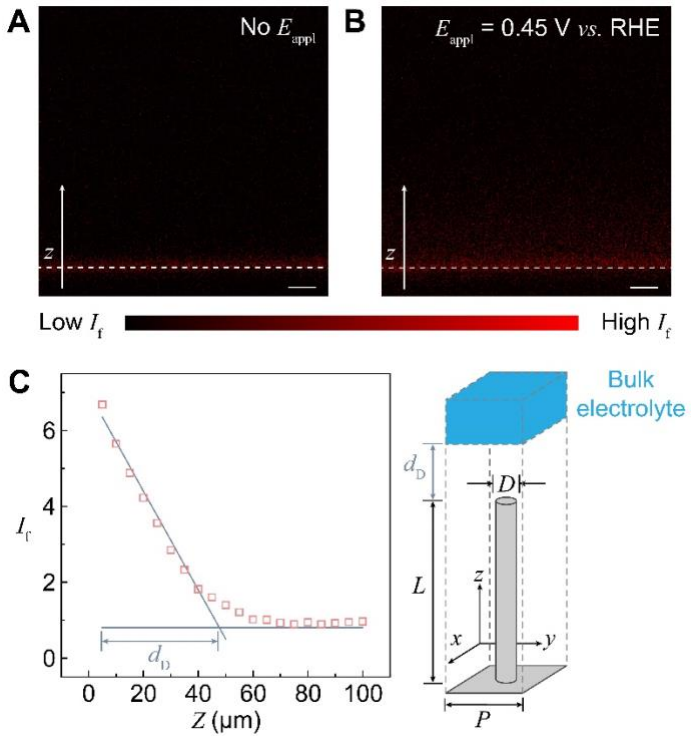


Figure S2.17. Fluorescence mapping on Au-coated planar electrode. A The fluorescence intensity (I_f) mapping on Au-coated planar electrode without E_{appl} **B** The I_f mapping on Au-coated planar electrode when E_{appl} = 0.45 V *vs.* RHE **C** Plotting of local I_f against the local distance from the base of the electrode (Z) on Au-coated planar electrode with E_{appl} = 0.45 V *vs.* RHE. The diffusion layer thickness, d_D, in FEM parameter table by the intersection of the two fitted red line. On Au-coated electrodes, d_D was 50 μm. Scale bar, 15 μm.

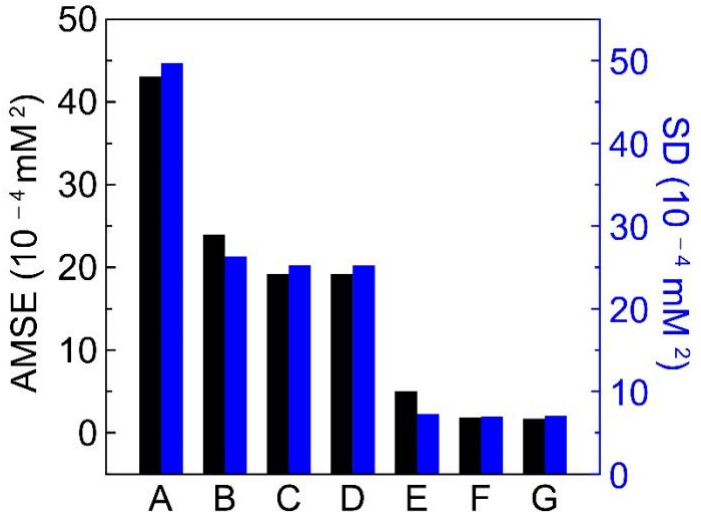


Figure S2.18. Machine learning model selection for O_2 gradient prediction on Pt-loaded wire array electrodes. The average mean square error (AMSE) and standard deviation (SD) of mean square error (MSE) in various machine learning approaches for O_2 gradient prediction on Pt-loaded wire array electrodes (A is Random Forest Regressor, B is Support Vector Regression, C is Bayesian Ridge Regression, D is Stochastic Gradient Descent, E is Adaboost Regressor, F is K-Nearest Neighbors Regressor, G is Multiple-layer Perceptron Neural Networks).

Chapter 3. Electrochemical control for extracellular pH microenvironment with high spatiotemporal resolutions

This chapter is a version of Wang, J.; Xie, Y.; Zou, H.; Chen, Y.; Liu, C. "Electrochemical control with high spatiotemporal resolutions for extracellular pH microenvironment." *Submitted* **2024**.

Abstract

The local pH values hence the pH microenvironment surrounding an organism critically affects its metabolism and physiology in both prokaryotes and eukaryotes. Despite the ubiquitous spatiotemporal heterogeneity of local pH conditions in biology, a biocompatible method that spatiotemporally programs pH microenvironment remains elusive. Here we report an electrochemical approach that spatiotemporally controls pH microenvironments for potential microbial applications. Quinone-based redox couple undergoes electrochemical proton-coupled electron transfer (PCET) that releases or consumes protons hence changes local pH. We designed a biocompatible hydroquinone/quinone redox couple that has minimal interference with bacterial aerobic respiration thanks to its hydrophilic nature and the specially targeted redox potential. Deploying such uniquely designed redox couple with interdigitated electrodes in a microfluidic device leads to an electrochemical control of pH microenvironment with fast temporal modulation (~10^1 s) and high spatial resolution (~10^0 μm) suitable for biological applications. The concept of deploying biocompatible electrochemistry offers a new venue towards perturbing biological microenvironments at cellular if not subcellular level.

Introduction

The extracellular pH environment surrounding an organism that measures the local availability of proton is essential for every aspect of biological physiology and metabolism[1-3]. Oxidative phosphorylation, the most important route of ATP generation in aerobic respiration for most of organisms on this planet[4,5], relies on a suitable proton motive force and local proton availability for transmembrane proton translocation[6]. Yet the biochemical metabolism itself also effects the local extracellular pH hence the pH microenvironments in the vicinity of the organisms. The Warburg effect in cancerous cells leads to locally acidic conditions in tumor tissues[7]. Fermentative respiration commonly secrets organic acid that also changes the local pH, whose values typically ranges between 5 and 7 (Fig. 3.1a),[8-10] especially in the extracellular space of biofilms[11-13]. From the perspective of bioenergetics, the transfers of proton and electron hence energy are so ubiquitously coupled that there are hardly any biological phenomena completely independent of local pH conditions. The close interplay between organisms and their microenvironments leads to ubiquitous spatiotemporal heterogeneities of pH microenvironments in nature. Tools that characterize and/or perturb such biological pH microenvironments are critical for our advanced understanding of various prokaryotic and eukaryotic systems.

The capability of spatiotemporally perturbing pH microenvironments for biological applications remains limited. Extensive efforts have been devoted towards the characterization of biological pH microenvironments particularly via fluorescent microscopy[11,14-17]. Yet there are only limited means for researchers to realize spatiotemporal perturbation towards extracellular pH at micrometer-scale level, particularly under experimental conditions commensurate with optical microscopy. Microfluidic systems create spatial pH gradients by mixing laminar fluidic flows of different pH[18-21], but the spatial resolution is limited to about 10^2 μm[18-21] and takes at least several

minutes (~10^2 seconds) for a temporal perturbation to be stably achieved[20]. Such a spatiotemporal resolution is unsatisfying, especially given the fledging interests in physiology and metabolism under single-cell if not sub-cellular levels[22-24]. It is necessary to develop tools that perturb pH extracellular microenvironments faster with a smaller spatial resolution.

We hypothesize that biocompatible electrochemistry of proton-coupled electron transfer (PCET) in the extracellular space offers a new venue of programmable pH microenvironments. Electrochemical PCET reaction[25,26] consumes or produces proton in electrode's vicinity, which will lead to a diffusion-based microscopic pH gradients in weakly buffered aqueous solutions near neutral pH (Fig. 3.1b). As we recently demonstrated for the microenvironments of O_2 and reactive oxygen species[27,28], the spatial profile of chemical microenvironments can be programmed with high spatial resolution (10^0 μm), potentially via inverse design based on machine-learning[28], by fine-tuning electrodes' morphology and spatial arrangement. Meanwhile, not only the magnitude of applied electrochemical potential E_{appl} provides one more degree of freedom for concentration's spatial profile, the temporal sequence of E_{appl} controls the microenvironments in a time-dependent manner with a time resolution of seconds if not tens of seconds (10^0~10^1 seconds)[28-30]. Therefore, in a microfluidic device equipped with pre-designed electrochemical configuration such as interdigitated electrodes (IDEs), a programmable electrochemical PCET process is proposed to reinforce our limited capability of controlling extracellular pH microenvironments with spatiotemporal resolutions at single-cell if not sub-cellular levels (Fig. 3.1c). However, such a concept has yet been tested experimentally despite its attractiveness and the apparent paucity of tools for extracellular pH perturbation.

One major challenge in fulfilling such a tantalizing concept is the biocompatibility and orthogonality of the pH-controlling electrochemical PCET process. As we aim to

electrochemically perturb only the extracellular pH microenvironments, the electrochemical PECT reaction ought be not only compatible with the biological moieties but also induce no undesired cellular responses, particularly under aerobic/microaerobic conditions when the cellular bioenergetic is sensitive to the extracellular pH hence the proton motive force[5,6]. Our strategy to address this challenge is to design an electrochemical PCET reaction with two unique properties: First, we will deploy highly hydrophilic molecules of PCET reaction that have minimal physical interactions with cellular structures and do not penetrate through the cellular membrane; second, the redox species are chosen so that the corresponding redox potential does not interfere much if not any either with the dissolved O_2 or with the cellular electron transport chain (ETC)[31] (Fig. 3.1d), in order to minimize the potential formation of reactive oxygen species (ROS) and the potential disruption of membrane-bound oxidative phosphorylation. We surmise such a design strategy will minimize the interaction between the redox molecule and organisms, hence reduce the chances of potential alternation of cellular metabolism and physiology. In this context, this work reports our progresses towards biocompatible PCET reaction for the extracellular modulation of extracellular pH microenvironments.

Here we report the design of a hydroquinone/quinone PCET redox couple, proposed to be compatible and orthogonal with biological moieties, that serves to electrochemically program pH microenvironments spatiotemporally. Thanks to its hydrophilic nature and suitable redox potential, 2,5-dihydroxybenzene sulfonate potassium (DHBS) as the hydroquinone component is found to have minimal interference with the growth of opportunistic pathogen *Pseudomonas aeruginosa*[32,33] and allows for electrochemical modulation of local pH via the two-electron PCET process. Tested in an IDE-equipped microfluidic channel, we demonstrate biocompatible electrochemical programming of spatiotemporal pH profiles in solution with spatial and temporal

resolutions (about 10^0 μm and 10^1 s) unachieved in other pH-controlling microfluidic devices. Such results showcase the feasibility of controlling pH concentration profiles with biocompatible PCET reactions, creating opportunities of future research to perturb extracellular pH microenvironments at single-cell if not subcellular levels.

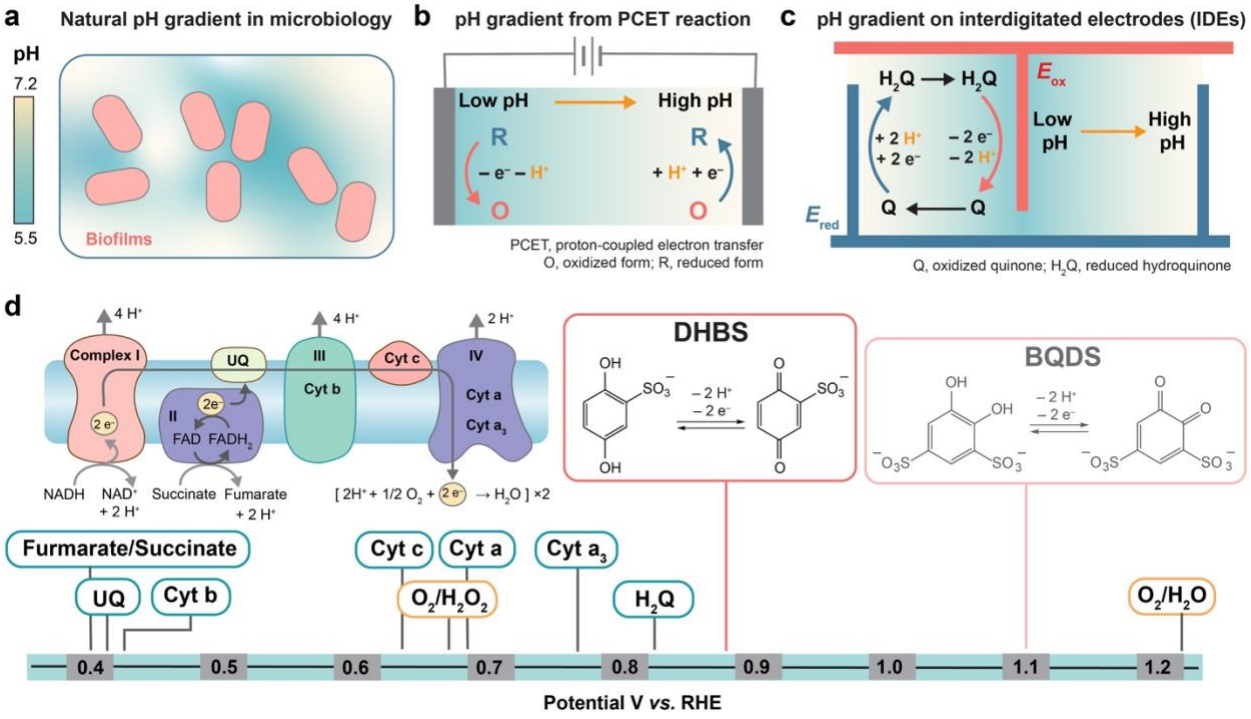


Figure 3.1. The design of electrochemical PCET reaction for extracellular pH modulation. a, the spatial pH profiles observable in bacterial systems, as an example of the ubiquitous pH heterogeneity in biology. **b**, The concept of generating pH gradients via electrochemical proton-couple electron transfer (PCET) reactions. **c**, Schematic of electrochemically generated pH gradient via PCET-based redox couple of quinone (Q) and hydroquinone (H_2Q), facilitated by interdigitated electrodes (IDEs) potentially in a microfluidic device. E_{ox} and E_{red}, the electrochemical potentials on the oxidizing and reducing electrodes, respectively. **d**, The Latimer diagram at pH = 7.0 for the design of hydroquinone/quinone derivatives given the redox potentials (E^o) in O_2 chemistry and the individual components of membrane-bound electron transport chain

(ETC). This work tested two candidate hydroquinone derivatives, 2,5-dihydroxybenzene sulfonate potassium (DHBS) and 4,5-dihydroxybenzene-1,3-disulfonic acid (BQDS). At pH = 7.0, E_{RHE} (V) *vs.* RHE = E_{SHE} (V) *vs.* SHE − 0.413 V. RHE, reversible hydrogen electrode; SHE, standard hydrogen electrode.

Results and Discussion

Design considerations for biocompatible PCET reaction based on quinone derivatives

Three criteria were implemented when designing the PCET process for electrochemical pH perturbation in the extracellular space. First, because an electrochemical PCET process relies on the stoichiometric consumption or generation of protons to change local pH, the PCET redox couples ought to have high solubilities that at least are similar to the buffer concentration in the biological medium (usually 10^0 ~ 10^1 mM). This led us to consider the redox couples based on synthetic hydroquinone/quinone chemistry, which undergo bidirectional PCET processes in water[34,35] and are known to have high aqueous solubilities thanks to the surging interests in aqueous redox flow batteries[36-38]. Second, as we propose to entail minimal interference between the redox couples and organisms, hydroquinone/quinone derivatives with highly negatively charged functional groups (e.g., sulfonate group) were favored. Not only will those negatively charged hydroquinone/quinone derivatives entail electrostatic repulsive interactions from the negatively charged cellular surface[39-41], but these hydrophilic molecules are also considered incapable of permeating through the cellular membranes for any alternation of metabolisms in the cytosol.

The third criterion for the PCET redox couple is a suitable redox potential that minimizes unwarranted side reactions with dissolved O_2 and the membrane-bound ETC in aerobic respiration (Fig. 3.1d). Hydroquinone, the two-electron, two-proton reduction product from quinone, is known

to reduce O_2 into H_2O_2[42], a potent ROS species, when thermodynamically its redox potential E^o is more negative than the redox potential of O_2 reduction H_2O_2 ($E^o_{O2/H2O2}$ in Fig. 1d)[43]. Therefore, the E^o of hydroquinone/quinone redox that suits our design should be more positive than $E^o_{O2/H2O2}$. Meanwhile, E^o should be more negative than the redox potential of water oxidation reaction ($E^o_{O2/H2O}$ in Fig. 1d), in order to avoid water oxidation from the oxidized quinone species. Last, the redox's interaction with the membrane-bound ETC should be mitigated by a judicious selection of hydroquinone/quinone's E^o. We conjecture that there will be minimal interaction if the E^o is more positive than that redox species in Complex IV of ETC, the cytochrome a and a_3 (cyt a and cyt a_3, respectively, in Fig. 1d)[31], when the electron hence energy flux in the ETC will not be altered had the hydroquinone/quinone redox underwent electron transfers with the membrane bound ETC. Overall, although the concept of electrochemical pH modulation sounds straightforward with seemingly a large amount of candidate hydroquinone/quinone derivatives, the multiple criteria from various considerations indeed render a limited range of options for the PECT redox couple.

Under the aforementioned criteria, two hydroquinone derivatives, 5-dihydroxybenzene sulfonate potassium (DHBS) and 4,5-dihydroxybenzene-1,3-disulfonic acid (BQDS) (Fig. 3.1d), both negatively charged at almost all pH ranges in aqueous solution, were chosen as the hydroquinone components for the candidate redox couple. Both molecules are commercially available and have been developed for the application of aqueous redox flow batteries thanks to their stability and high aqueous solubility (up to 0.7 and 0.3 M)[38]. The negative charge and the electron-withdrawing nature of the sulfonic group are proposed to yield minimized cellular interactions and suitable redox potentials of 0.9 and 1.1 V *vs.* Reversible Hydrogen Electrode (RHE) at pH = 7.0 for DHBS and BQDS, respectively (Fig. 3.1d)[36,38]. As will be shown below, both DHBS and BQDS have

been tested while DHBS was found more appropriate for electrochemically controlled pH microenvironments.

Electrochemical characterizations for two hydroquinone/quinone redox couples

Experiments of cyclic voltammetry on glassy carbon, platinum (Pt) and gold (Au) electrodes (see Methods) were conducted in 1× phosphate-buffered saline (PBS) solution (pH = 7.2, medium 1.1 in Table S3.1) to examine the electrochemical PCET processes for 5 mM of BQDS (Fig. 3.2a) and DHBS (Fig. 3.2b). Bidirectional PCET-based reduction and oxidation were observed for both quinone derivatives on all electrode materials, while kinetically faster for DHBS based on the smaller potential differences between the better-defined cathodic and anodic peaks. Estimated based on mid-point potentials, the measured E^{o} of BQDS and DHBS are 0.9 and 1.1 V *vs*. RHE, respectively, consistent with literature values of 0.88 and 1.10 V *vs.* RHE reported in 0.5 M phosphate buffer[36,38].

Plotting the current densities i_p of anodic and cathodic peaks when available against the square roots of scan rates ($v^{1/2}$) in voltammetry leads to linear relationships for all electrode materials for both BQDS (Fig. 3.2c) and DHBS (Fig. 3.2d). This indicates diffusion-based redox behavior and minimal adsorption thanks to the highly negatively charged nature of those hydroquinone/quinone derivatives. The observation that the hydrophobic glassy carbon, analogous to the lipid bilayer of cellular membranes, does not induce any observable surface adsorption in Fig. 3.2c and 3.2d is supportive of our design that a hydrophilic, negatively charged quinone will incur muted interaction with biological moieties in solution.

Experiments of rotating disk electrode (RDE) in Au electrode (Fig. 3.2e, 3.2f and Supplementary Fig. S3.1; see Methods, medium 1.2 in Supplementary Table S3.1) were conducted for both BQDS and DHBS in order to extract the number of electrons transferred during the redox phenomena in

Fig. 3.2a and 3.2b. At 1.5 V *vs.* RHE, the inverse of oxidative current ($1/I$) for the reduced BQDS is plotted against the inverse of square root of angular rotation rate ($1/\omega^{1/2}$) (Fig. 2e) for the analysis based on the Koutecký-Levich equation[44,45]. Based on a diffusion coefficient of 2.7×10^{-6} cm^2/s,[45,46] the number of electron transfer (n) is calculated as 1.06. In contrast, the same analysis for DHBS at 1.45 V *vs.* RHE (Fig. 3.2f) yields n = 2.10 based on a diffusion coefficient of 4.28×10^{-6} cm^2/s[47]. These results show that BQDS at neutral pH undergoes a one-electron, one-proton electrochemical process with semiquinone radical as the oxidized species, while DHBS at the same condition undergoes a targeted two-electron, two-proton one between the hydroquinone and quinone redox species[34]. Such results are consistent with the faster PCET kinetics for DHBS observed in cyclic voltammetry (Fig. 3.1a and 3.2b). Compared to BQDS's semiquinone radical as the oxidized counterpart in the PCET process, the electrochemical hydroquinone/quinone interconversion of DHBS are considered less prone to side reactions.

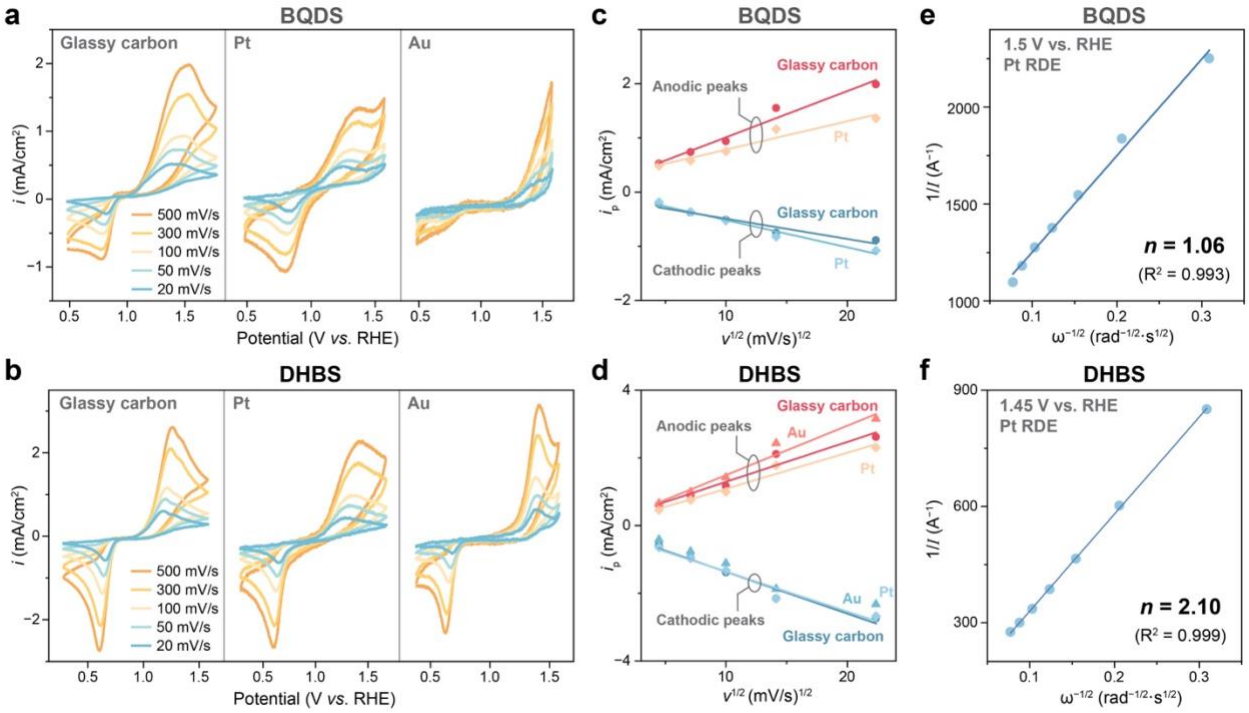


Figure 3.2. Electrochemical characterizations of BQDS and DHBS. a and **b**, Cyclic voltammograms for BQDS (**a**) and DHBS (**b**) at 1× phosphate-buffered saline solution (PBS, pH = 7.2, medium 1.1 in Table S1) with glassy carbon, platinum (Pt), and gold (Au) working electrodes. **c** and **d**, the current densities of cyclic voltammograms for the anodic and cathodic peaks (i_p) against the square root of scan rate v ($v^{1/2}$) for BQDS (**c**) and DHBS (**d**). **e** and **f**, the inverse of oxidative current ($1/I$) on Au rotating disk electrode (RDE) against the inverse of square root of angular rotation rate ($\omega^{-1/2}$) for BQDS (**e**, at 1.5 V *vs.* RHE) and DHBS (**f**, at 1.45 V *vs.* RHE) in 10 mM phosphate buffer (medium 1.2 in Table S1) The electron transfer number n determined from the Koutecký-Levich equation are 1.06 and 2.10 for BQDS and DHBS, respectively. All data were *iR* corrected in N_2 with AgCl/Ag (1 M KCl) reference and Au mesh counter.

Biocompatibility assay for two hydroquinone/quinone redox couples

Biocompatibility tests were conducted by observing the effects of either BQDS or DHBS towards the aerobic growth of *Pseudomonas aeruginosa* (see Methods), a gram-negative, opportunistic bacterial pathogen[32] demonstrating extensive pH heterogeneities (pH $\in$ [5.5, 7.2]) within its biofilms[16,48]. Two different strains of *P. aeruginosa*, moderately virulent PAO1[33,49] and hyper-virulent PA14[33], were both tested with biological triplicates (n = 3). In Fig. 3a, the optical density at 600 nm (OD_{600}), a surrogate of cell density, is plotted as function of time for *P. aeruginosa* PAO1 in phosphate-buffered growth medium (pH = 7.2, medium 2.1 in Table S3.2) in the absence of any organic substrate (yellow), 20 mM BQDS (dark blue), 20 mM DHBS (light blue), or 30 mM succinate (red). Since appreciable bacterial growth was only observed with the addition of succinate, neither BQDS nor DHBS serves as organic substrate to support cellular growth. There is no significant impact on bacterial growth when the phosphate buffer concentration of the

medium is within the range of 10 mM to 43 mM (Fig. 3.3b), suggesting that the buffer capability of the bacterial culture solution may not be critical within a certain concentration range.

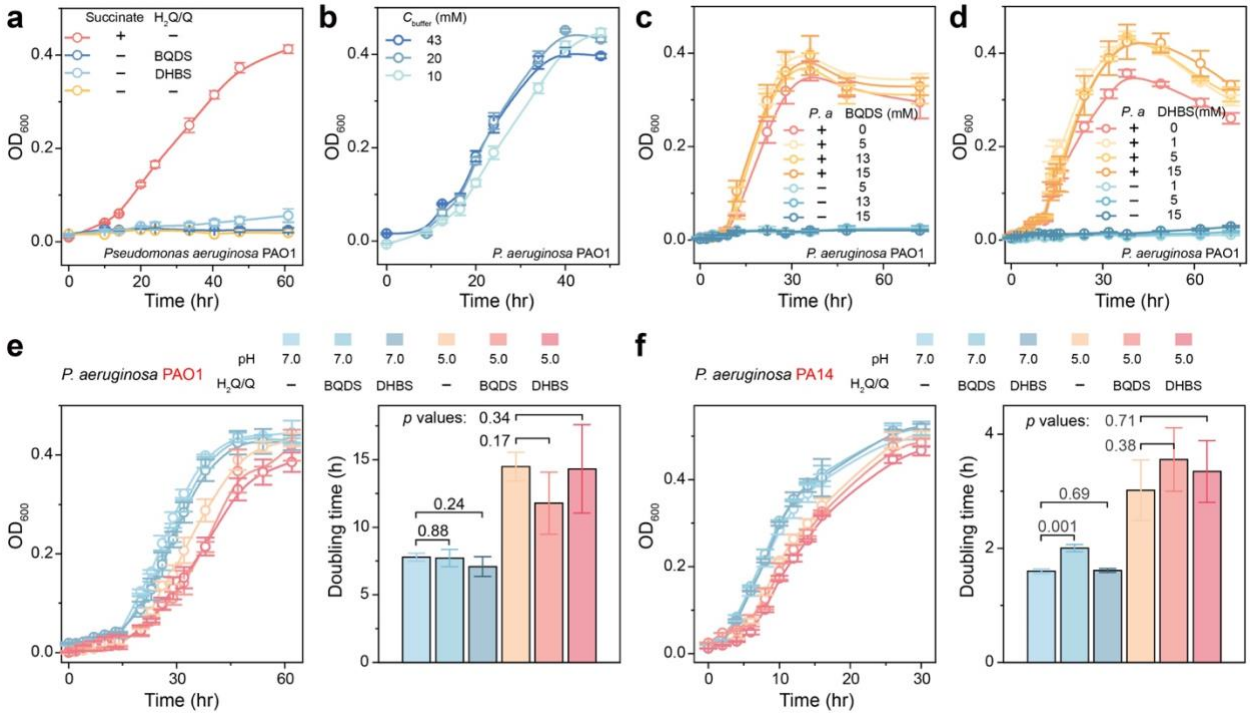


Figure 3.3. Aerobic growth of *Pseudomonas aeruginosa* with the presence of BQDS and DHBS. a, Aerobic growth curves for *P. aeruginosa* PAO1 in phosphate-buffered growth medium (medium 2.1 in Table S S3.2) with the addition of succinate (red), BQDS (dark blue), DHBS (light blue), and no addition of any organic sources (yellow). OD_{600}, optical density at 600 nm. **b**, Aerobic growth curves for *P. aeruginosa* PAO1 under different concentration of phosphate buffer (C_{buffer}) adapted from the growth medium (medium 2.1 in Table S S3.2). **c** and **d**, Aerobic growth curves for *P. aeruginosa* PAO1 under different concentrations BQDS (**c**) and DHBS (**d**) along with the abiotic controls (medium 2.2 in Table S S3.2). **e** and **f**, Aerobic growth curves and the corresponding doubling times in two different pH conditions (pH = 5.0 and 7.0) for *P. aeruginosa* strains PAO1 (**e**) and PA14 (**F**) in growth mediums buffered by phosphate and 3-(N-morpholino) propanesulfonic acid (MOPS) (Medium 2.2 in Table S S3.2 and medium 3.1 in Table S S3.3),

respectively. Biological triplicates (n = 3). Error bars represent standard deviations. p values calculated via two-sample unequal variance t-test.

The addition of BQDS or DHBS up to 15 mM did not significantly hinder the growth of *P. aeruginosa* PAO1 (Fig. 3.3c and 3.3d, respectively), at 40-mM succinate growth medium with 10 mM phosphate buffer (pH = 7.2, medium 2.2 in Supplementary Table S3.2). Indeed, in the case of DHBS, the minimum inhibition concentration, defined as the lowest concentration of a chemical that will inhibit the visible growth of an organism[50], was estimated to be between 128 to 256 mM based on bacterial growth in 96-well plate (Supplementary Fig. S3.2, see Methods, medium 2.2 in Supplementary Table S3.2); the half-maximal inhibitory concentration (IC_{50}), defined as the concentration of inhibitor necessary to halve the reaction rate observed under specified assay condition[51], was estimated to be about 100 mM based on spot assay on the agar plate (Supplementary Fig. S3.3, see Methods, medium 2.2 in Supplementary Table S3.2). These results suggest that bacterial growth hence cellular metabolism is not significantly perturb by the added hydroquinones, particularly DHBS, until the hydroquinone's concentration reaches about 100 mM.

As the hydroquinone/quinone redox is designed to alter the extracellular pH microenvironments, the biocompatibilities of BQDS and DHBS were further tested at different pH conditions by evaluating the doubling times based on the growth curves of PAO1 and PA14 strains (see Methods, medium 2.2 in Supplementary Table S3.2 and medium 3.1 in Supplementary Table S3.3, respectively). As the extracellular pH for biofilms of *P. aeruginosa* typically ranges roughly between 5 to 7,[10,48] the bacterial doubling times at pH = 5.0 and 7.0 were both investigated. For PAO1 strain, the growth curves and doubling times with the addition of 15 mM BQDS or 15 mM DHBS were compared with the controls of bare succinate growth medium (Fig. 3.3e; medium 2.2 in Supplementary Table S3.2). There are no statistically significant differences (p value > 0.05,

two-sample unequal variance t-test) in terms of doubling time with the addition of BQDS or DHBS at both conditions of pH = 5.0 and 7.0, although in general *P. aeruginosa* grows slower at the suboptimal condition of pH = 5.0. Similar experiments were conducted for PA14 strain in the growth medium of 10 mM 3-(N-morpholino)propanesulfonic acid (MOPS) buffer (see Methods, medium 3.1 in Supplementary Table S3) (Fig. 3.3f). For the PA14 strain, there are no statistically significant differences (p value > 0.05, two-sample unequal variance t-test) in terms of doubling time with the addition of BQDS or DHBS at both conditions of pH = 5.0 and 7.0, notwithstanding the condition of pH = 5.0 with the addition of BQDS (p value = 0.001). This indicates that in acidic medium bacterial growth was inhibited by BQDS, potentially owning to its one-electron PCET process that yields reactive semiquinone radicals. Nonetheless, overall there is minimal interference from the hydroquinone/quinone species, particularly for DHBS, towards the aerobic growth of *P. aeruginosa* at different pH conditions, reinforcing our hypothesis that a highly negatively charged hydroquinone/quinone redox couple with suitable electrode potential will be orthogonal towards cellular metabolism.

The experimental design for electrochemically controlled pH microenvironments

We chose to deploy DHBS-based redox couple for the experimental demonstration of electrochemical pH perturbation. Our electrochemical characterizations indicate that at neutral pH, DHBS undergoes the presumed two-electron, two-proton PCET process between the hydroquinone and quinone forms with relatively fast reaction rates, despite the challenging kinetics for stepwise PCET at neutral pH based on the kinetic model developed by E. Laviron[52]. Moreover, while BQDS and DHBS are both appreciably noninterfering towards the aerobic growth of *P. aeruginosa*, our evaluation of doubling times suggests that DHBS does not hinders bacterial growth even at suboptimal pH = 5.0, a condition when BQDS may be less innocent. The BQDS's

noninnocence towards bacterial growth is putatively due to the generated semiquinone from an O_2-driven one-electron, one-proton oxidation, whose radical nature poses BQDS a less benign redox couple for biological systems.

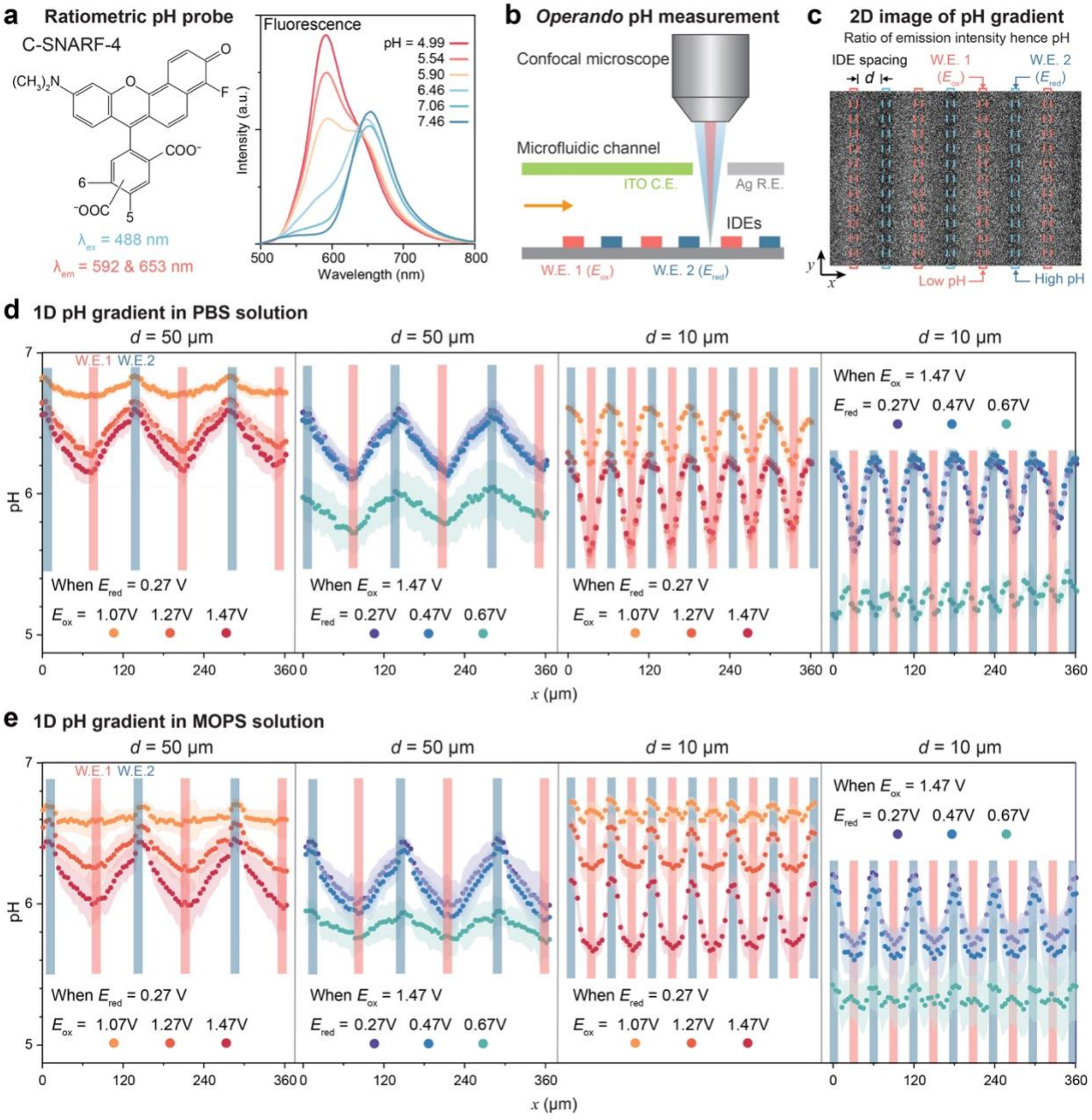


Figure 3.4. Steady-state pH gradient generated by DHBS-based electrochemistry in biological mediums. a and **b**, pH-sensing ratiometric fluorescent probe seminaphthorhodafluor-

4F 5-(and-6) carboxylic acid (C-SNARF-4) (**a**) was deployed for the quantification of pH gradient in a microfluidic channel equipped with Au IDEs (**b**), whose two working electrodes (W.E. 1 and W.E. 2) electrochemically oxidizes and reduces the DHBS redox couple with potential E_{ox} and E_{red}, respectively. Indium-tin oxide (ITO), counter electrode (C.E.); Ag-coated ITO, pseudo-reference electrode (R.E.). λ_{ex}, excitation wavelength; λ_{em}, emission wavelength. **c**, The two-dimensional (2D) mapping about the ratio of fluorescent emissions (653 *vs.* 592 nm), 5 μm above the electrode surface, overlayed with the locations of W.E. 1 and W.E 2. *d*, the distance between W.E. 1 and W.E 2. The directions normal and parallel to the finger electrodes are defined as the *x* and *y* axes, respectively. **c** and **e**, one-dimensional (1D) pH gradients against the *x* coordinate in growth mediums buffered by phosphate (**d**, medium 2.2 in Supplementary Table S S3.2) and MOPS (**e**, medium 3.1 in Table S S3.3) under different combinations of E_{ox}, E_{red}, and *d* values. The dots and shaded areas represent the average and standard deviation of the pH values across all *y* coordinates at the same *x* coordinates. The red and blue bars represent the positions of the oxidizing and reducing electrodes with potentials E_{ox} and E_{red} *vs.* RHE, respectively. Bulk solution pH = 7.2; fluidic flow rate, 0.1 mL/min. Additional experimental conditions can be found in Methods.

A microfluidic device of Au IDEs under a constant flow rate was constructed under a fluorescent confocal microscope to demonstrate the proposed electrochemical control of pH microenvironments (Fig. 3.4a, 3.4b and Supplementary S4; see Supplementary Note S3.1 for the rational of choosing Au as electrode materials). Two pairs of Au finger electrodes, each of 20-μm width with a spacing of either 10 or 50 μm, were designated as two working electrodes in a bi-potentiostat configuration with Ag pseudo-reference electrode and indium-tin oxide counter electrode (Fig. 3.4b, see Methods). As schematically depicted in Fig. 3.1c, the anodic working electrode with potential E_{ox} oxidizes hydroquinone (H_2Q) into quinone (Q) with the release of two

protons, while the cathodic working electrode with potential E_{red} reduces quinone to hydroquinone with the consumption of two protons. The diffusion of chemical species between the electrode pairs is expected to yield a lower pH near the oxidizing electrode and a higher pH near the reducing one, hence a one-dimensional pH gradient normal to the individual finger electrodes.

The hypothesized pH gradient, presumably controllable by the E_{ox} and E_{red} values, was spatially mapped within the IDE-bearing microfluidic channel by confocal microscope at a spatial resolution of about 650 nm with pH-sensitive ratiometric fluorescent probe seminaphthorhodafluor-4F 5-(and-6) carboxylic acid (C-SNARF-4)[9,11,48], whose ratio of emission intensities at 592 and 653 nm (Fig. 3.4a) reports the local pH after the establishment of a calibration curve (Supplementary Fig. S3.5). Control experiments with C-SNARF-4 showed that within our detection limit the pH probe does not inhibit the PCET processes (Supplementary Fig. S3.6) and the DHBS-based electrochemical process does not degrade the probe's optical property (Supplementary Fig. S3.7). In order to observe the maximal pH gradients exerted by electrochemistry without significant optical interference from the metallic Au electrodes, the microscope focal plane was fixed at 5 μm above the electrode (see Methods, Note S3.2). Because the local pH microenvironment near the electrode differs more profoundly from the bulk as the one at 5 μm above the electrode, our experimentally reported pH gradient is an underestimate of the actual pH gradient that many biological systems will indeed experience. While a confocal image hence the pH spatial profile is two-dimensional (Fig. 3.4c), the aforementioned one-dimensional nature of the presumed pH gradient allows us to present the generated pH spatial profile as one-dimensional plot by averaging the pH values at the same x coordinate along the direction normal to the finger electrodes.

Spatiotemporal programming of pH microenvironments by DHBS-based electrochemistry

Steady-state pH gradients programmed by E_{appl} values were demonstrated in two of the most commonly used biological buffer solutions, phosphate-buffered and MOPS-buffered growth medium (Fig. 3.4d and 3.4e; medium 2.2 and 3.1 in Supplementary Table S3.2 and S3.3, respectively). The averaged pH values under different combinations of time-invariant E_{appl} values (E_{ox} and E_{red}), along with the measurement standard deviations, were plotted along the *x* coordinate normal to the finger electrodes where the location of oxidizing and reducing electrodes were marked as red and blue bars, respectively (Fig. 3.4d and 3.4e, see Methods). In both mediums at a flow rate of 0.1 mL/min, pH spatial gradients between the anodic and cathodic electrodes were observed, and as expected, with a higher pH near the anode and a lower pH near the cathodic. An increase of E_{ox} under a constant E_{red} will lead to a much larger pH difference hence a steeper pH gradient; ditto with a decrease of E_{red} under a constant E_{ox}. Our observed pH gradients are within the range for the biofilms of *P. aeruginosa*[48]. The spatially repeated pattens of pH gradients are the manifesto of the reliability of the generated pH spatial gradients.

Moreover, reducing the distance *d* between oxidizing and reducing finger electrodes from 50 μm (left half of Fig. 3.4d and 3.4e) to 10 μm (right half of Fig. 3.4d and 3.4e) leads to more pronounced spatial pH gradients. The largest slope of pH gradient amounts to 0.02 pH/μm (E_{ox} = 1.47 V, E_{red} = 0.27 V, d = 10 μm in MOPS medium). Such a large slope of pH gradient can hardly be achieved in conventional methods based on passive diffusion or convection in lieu of active electrochemical modulation in microfluidic channels (Supplementary Table S3.4)[18-21,53,54]. Our results indicate that electrochemical PCET process is capable of creating a 12-mV difference in proton motive force across a distance of 1 μm, or 0.12 V across 10 μm. Given the sensitivity of oxidative phosphorylation towards proton motive force, our tool can pose an appreciable perturbation

towards organism's aerobic respiration and overall metabolism at single-cell level for prokaryotes and subcellular level for eukaryotic systems.

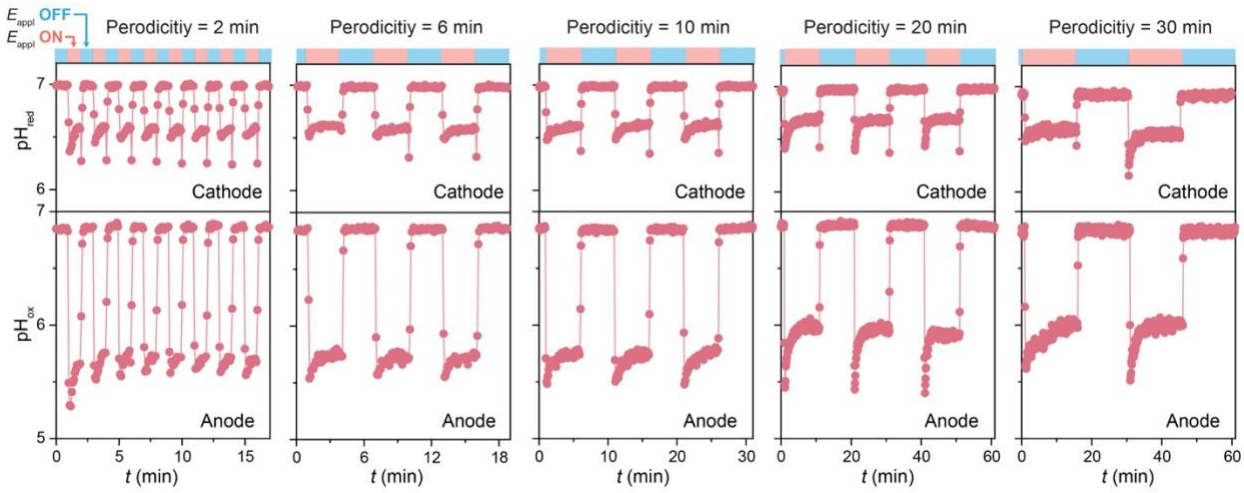


Figure 3.5. Temporal responses of electrochemically controlled pH microenvironments. The local pH values 5 μm above the centers of the reducing (top, pH_{red}, "Cathode") and oxidizing electrodes (bottom, pH_{ox}, "Anode") were plotted every 5 seconds with the provision of E_{appl} on and off under different periodicities ranging from 2 minutes to 30 minutes. When E_{appl} were applied, E_{red} = 0.27 V and E_{ox} = 1.47 V *vs.* RHE. 10-mM MOPS growth medium (bulk pH = 7.2; medium 3.1 in Table S3.3). An exemplary evolution of time-dependent pH gradient when periodicity = 1 minute was shown in Video S3.1.

The temporal resolution of electrochemically driven pH perturbation was shown to be at $10^0 \sim 10^1$ seconds with good repeatability. One proposed benefit of electrochemically controlled pH microenvironments is the high temporal resolution, as electrochemical processes can be quickly turned on or off with the application or withdrawal of electrochemical potentials. In MOPS medium (medium 3.1 in Supplementary Table S3.3), we examined the temporal pH response with the provision of E_{appl} on and off under different periodicities ranging from 2 minutes to 30 minutes. Given the high-dimensionality of the time-dependent pH gradients (Supplementary Video S3.1),

the local pH values 5 μm above the centers of the reducing (pH_{red}, top row in Fig. 3.5) and oxidizing electrodes (pH_{ox}, bottom row in Fig. 3.5) were plotted every 5 seconds (see Methods). We have observed good repeatability of the established pH microenvironments across all periodicity values (Supplementary Fig. S3.8). Moreover, stable pH values were achieved within about 10 seconds after the voltage switches, even in cases when the periodicity is only 2 minutes (Fig. 3.5). Such a fast temporal resolution of pH modulation is at least one order-of-magnitude faster than the ~10^2 seconds ones in conventional methods based on passive diffusion or convection (Supplementary Table S3.4)[18,20,53,54]. Thanks to the fast-switching nature of electrochemistry, it is feasible now to perturb the extracellular pH microenvironments faster than the responses of cellular translation and transcription[55-57] at single-cell if not subcellular levels.

A simulation-driven inquiry into the general applicability of electrochemical pH control

Additional numerical simulations based on finite-element methods were conducted to inquire into the parameter range compatible with electrochemically controlled pH microenvironments, as we envision the presented tool will be generally applicable towards different biological systems. A two-dimensional model built on COMSOL Multiphysics (version 5.3) was constructed to reflect not only the cross-section of electrochemical microfluidic setup (d = 50 μm) under a constant lamellar flow but also the electrochemical properties of Au IDEs based on our experimental results (left in Fig. 3.6a, see Methods). Same as our experimental evaluation about the temporal resolution of electrochemical pH perturbation (Fig. 3.5), the pH profiles including pH_{ox} and pH_{red} were numerically calculated under different conditions (right in Fig. 6a, Supplementary Fig. S3.9). As a surrogate of the pH range achievable by electrochemistry, the pH difference $\Delta pH = pH_{red} - pH_{ox}$ was calculated as a function of E_{ox}, E_{red}, the phosphate buffer concentration (C_{buffer}), and the DHBS concentration (C_{DHBS}). When E_{red} = 0.67 V *vs.* RHE (Fig. 3.6b), there exists a wide range of

parameter combinations when ΔpH > 0.7, the common pH differences across bacterial biofilms[9,58] and the cancerous tissues[59-61]. This indicates that the presented method of electrochemical pH modulation is amenable to many different extracellular mediums.

Generally, larger value of ΔpH is calculated under a relatively smaller C_{buffer}, larger C_{DHBS}, and larger E_{ox}; meanwhile, E_{red} poses a much smaller impact towards ΔpH (Supplementary Fig. S10) and a smaller *d* value tends to reduce the magnitude of ΔpH (Supplementary Fig. S11) although boosting the slope of pH gradient (Fig. 3.4d and 3.4e). A smaller ΔpH is expected with a smaller *d* value, because it is harder to maintain a pH difference between IDEs of a closer distance. When the solution buffering capability decreases (smaller C_{buffer}) or there are more protons released/consumed from hydroquinone/quinone redox (larger C_{DHBS}), the electrochemical PCET process will pose a much larger perturbation towards the extracellular pH (Supplementary Fig. S3.12). Because ambiently the predominant species for DHBS is the reduced hydroquinone form owing to its positive redox potential (0.9 V *vs.* RHE from Fig. 3.2b), a change of E_{ox} value will lead to significant change of local proton releases from hydroquinone oxidation, while a relatively mild change of proton consumption will incur from the change of E_{red} value. As we know now that not every parameter is equally important towards maximizing ΔpH, such insights will benefit future designs of electrochemical pH microenvironments for biological appliations.

Conclusion

While pH microenvironments are ubiquitous in biological systems, spatiotemporal perturbation of local pH conditions for biological application has been rare and challenging to achieve. The rarity of reported spatiotemporal pH modulation resides on the lack of effective methods that changes local pH environments with high biocompatibility and good spatial/temporal resolution. Based on the equally ubiquitous PCET nature of electrochemical processes, this work reports the feasibility

of using electrochemical PCET reactions from biocompatible quinone/hydroquinone redox couple to generate biologically relevant pH gradients in bacterial growth medium with steeper spatial gradient and faster temporal response. As the extent of PCET process can be controlled by applied electrochemical potential, the generated spatiotemporal pH profiles are indeed digitally programmed by electric signals. Deploying biocompatible electrochemistry with judicious device design offers a venue to transduce digital signals into spatiotemporal profiles of local pH, hence a larger degree of freedom to perturb and investigate microbial systems under heterogenous microenvironments in the future.

Materials and Methods

Chemicals

The chemicals, unless specified, were purchased from Sigma-Aldrich, and used as received. The interdigitated electrodes are purchased from NanoSPR LLC (BA1810 & BA1850). ITO glass was purchased from SPI supplies (LOT#1231220, 30-60Ω, 22×40mm, 1.5). Silver paste was purchased from Ted Pella. Chemical resistant tapes and Epoxy 1C were purchased from McMaster Carr. Plastic tubing and fitting were purchased from IDEX Health & Science. Gold electrodes (CHI 101, diameter = 2 mm), Platinum electrodes (CHI 102, diameter = 2 mm) and glassy carbon electrodes (CHI 104, diameter = 3 mm) were purchased from CH Instruments.

Electrochemical characterizations

All electrochemical experiments were conducted via using Gamry Instruments Interface potentiostat.

Cyclic Voltammetry. Cyclic voltammetry was conducted in a H-cell with three-electrode system with the electrolyte of 1× PBS solution (pH = 7.4, medium 1.1 in Table S1) and 5 mM BQDS or

DHBS. Three different working electrodes were used, including a glassy carbon electrode (diameter = 3 mm), a Pt electrode (diameter = 2 mm) and an Au electrode (diameter = 2 mm). An Au mesh was used as the counter electrode, and an Ag/AgCl (1M KCl) electrode was used as the reference electrode. The redox potential of the Ag/AgCl (1M KCl) electrode was calibrated by a Zobell's solution[62] with a redox potential of 227 mV *vs.* RHE (Supplementary Figure S3.12a). Various scan rates were applied to the electrode, including 20, 50, 100, 300, 500 mV/s. The redox potential was determined by averaging the potential of the oxidation and reduction peaks.

Rotating disk electrode. The rotating disk electrode (Pine Research, Inc., AFE6R1PT) experiment was conducted using a modulated speed rotator (Pine Research, Inc., AFMSRCE) and the same counter and reference electrodes as the cyclic voltammetry. A gold rotating disk electrode (diameter = 5 mm) was used, and the electrolyte consists of 20 mM BQDS or DHBS in 10 mM PBS solution (medium 1.2 in Table S3.1). The electrolyte was saturated with air and N_2 before the electrochemical measurement to exclude the interference of O_2 during hydroquinone oxidation. Background correction was performed by subtracting the current of 10 mM PBS solution from the current of 20 mM BQDS or DHBS in 10 mM PBS solution. The rotation speed was set at 100, 225, 400, 625, 900, 1225, and 1600 rpm. The electron transfer number was calculated using the Koutecký-Levich equation with the diffusion coefficient obtained from the literature.

The characterization of microbial cultures

The PAO1 and PA14 strain of *P. aeruginosa* was obtained from Dianne Newman's lab at Caltech. The bacteria were cultured at 30 °C in glassy tubes for all the growth curve measurements if not mentioned specially. Two buffer mediums were used: phosphate-buffered and MOPS succinate mediums. The phosphate-buffered succinate medium (medium 2.1 in Table S3.2) includes 4.15 mM KH_2PO_4, 38.85 mM K_2HPO_4, 42.8 mM NaCl, 9.3 mM NH_4Cl, 40 mM sodium succinate, 1

mM $MgSO_4$, and 1mL/L 1× SL-10 trace element solution. The MOPS succinate medium (medium 3.2 in Table S3) includes 100 mM MOPS, 50 mM NH_4Cl, 3.7 mM KH_2PO_4, 1 mM $MgSO_4$, 40 mM sodium succinate, and 7.2 μM $FeSO_4$. The pH was adjusted to 7.2 by using HCl or NaOH. Absorbance at 600 nm (OD_{600}) was measured by using an Agilent Cary 60 UV-Vis spectrophotometer. Each condition was tested in triplicates.

Carbon source. The PAO1 strain of *P. aeruginosa* was cultured in phosphate-buffered medium including 30 mM succinate (medium 2.1 in Table S2) at 30 °C without shaking. The succinate was replaced by 20 mM BQDS or 20 mM DHBS, providing an equivalent carbon amount. A phosphate-buffered medium without a carbon source was also prepared for the control experiment. The OD_{600} was monitored approximately every 8 hours for 3 days to collect the growth curve.

Buffer concentration. The phosphate-buffered succinate mediums (medium 2.1 in Table S3.2) with different concentrations (10, 20, 43 mM) of phosphate buffer were prepared and were inoculated with the same amount of *P. aeruginosa* PAO1 strain culture. The PAO1 strain culture was incubated at 30 °C with a shaking speed of 200 rpm. The OD_{600} was monitored approximately every 6 hours for 2 days to collect the growth curve.

BQDS/DHBS biocompatibility. The PAO1 strain of *P. aeruginosa* was cultured in 10 mM phosphate-buffered succinate medium (medium 2.1 in Table S3.2) with different consternation of BQDS (5mM, 13 mM and 15 mM) or DHBS (1mM, 5 mM and 15 mM) at 30 °C with a rotating speed of 200 rpm. Control experiments were also conducted by preparing 10 mM phosphate-buffered succinate mediums (medium 2.1 in Table S3.2) with BQDS/DHBS but without PAO1. The OD_{600} was monitored every 2-8 hours, depending on the stages of bacterial growth, for 2 days to collect the growth curve.

Minimum inhibition concentration measurement. The minimum inhibition concentration measurement was conducted by using a plate reader (TECAN M1000). The 10 mM MOPS succinate medium (medium 3.1 in Table S3) with a series of DHBS concentrations ranging from 2 mM to 256 mM was prepared in a 96-well plate. The PA14 strain of *P. aeruginosa* was cultured overnight with an initial OD_{600} of approximately 0.5. The PA14 strain culture was then diluted in 10 mM MOPS medium at ratios of 1/10, $1/10^2$, $1/10^2$, $1/10^3$, $1/10^4$, and $1/10^5$, and the same amount was added to each well in the 96-well plate. The 96-well plate was monitored every 20 minutes at room temperature for 24 hours using the plate reader with shaking to collect growth curve. The minimum inhibition concentration was determined by the lowest concentration of DHBS that will inhibit the visible growth of the PA14 strain of *P. aeruginosa*.

IC_{50} estimation. The 10 mM MOPS succinate medium with DHBS concentrations of 0 mM, 5 mM, 15 mM, 30 mM, and 100 mM were prepared. The PA14 strain of *P. aeruginosa* was cultured overnight with an initial OD of approximately 0.5. The PA14 strain culture was diluted to 1/10, $1/10^2$, $1/10^2$, $1/10^3$, $1/10^4$, $1/10^5$, and $1/10^6$ with 10 mM MOPS medium (medium 3.1 in Table S3.3) and equal volumes were added to the DHBS-containing medium solutions. 2 μL of the mixed culture was inoculated onto an agar plate and incubated at 30 °C for 24 hours. The half maximal inhibitory concentration (IC_{50}) was estimated based on the comparison at $1/10^3$ dilution.

BQDS/DHBS biocompatibility at different pH conditions. The 10 mM phosphate-buffered succinate medium (medium 2.2 in Table S3.2) was prepared and adjusted to pH 5 and pH 7 using HCl. For each pH, three conditions were tested: no hydroquinone, 15 mM BQDS, and 15 mM DHBS. The PAO1 strain culture was incubated at 30 °C with a shaking speed of 200 rpm for a total of 6 conditions. The OD_{600} was monitored every 2-8 hours based on the bacterial growth stages for 2 days to collect the growth curve. Similar experiments were conducted with 10 mM

MOPS (medium 3.1 in Table S3.3) succinate medium for PA14 strains of *P. aeruginosa*. The doubling time was calculated from the exponential fitting of the log phase in the growth curve and a two-sample unequal variance t-test (tails = 1) was performed to obtain p-value for the two conditions at the same pH.

The construction of electrochemical microfluidic device

A three-electrode electrochemical system was established in a microfluidic flow device. An ITO glass (SPI supplies, 30-60Ω, 22×40mm, 1.5) substrate was etched in 6 M HCl to create two distinct conductive regions. One region served as a counter electrode, while the other was coated with the Ag paste to function as a pseudo reference electrode. The pseudo reference electrode was calibrated using the Zobell's solution[62] and had a redox potential of 270 mV *vs.* RHE (Supplementary Figure S3.12B). Gold interdigitated electrodes with varying gap widths of 10 and 50 μm (NanoSPR LLC, BA1810 & BA1850) were used as working electrodes. Each interdigitated electrode consisted of two pairs of Au finger electrodes, each with a width of 20 μm width and a variable in-between spacing of either 10 or 50 μm. A cap designed in AutoCAD was fabricated using a 3D printer (Dremel Digilab 3D45) and assembled with the electrodes and tubing. The epoxy (Loctite 1C 1C) was used to seal the device and prevent leakage.

Optical characterizations using florescent confocal microscopy

The fluorescent spectra of C-SNARF-4. The C-SNARF-4 was dissolved in dimethyl sulfoxide (DMSO) to prepare a stock solution which was stored at –20 °C. The C-SNARF-4 stock solution was diluted to 10 μM by using PBS solution for further measurement. The ultraviolet-visible (UV-Vis) spectrum was recorded using an Agilent Cary 60 UV-Vis spectrophotometer. The fluorescence spectrum was measured using an Ocean optics Inc. photoluminescence with a light source at 462 nm.

The setting and preparation for confocal imaging. The confocal microscopy measurements were conducted using an inverted laser confocal microscope (LEICA SP8 SMD) with an HC PL FLUOTAR 10×/0.30 dry lens. The excitation wavelength was set to 488 nm, and signals were collected from two channels: 592±30 nm and 653±30 nm. The pinhole was set as 0.28 A.U. (20 μm). The *x*-*y* resolution was approximately 6.5×10^2 nm, and the *z* resolution was approximately 4.8×10^3 nm. A syringe pump was used to flow 10 mM phosphate-buffered or MOPS succinate medium (medium 2.2 in Table S3.2, medium 3.1 in Table S3.3) containing 15 mM hydroquinone, and 10 μM C-SNARF-4. A series of flow rates (0.01, 0.05, 0.1, 0.2, 0.4 mL/min) were tested (Supplementary Fig. S13) and a typical flow rate of 0.1 mL/min was used for all the main figures. Succinate mediums of varying pH values (5.0, 5.5, 6.0, 6.5, 7.0, 7.5) were used to calibrate the pH before electrochemical measurements (Supplementary Fig. S3.5).

The confocal microscopy imaging. For the electrochemical measurements, 10 mM phosphate-buffered succinate medium (pH 7.2, medium 2.2 in Table S2) and 10 mM MOPS succinate medium (pH 7.2, medium 3.1 in Table S3.3) containing 15 mM hydroquinone and 10 μM C-SNARF-4 were used. Bi-potentiostat measurements were conducted using two Gamry Interface potentiostats. At first, cyclic voltammetry was performed on each finger electrode (Supplementary Figure S3.14), followed by a 1-min chronoamperometry at a fixed potential on each finger electrode. The microscope focal plane was fixed at 5 μm above the electrode, and an *xy*t scan was conducted in a 1024 format with a time interval of 2.7 seconds, starting 10 seconds before continuing until 30 seconds after the chronoamperometry. The potentials on two finger electrodes were changed, and each condition was tested in triplicates. The confocal image captured at the middle point of the chronoamperometry was used to represent the spatial gradient for each condition.

The response time measurements. To alter the periodicity of electrochemical potentials, chronoamperometries were conducted for durations of 1 minutes, 3 minutes, 5 minutes, 10 minutes and 15 minutes, each followed by an interval of the same duration as the chronoamperometry. Typically, three cycles (potential ON/OFF) were performed, although the numbers of cycles could be adjusted based on the periodicity. Confocal images were collected as *x*-*y* mapping (1024×1024 pixels) with a time interval of 5 seconds for all cycles. The 5-second interval time was set slightly longer than the minimum time (2.7 seconds) required to capture a 1024-pixel image, allowing the interval to be divisible by the periodicity while maintaining sufficient temporal resolution to show response times of around 10 seconds.

Data analysis of confocal images. All confocal images were processed using MATLAB. First, the ratio of intensities from two channels (592±30 nm and 653±30 nm) was calculated for each frame. The intensity ratio image of two channels, 592 nm and 653 nm (Int_{653}/Int_{592}), was divided into 128 rectangle areas, each with a width of approximately 2.5 μm (8×1024 pixels) in the direction perpendicular to the electrodes. Calibration curves were built using a second-order polynomial fitting for each rectangle to eliminate interference from the electrodes (20 μm width). The intensity ratios in each rectangle were averaged and converted to pH values using the corresponding calibration curve. Finally, the pH gradient along the direction perpendicular to electrodes (*x* coordinate) was plotted. The average and standard deviation of triplicates were also analyzed to plot spatial gradient at different applied potentials. For temporal change in pH, a specific position, either the cathode or anode, was chosen, and the local pH was analyzed for all frames and plotted along the time coordinate.

Numerical simulations based on finite-element methods

A model was developed based on finite element analysis (FEA) via using "Electroanalysis" module in COMSOL Multiphysics (Version 5.3). The two-dimensional geometry consisted of a cross section of the microfluidic flow device (Fig. 6a) with a diffusion layer of 200 μm. The interfaces of interdigitated electrodes were located along the bottom boundary of the cross-section. The width of the finger electrodes was set at 20 μm and the gap between the finger electrodes could be either 10 μm or 50 μm. The ten pairs of the finger electrodes were simulated within the model. The minimum pH (pH_{ox}) was observed 5 μm above the anode of the 8th electrode pair, while the maximum pH (pH_{red}) was observed 5 μm above the cathode of the 8th electrode pair. The pH difference was defined as the maximum pH minus the minimum pH ($\Delta pH = pH_{red} - pH_{ox}$).

The model includes phosphate buffer and hydroquinone/quinone redox species. The chemical equilibriums were based on the following equations:

$$H_3PO_4 \rightleftarrows H_2PO_4^- + H^+ \quad (1)$$

$$H_2PO_4^- \rightleftarrows HPO_4^{2-} + H^+ \quad (2)$$

$$HPO_4^{2-} \rightleftarrows PO_4^{3-} + H^+ \quad (3)$$

$$H_2Q \rightleftarrows HQ^- + H^+ \quad (4)$$

$$HQ^- \rightleftarrows Q^{2-} + H^+ \quad (5)$$

with the dissociation constant of 6.9×10^{-3} for reaction (1); 6.2×10^{-8} for reaction (2); 4.8×10^{-13} for reaction (3); 1.6×10^{-10} for reaction (4); and 4.0×10^{-12} for reaction (5), which are obtained from literature[35,63].

The diffusion of species was simulated based on the following equations (6). D_{H^+} is the diffusion coefficient of proton, which is 9.3×10^{-9} m^2/s[64]; D_Q is the diffusion coefficient of quinone, which is 4.2×10^{-10} m^2/s[46]; D_{H_2Q}, D_{HQ^-} and $D_{Q^{2-}}$ are the diffusion coefficients of hydroquinone, HQ^-

and Q^{2-} which are 2.7×10^{-10} m^2/s[46]; $D_{H_3PO_4}$, $D_{H_2PO_4^-}$, $D_{HPO_4^{2-}}$ and $D_{PO_4^{3-}}$ are the diffusion coefficients of phosphoric acid, $H_2PO_4^-$, HPO_4^{2-}, HPO_4^- and PO_4^{3-} which are 8.7×10^{-10} m^2/s[65].

$$\frac{\partial\phi(r,t)}{\partial t} = \mathrm{D}\nabla^2\phi(r,t) \tag{6}$$

The equilibrium redox potential (E_{eq}) was obtained from the cyclic voltammetry of DHBS (Fig. 3.2b), which is 1.02 V *vs.* RHE. On the electrode surface, hydroquinone oxidation occurred on the anode and the quinone reduction occurred on the cathode.

$$H_2Q - 2e^- - 2H^+ \rightarrow Q \tag{7}$$

$$Q + 2e^- + 2H^+ \rightarrow H_2Q \tag{8}$$

On the surface of interdigitated electrodes, the electrochemical reaction was simulated as the equations (9) and (10).

$$i_{loc} = i_0\left(\frac{[H_2Q]}{C_{H_2Q}}exp\left(\frac{\alpha_a F\eta}{RT}\right) - \frac{[Q]}{C_Q}\left(\frac{[H^+]}{C_{H^+}}\right)^2 exp\left(\frac{-\alpha_c F\eta}{RT}\right)\right) \tag{9}$$

$$J_{H_2Q} = -J_Q = \frac{i_{loc}}{2F} \tag{10}$$

In equations (8) and (9), i_{loc} stood for the local current density on the electrode surface. J_{H_2Q} and J_Q represented the local flux of H_2Q and Q from electrolyte. α_a and α_c is the transfer coefficient, which is equal to 0.5. *F* is the Faraday constant. *R* is the gas constant and *T* is the temperature. The local species concentration is described by [species], and $C_{species}$ is concentration in the bulk solution at *T*. i_0 is the local exchange current density of Au electrode in PBS solution, which was obtained by Tafel analysis of cyclic voltammetry of 5 mM DHBS on gold disk electrode (diameter =2 mm) (Supplementary Fig. S3.15).

For a typical condition, the initial electrolyte contained 10 mM phosphate buffer (c_{buffer}), 15 mM hydroquinone (c_{H_2Q}) and 1×10^{-6} mM quinone (c_Q). The electrolyte flow was simulated as constant lamellar flow with a vertical convection rate of 120 μm/s (0.1 mL/min).

Different parameters including concentration of buffer (c_{buffer}), concentration of hydroquinone (c_{H_2Q}), concentration of quinone (c_Q), applied oxidation potential (E_{ox}), and applied reduction potential (E_{red}) were screened by the MATLAB.

References

1 Jo, J., Price-Whelan, A. & Dietrich, L. E. Gradients and consequences of heterogeneity in biofilms. *Nat. Rev. Microbiol.* **20**, 593-607 (2022).

2 Stewart, P. S. & Franklin, M. J. Physiological heterogeneity in biofilms. *Nat. Rev. Microbiol.* **6**, 199-210 (2008).

3 Kato, Y. *et al.* Acidic extracellular microenvironment and cancer. *Cancer Cell Int.* **13**, 1-8 (2013).

4 Hatefi, Y. The mitochondrial electron transport and oxidative phosphorylation system. *Annu. Rev. Biochem.* **54**, 1015-1069 (1985).

5 Kaila, V. R. & Wikström, M. Architecture of bacterial respiratory chains. *Nat. Rev. Microbiol.* **19**, 319-330 (2021).

6 Senior, A. E. ATP synthesis by oxidative phosphorylation. *Physiol. Rev.* **68**, 177-231 (1988).

7 Liberti, M. V. & Locasale, J. W. The Warburg effect: how does it benefit cancer cells? *Trends Biochem. Sci.* **41**, 211-218 (2016).

8 Behbahani, S. B. *et al.* pH variation in medical implant biofilms: Causes, measurements, and its implications for antibiotic resistance. *Front. Microbiol.* **13**, 1028560 (2022).

9 Schlafer, S. *et al.* pH landscapes in a novel five-species model of early dental biofilm. *PLoS One* **6**, e25299 (2011).

10 Fulaz, S. *et al.* Ratiometric imaging of the in situ pH distribution of biofilms by use of fluorescent mesoporous silica nanosensors. *ACS Appl. Mater. Interfaces* **11**, 32679-32688 (2019).

11 Schlafer, S., Kamp, A. & Garcia, J. E. A confocal microscopy based method to monitor extracellular pH in fungal biofilms. *FEMS Yeast Res.* **18**, foy049 (2018).

12 Gupta, P., Sarkar, S., Das, B., Bhattacharjee, S. & Tribedi, P. Biofilm, pathogenesis and prevention—a journey to break the wall: a review. *Arch. Microbiol.* **198**, 1-15 (2016).

13 Dige, I., Baelum, V., Nyvad, B. & Schlafer, S. Monitoring of extracellular pH in young dental biofilms grown in vivo in the presence and absence of sucrose. *J. Oral Microbiol.* **8**, 30390 (2016).

14 Chen, Y. Recent advances in fluorescent probes for extracellular pH detection and imaging. *Anal. Biochem.* **612**, 113900 (2021).

15 Chandra, A. & Singh, N. Cell microenvironment pH sensing in 3D microgels using fluorescent carbon dots. *ACS Biomater. Sci. Eng.* **3**, 3620-3627 (2017).

16 Hollmann, B., Perkins, M., Chauhan, V. M., Aylott, J. W. & Hardie, K. R. Fluorescent nanosensors reveal dynamic pH gradients during biofilm formation. *NPJ Biofilms Microbiomes* **7**, 50 (2021).

17 Schlafer, S. *et al.* Ratiometric imaging of extracellular pH in bacterial biofilms with C-SNARF-4. *Appl. Environ. Microbiol.* **81**, 1267-1273 (2015).

18 Kim, T., Pinelis, M. & Maharbiz, M. M. Generating steep, shear-free gradients of small molecules for cell culture. *Biomed. Microdevices* **11**, 65-73 (2009).

19 Luo, X. *et al.* In situ generation of pH gradients in microfluidic devices for biofabrication of freestanding, semi-permeable chitosan membranes. *Lab Chip* **10**, 59-65 (2010).

20 Zhuang, J., Wright Carlsen, R. & Sitti, M. pH-taxis of biohybrid microsystems. *Sci. Rep.* **5**, 11403 (2015).

21 Kirchhof, K. *et al.* Polyelectrolyte multilayers generated in a microfluidic device with pH gradients direct adhesion and movement of cells. *Lab Chip* **11**, 3326-3335 (2011).

22 Dar, D., Dar, N., Cai, L. & Newman, D. K. Spatial transcriptomics of planktonic and sessile bacterial populations at single-cell resolution. *Science* **373**, eabi4882 (2021).

23 Hatzenpichler, R., Krukenberg, V., Spietz, R. L. & Jay, Z. J. Next-generation physiology approaches to study microbiome function at single cell level. *Nat. Rev. Microbiol.* **18**, 241-256 (2020).

24 Taylor, M. J., Lukowski, J. K. & Anderton, C. R. Spatially resolved mass spectrometry at the single cell: recent innovations in proteomics and metabolomics. *J. Am. Soc. Mass Spectrom.* **32**, 872-894 (2021).

25 Weinberg, D. R. *et al.* Proton-coupled electron transfer. *Chem. Rev.* **112**, 4016-4093 (2012).

26 Mayer, J. M. Proton-coupled electron transfer: a reaction chemist's view. *Annu. Rev. Phys. Chem.* **55**, 363-390 (2004).

27 Lu, S., Guan, X. & Liu, C. Electricity-powered artificial root nodule. *Nat. Commun.* **11**, 1505 (2020).

28 Chen, Y., Wang, J., Hoar, B. B., Lu, S. & Liu, C. Machine learning–based inverse design for electrochemically controlled microscopic gradients of O_2 and H_2O_2. *Proc. Natl. Acad. Sci. U.S.A.* **119**, e2206321119 (2022).

29 Jung, H. S. *et al.* CMOS electrochemical pH localizer-imager. *Sci. Adv.* **8**, eabm6815 (2022).

30 O'Sullivan, B. *et al.* A simulation and experimental study of electrochemical pH control at gold interdigitated electrode arrays. *Electrochim. Acta* **395**, 139113 (2021).

31 Kracke, F., Vassilev, I. & Krömer, J. O. Microbial electron transport and energy conservation–the foundation for optimizing bioelectrochemical systems. *Front. Microbiol.* **6**, 575 (2015).

32 Tuon, F. F., Dantas, L. R., Suss, P. H. & Tasca Ribeiro, V. S. Pathogenesis of the *Pseudomonas aeruginosa* biofilm: a review. *Pathogens* **11**, 300 (2022).

33 Grace, A., Sahu, R., Owen, D. R. & Dennis, V. A. *Pseudomonas aeruginosa* reference strains PAO1 and PA14: A genomic, phenotypic, and therapeutic review. *Front. Microbiol.* **13**, 1023523 (2022).

34 Guin, P. S., Das, S. & Mandal, P. Electrochemical reduction of quinones in different media: a review. *Int. J. Electrochem. Sci.* **2011**, 816202 (2011).

35 Quan, M., Sanchez, D., Wasylkiw, M. F. & Smith, D. K. Voltammetry of quinones in unbuffered aqueous solution: reassessing the roles of proton transfer and hydrogen bonding in the aqueous electrochemistry of quinones. *J. Am. Chem. Soc.* **129**, 12847-12856 (2007).

36 Gerken, J. B. *et al.* Comparison of quinone-based catholytes for aqueous redox flow batteries and demonstration of long-term stability with tetrasubstituted quinones. *Adv. Energy Mater.* **10**, 2000340 (2020).

37 Er, S., Suh, C., Marshak, M. P. & Aspuru-Guzik, A. Computational design of molecules for an all-quinone redox flow battery. *Chem. Sci.* **6**, 885-893 (2015).

38 Wedege, K., Dražević, E., Konya, D. & Bentien, A. Organic redox species in aqueous flow batteries: redox potentials, chemical stability and solubility. *Sci. Rep.* **6**, 39101 (2016).

39 Hong, Y. & Brown, D. G. Electrostatic behavior of the charge-regulated bacterial cell surface. *Langmuir* **24**, 5003-5009 (2008).

40 Fröhlich, E. The role of surface charge in cellular uptake and cytotoxicity of medical nanoparticles. *Int. J. Nanomed.*, 5577-5591 (2012).

41 Wilson, W. W., Wade, M. M., Holman, S. C. & Champlin, F. R. Status of methods for assessing bacterial cell surface charge properties based on zeta potential measurements. *J. Microbiol. Methods* **43**, 153-164 (2001).

42 Roginsky, V. & Barsukova, T. Kinetics of oxidation of hydroquinones by molecular oxygen. Effect of superoxide dismutase. *J. Chem. Soc., Perkin Trans. 2*, 1575-1582 (2000).

43 Jiang, Y. *et al.* Selective electrochemical H_2O_2 production through two-electron oxygen electrochemistry. *Adv. Energy Mater.* **8**, 1801909 (2018).

44 Treimer, S., Tang, A. & Johnson, D. C. A Consideration of the application of Koutecký-Levich plots in the diagnoses of charge-transfer mechanisms at rotated disk electrodes. *Electroanalysis* **14**, 165-171 (2002).

45 Zhang, S., Li, X. & Chu, D. An organic electroactive material for flow batteries. *Electrochim. Acta* **190**, 737-743 (2016).

46 Ji, X., Banks, C. E., Silvester, D. S., Wain, A. J. & Compton, R. G. Electrode kinetic studies of the hydroquinone−benzoquinone system and the reaction between hydroquinone and ammonia in propylene carbonate: application to the indirect electroanalytical sensing of ammonia. *J. Phys. Chem. C* **111**, 1496-1504 (2007).

47 Singh, V., Kim, S., Kang, J. & Byon, H. R. Aqueous organic redox flow batteries. *Nano Res.* **12**, 1988-2001 (2019).

48 Hunter, R. C. & Beveridge, T. J. Application of a pH-sensitive fluoroprobe (C-SNARF-4) for pH microenvironment analysis in *Pseudomonas aeruginosa* biofilms. *Appl. Environ. Microbiol.* **71**, 2501-2510 (2005).

49 Yang, L. *et al.* Distinct roles of extracellular polymeric substances in *Pseudomonas aeruginosa* biofilm development. *Environ. Microbiol.* **13**, 1705-1717 (2011).

50 Andrews, J. M. Determination of minimum inhibitory concentrations. *J. Antimicrob. Chemother.* **48**, 5-16 (2001).

51 Burlingham, B. T. & Widlanski, T. S. An intuitive look at the relationship of K_i and IC_{50}: a more general use for the Dixon plot. *J. Chem. Educ.* **80**, 214 (2003).

52 Laviron, E. Theoretical study of a 1*e*, $1H^+$ surface electrochemical reaction (four-member square scheme) when the protonation reactions are at equilibrium. *J. Electroanal. Chem.* **109**, 57-67 (1980).

53 Hausfeld, A. D. Isoelectric focusing: pH gradients established with simple buffers and a cation-selective membrane. *Anal. Biochem.* **212**, 237-246 (1993).

54 Nawa-Okita, E., Nakao, Y., Yamamoto, D. & Shioi, A. A molecular assembly machine working under a quasi-steady state pH gradient. *Bull. Chem. Soc. Jpn.* **93**, 604-610 (2020).

55 Fröhlich, F. *et al.* Multi-experiment nonlinear mixed effect modeling of single-cell translation kinetics after transfection. *NPJ Syst. Biol. Appl.* **4**, 42 (2018).

56 Morisaki, T. *et al.* Real-time quantification of single RNA translation dynamics in living cells. *Science* **352**, 1425-1429 (2016).

57 Leonhardt, C. *et al.* Single-cell mRNA transfection studies: delivery, kinetics and statistics by numbers. *Nanomed.: Nanotechnol. Biol. Med.* **10**, 679-688 (2014).

58 Allan, V., Macaskie, L. & Callow, M. Development of a pH gradient within a biofilm is dependent upon the limiting nutrient. *Biotechnol. Lett.* **21**, 407-413 (1999).

59 Swietach, P., Vaughan-Jones, R. D., Harris, A. L. & Hulikova, A. The chemistry, physiology and pathology of pH in cancer. *Philos. Trans. R. Soc. B: Biol. Sci.* **369**, 20130099 (2014).

60 Webb, B. A., Chimenti, M., Jacobson, M. P. & Barber, D. L. Dysregulated pH: a perfect storm for cancer progression. *Nat. Rev. Cancer* **11**, 671-677 (2011).

61 Zhang, X., Lin, Y. & Gillies, R. J. Tumor pH and its measurement. *J. Nucl. Med.* **51**, 1167-1170 (2010).

62 Nordstrom, D. K. Thermochemical redox equilibria of ZoBell's solution. *Geochim. Cosmochim. Acta* **41**, 1835-1841 (1977).

63 Lide, D. R. *CRC handbook of chemistry and physics*. Vol. 85 (CRC press, 2004).

64 Amdursky, N., Lin, Y., Aho, N. & Groenhof, G. Exploring fast proton transfer events associated with lateral proton diffusion on the surface of membranes. *Proc. Natl. Acad. Sci. U.S.A.* **116**, 2443-2451 (2019).

65 Leaist, D. G. Diffusion in dilute aqueous solutions of phosphoric acid. Verification of the limiting law for diffusion of weak electrolytes. *J. Chem. Soc., Faraday Trans. 1* **80**, 3041-3050 (1984).

Supplementary Information

Supplementary Notes

Note S3.1: Choice of electrode materials in the electrochemical microfluidic system

In this work, we evaluated three common electrode materials, including glassy carbon (GC), platinum (Pt), and gold (Au), as the potential electrode materials used in the electrochemical microfluidic system equipped with interdigitated electrode (IDEs). Despite its attractive electrochemical behaviors that we found, GC was not chosen owing to the technical challenge of its deposition and patterning on IDE substrate.[1] Pt was not chosen largely because we are concerned of its potential toxicity during electrochemical processes.[2],. Finally, Au was chosen of the materials for our IDE setup thanks to its tested biocompatibility and known commercial availability.

Note S3.2: The selection of the focal plane for the pH quantification during the imaging of confocal microscopy

The relative height of the focal plane relative to the IDE substrate, for the pH quantification during the imaging of confocal microscopy, is judiciously chosen based on two factors: First, the focal plane is ought to be as close to the IDE substrate (z height defined as z = 0 μm) as possible, in order to accurately measure the local pH change exerted by the electrochemical PCET process. Nonetheless, optical interface from the IDE substrate may obscure an accurate pH quantification via the confocal microscope hence the focal plane may not be too close to the IDE substrate. Empirically, as exemplified in Fig. S6 during our experiments of pH calibration, we found that a focal plane that is 5 μm away from the IDE substrate in the liquid medium (z = 5 μm) accurately measured the solution pH while a focal plane of smaller z value will render erroneous pH values. Such considerations led to the choice of a focal plane with z = 5 μm for our measurements of pH gradients.

Another note is that the thickness of Au IDEs on the planer substrate (~ 150 nm) does not significantly interfere with our reported pH gradients, because such a thickness is much smaller than the spatial resolution in the z direction of the confocal microscope, roughly in the order of 5 μm

Supplementary Tables

Table S3.1: Phosphate-buffered saline (PBS) solution

Medium 1.1: The original 1× PBS solution

Component	Concentration (mM)
NaCl	137
KCl	2.7
Na_2HPO_4	10
KH_2PO_4	1.8

The above recipe has been used in Figure 3.2A, 3.2B, S3.6, S3.7 and S3.15.

Medium 1.2: 1× PBS solution of 10 mM phosphate buffer

Component	Concentration (mM)
NaCl	137
KCl	2.7
Na_2HPO_4	8.5
KH_2PO_4	1.5

The above recipe has been used in Figure 3.2E, 3.2F, and S3.1, S3.9, S3.10 and S3.11.

Table S3.2: Phosphate-buffered growth medium

Medium 2.1: succinate growth medium with 43 mM phosphate buffer

Component	Concentration (mM)	Concentration (ml/L)
KH_2PO_4	4.15	
K_2HPO_4	38.85	
NaCl	42.8	
NH_4Cl	9.3	
Sodium succinate	40	
$MgSO_4$	1	
1x SL-10 trace element solution		1

The above recipe has been used in Figure 3A and 3B.

Medium 2.2: succinate growth medium of 10 mM phosphate buffer

Component	Concentration (mM)	Concentration (ml/L)
KH_2PO_4	0.97	
K_2HPO_4	9.03	
NaCl	42.8	
NH_4Cl	9.3	
Sodium succinate	40	
$MgSO_4$	1	
1x SL-10 trace element solution		1

The above recipe has been used in Figure 3B, 3E, S5, S8, S12 and S13.

1× SL-10 trace element solution

Component	Concentration (mM)
HCl	68.568
$FeCl_2$	7.545
$ZnCl_2$	0.514
$MnCl_2$	0.505
H_3BO_3	0.097
$CoCl_2$	1.463
$CuCl_2$	0.012
$NiCl_2$	0.185
Na_2MoO_4	0.149

Table S3.3: 3-(N-morpholino)propanesulfonic acid (MOPS)-buffered growth medium

Medium 3.1: succinate growth medium of 10 mM MOPS buffer

Component	Concentration (mM)
MOPS	10
NH_4Cl	50
KH_2PO_4	3.7
$MgSO_4$	1
Sodium succinate	40
$FeSO_4$	7.2×10^{-3}

The above recipe has been used in Figure 3F, S2, S3, S4.

Medium 3.2: succinate growth medium of 100 mM MOPS buffer

Component	Concentration (mM)
MOPS	100
NH_4Cl	50
KH_2PO_4	3.7
$MgSO_4$	1
Sodium succinate	40
$FeSO_4$	7.2×10^{-3}

Table S3.4 Compare the spatial and temporal performances of pH gradients in this work and previous literatures

Gradient system	Method of generation	Width of gradient [a]	Range of gradient [b]	Slope of gradient [c]	Spatial resolution [d]	Response time [e]	Temporal resolution [f]	Biocom-patible	Ref.
Chamber Systems	Diffusion	600 μm	8.6 ~ 9.3	0.001 pH/μm	~5 μm	1 ~ 2.5 hr	N.A.[k]	Yes	11
Microfluidic device	Diffusion	0.9 mm	5 ~ 9	0.004 pH/μm	N.A.[h]	N.A.[j]	N.A.[k]	Yes	10
Microfluidic device	Diffusion	~500 μm	4 ~ 10	0.01 pH/μm	N.A.[h]	N.A.[j]	N.A.[k]	Yes	9
Microfluidic device	Diffusion	500 μm	3.8 ~ 5.4, 6 ~ 7.6, 8.2 ~ 9.8	0.003 pH/μm	N.A.[h]	~2 min	1 min	Yes	8
Microfluidic device	Diffusion and convection	200 μm	6.6 ~ 8.5	0.001 pH/μm	N.A.[h]	N.A.[j]	60 min	Yes	7
Isoelectric focusing	Convection	4 cm	4 ~ 5, 5 ~ 6, 7 ~ 8, 8 ~ 9	0.3 pH/cm	~1 cm	~3 hr	N.A.[k]	Yes	6
Aerosol microdroplets	Electrostatic repulsion	~20 μm	7 ~ 11	0.2 pH/μm	~5 μm	N.A.[j]	N.A.[k]	N.A.[l]	5
Indium tin oxide electrode	Electrochemi stry	25 mm [g]	4.5 ~ 7.5	N.A.[h]	~100 μm	~70 sec	~8 sec	Yes	4
Complementar y metal-oxide semiconductor	Electrochemi stry	80 ~ 1280 μm	5 ~ 7	0 ~ 0.02 pH/μm	80 μm	~10 sec	~10 sec	Yes	3
Interdigitated electrodes	Electrochemi stry	10 or 50 μm	5.5 ~ 7.2	0 ~ 0.02 pH/μm	0.65μm	~10 sec	2.7 sec	Yes	This work

[a] The distance between the points of maximum and minimum pH.

[b] Minimum pH to maximum pH.

[c] (Maximum pH – minimum pH)/width.

[d] The closest distance between two points where pH values was measured.

[e] The time to form a stable pH gradient.

[f] The interval time between two measurements of pH values.

[g] The width of the reactor for the case that the pH map wasn't measured.

[h] Not available. The local pH values weren't reported.

[i] Not available. The closest distance between two points where pH values was measured wasn't reported.

[j] Not available. The time to form a stable pH gradient wasn't reported.

[k] Not available. The temporal measurement of pH values wasn't reported.

[l] Not available. The biocompatibility was not evaluated.

Supplementary Figures

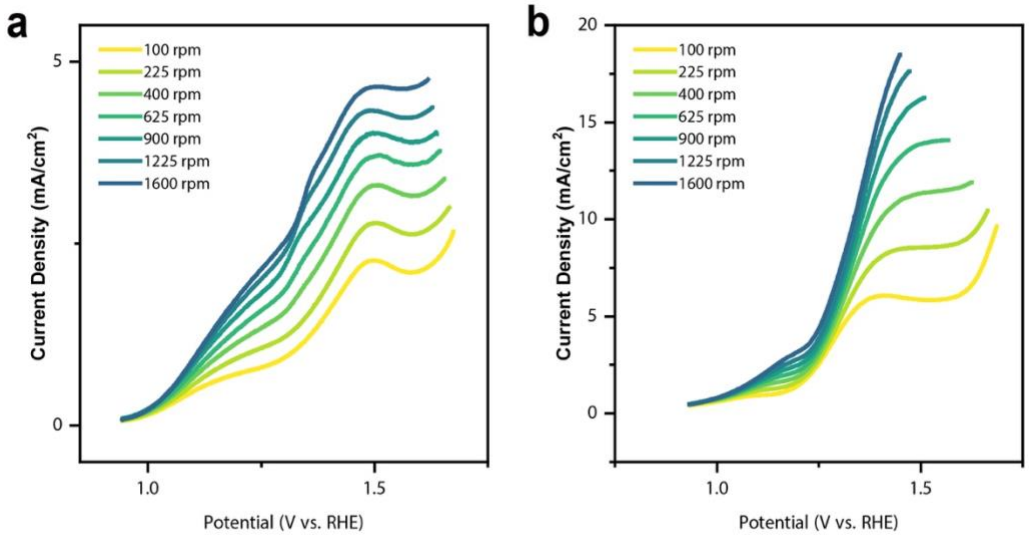


Figure S3.1. Linear sweep voltammetry of BQDS and DHBS on rotating disk electrode. a The linear scanning voltammetry of BQDS with different rotating speeds. **b** The linear scanning voltammetry of BQDS with different rotating speeds.

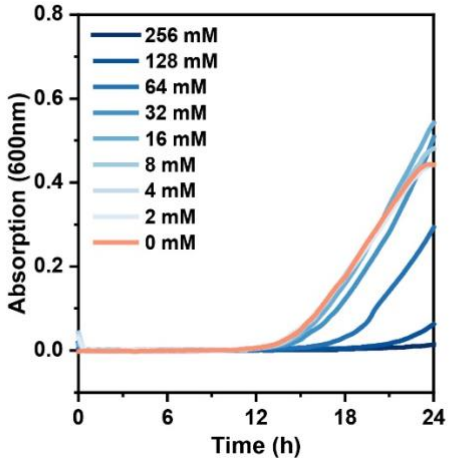


Figure S3.2. The determination of minimum inhibition concentration of DHBS for *P. aeruginosa* PA14. Growth curves of strain PA14 under different concentrations of DHBS. 96-well plate by plate reader.

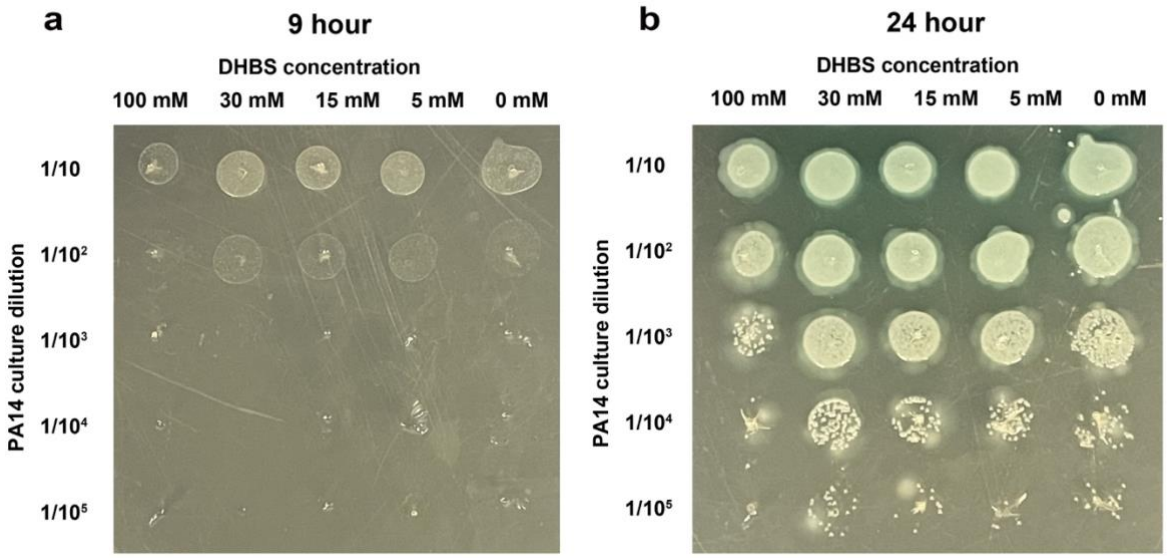


Figure S3.3. Half-maximal inhibitory concentration measurement of DHBS for PA14. The agar plate spot assay of PA14 with different DHBS concentration after cultured for **a** 9 hours and **b** 24 hours at 30 °C.

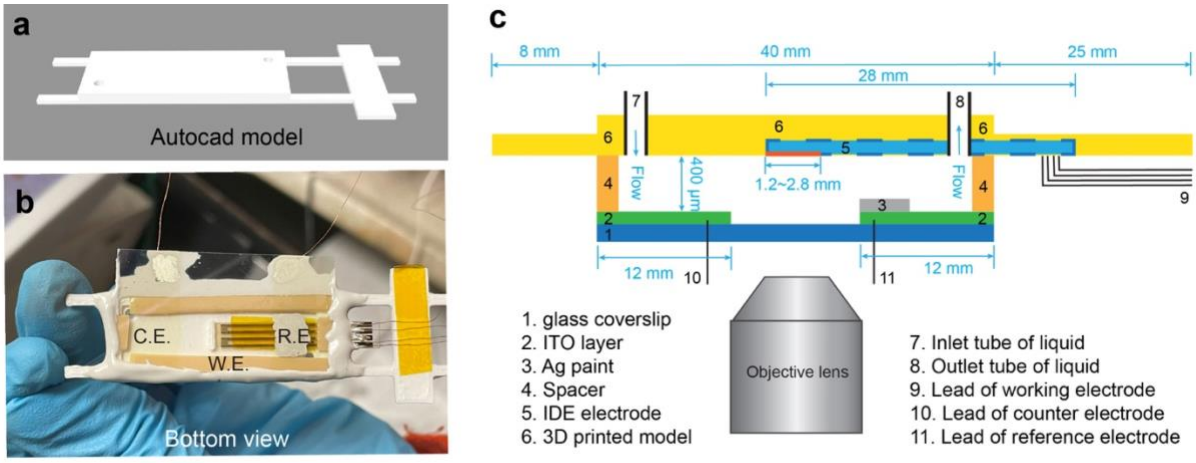


Figure S3.4. Photos of the flow device for the imaging of a confocal microscope. a 3D model of the cap of the flow device using AutoCAD. **b** Bottom view of the flow device. **c** Cross-sectional scheme of the electrochemical flow device. The objective lens is in a setting of an inverted confocal laser scanning microscope. W.E., gold interdigitated electrode (IDE); C.E., counter electrode; R.E., reference.

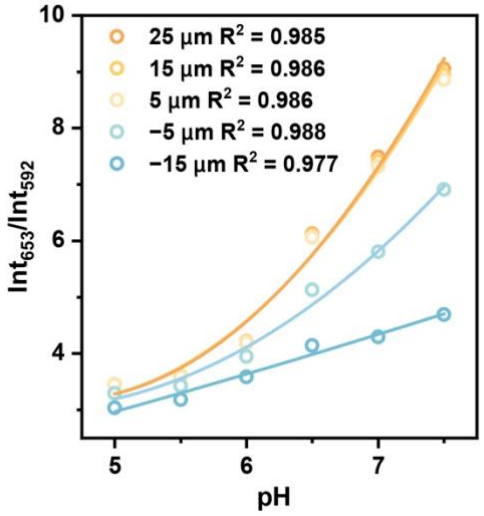


Figure S3.5. pH calibration at different *z* planes in the microfluidic device measured under confocal microscope. The ratio of fluorescent emission intensities of C-SNARF-4 between 653 and 592 nm (Int_{653}/Int_{592}) in homogenous solutions of pre-set pH values were measured by a confocal microscope. The plane of $z = 0$ μm was aligned to be the substrate plane of the IDEs. The relationship between Int_{653}/Int_{592} and pH follows a second-order polynomial fitting, used as a calibration curve, when $z \geq 5$ μm . Medium 2.2 in Table S3.2.

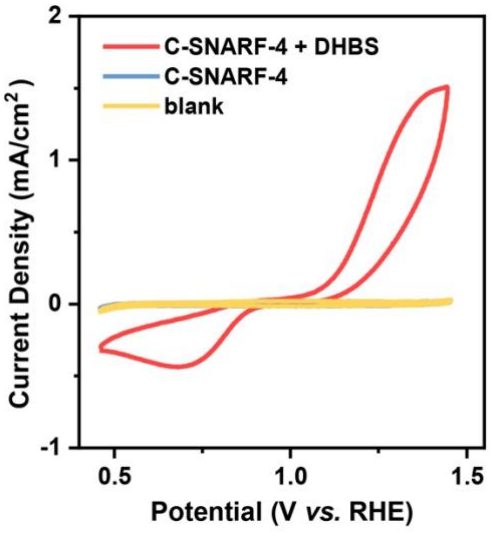


Figure S3.6. Cyclic voltammograms to assess the redox behavior of C-SNARF-4. Red, 10 μM of C-SNARF-4 and 5 mM DHBS in 1× PBS solution (medium 1.1 in Table S1); blue, 10 μM of C-SNARF-4 in 1× PBS solution; yellow, blank solution of 1× PBS solution. Minimal redox features were observed from C-SNARF-4 and the electrochemical PCET process from DHBS was not altered in the presence of C-SNARF-4. 2-mm diameter Au working electrode, 100 mV/s, in ambient air.

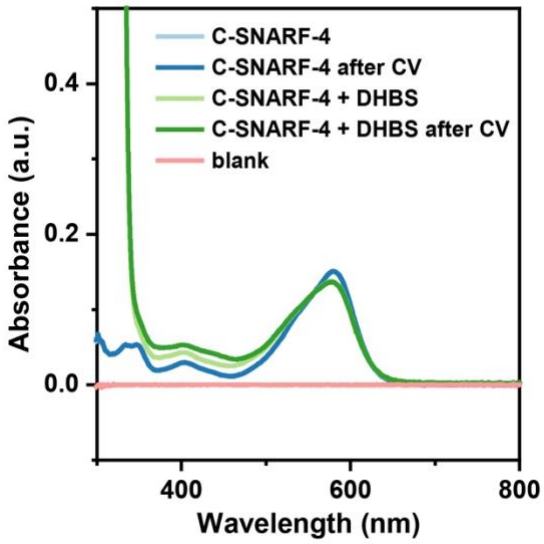


Figure S3.7. UV-Vis absorption spectra of C-SNARF-4 before and after electrochemical testing. Light blue, 10 μM of C-SNARF-4 in 1× PBS solution (medium 1.1 in Table S1) before 20 cycles of cyclic voltammetry; blue, 10 μM of C-SNARF-4 in 1× PBS solution after 20 cycles of cyclic voltammetry; light green, 10 μM of C-SNARF-4 and 5 mM DHBS in 1× PBS solution before 20 cycles of cyclic voltammetry; green, 10 μM of C-SNARF-4 and 5 mM DHBS in 1× PBS solution after 20 cycles of cyclic voltammetry; green; pink, blank solution of 1× PBS solution. The optical properties of C-SNARF-4 didn't change significantly before and after electrochemical testing, whether in the presence or absence of DHBS. 2-mm diameter Au working electrode; 20 cycles of cyclic voltammetry, 0.47 ~ 1.47 V vs. RHE, 100 mV/s, in ambient air.

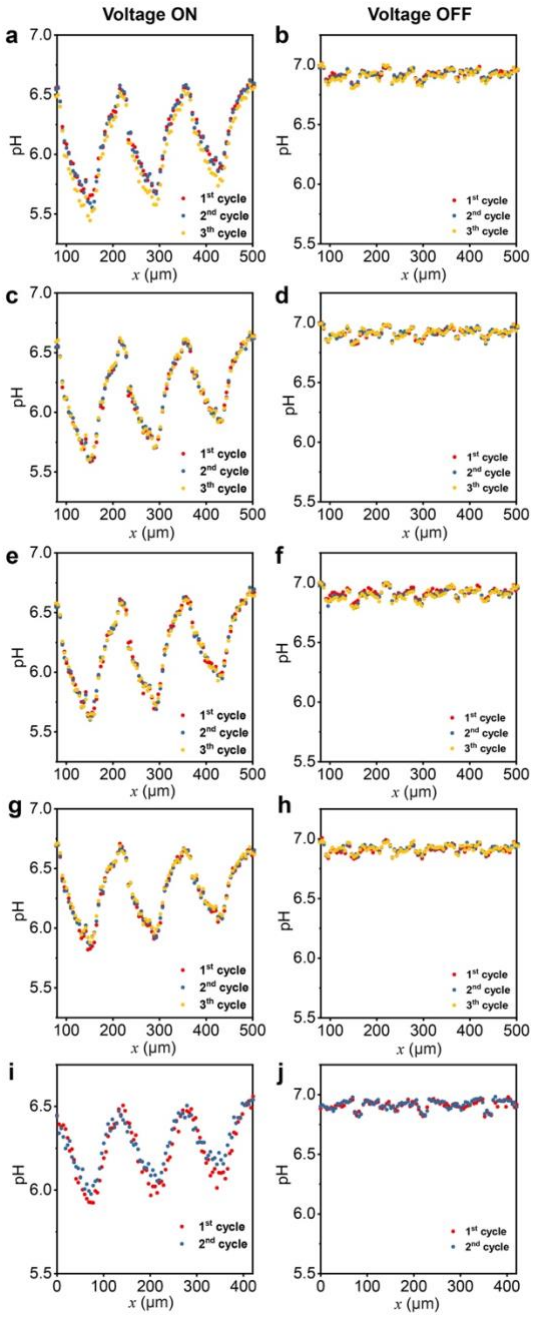


Figure S3.8. The repeatability of the spatial pH profiles generated under oscillating E_{appl} values. The spatial pH profile normal to the IDEs (*x* direction, akin to Fig. 4D and 3E) under oscillating E_{appl} values with the periodicities of 2 minutes (**a**, **b**), 6 minutes (**c**, **d**), 10 minutes (**e**, **f**), 20 minutes (**g**, **h**), and 30 minutes (**i**, **j**). The left panels depict the pH profiles when electrochemical potentials were applied (E_{ox} = 0.27 V, E_{red} = 1.47 V *vs*. RHE), while the right panels are the pH profiles under open circuit potential. The red, blue, and yellow traces represent the first, second, and third time of the oscillation and the corresponding pH spatial profiles.

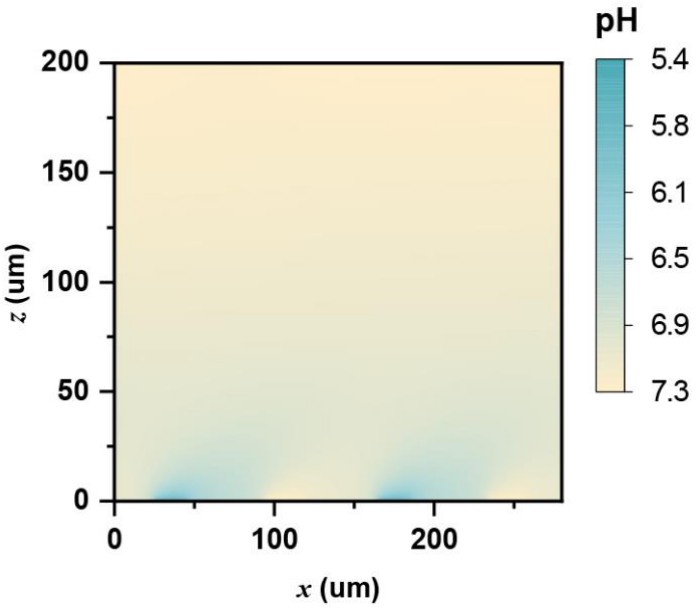


Figure S3.9. The pH gradient in the *x*-*z* plane numerically calculated by the COMSOL model. E_{red} = 0.27 V and E_{ox} = 1.47 V *vs.* RHE; fluidic flow rate, 0.1 mL/min; medium 1.2 in Table S1 (pH = 7.2).

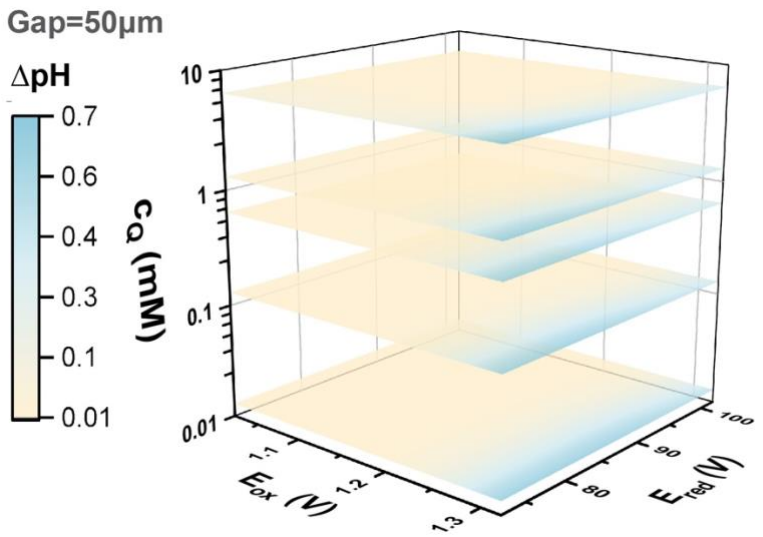


Figure S3.10. ΔpH, the difference between pH_{red} and pH_{ox}, numerically calculated as a function of multiple parameters including E_{red}. Owing to the presence of both hydroquinone and quinone in the system, the numerical simulation further denotes the concentration of the hydroquinone and quinone as C_{H_2Q} and C_Q, respectively. Here we calculate how ΔpH is dependent on C_Q and the electrode potentials (E_{ox} and E_{red}, *vs.* RHE) when C_{H_2Q} = 15 mM. d = 50 μm; flow rate, 0.1 mL/min.

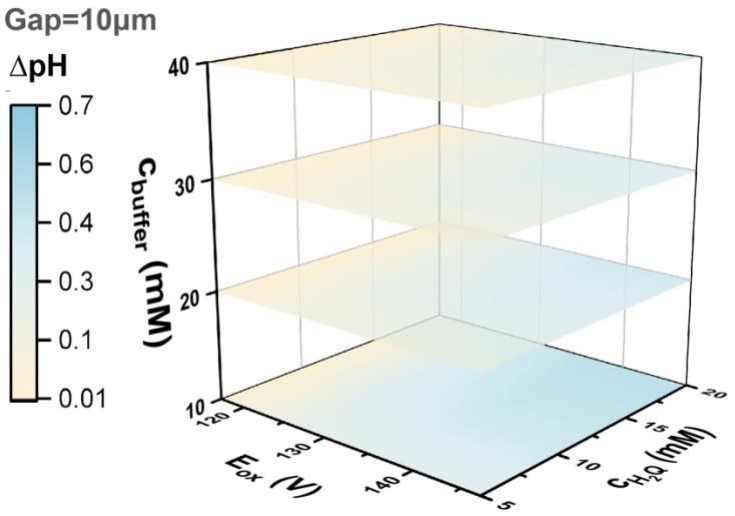


Figure S3.11. ΔpH, the difference between pH_{red} and pH_{ox}, numerically calculated as a function of multiple parameters with a smaller *d* value. Owing to the presence of both hydroquinone and quinone in the system, the numerical simulation further denotes the concentration of the hydroquinone and quinone as C_{H_2Q} and C_Q, respectively. Here we calculate how ΔpH is dependent on C_{H_2Q}, the electrode potential E_{ox} (*vs.* RHE), and the phosphate buffer concentration C_{buffer} when $C_Q = 1\times10^{-6}$ mM. $d = 10$ μm; flow rate, 0.1 mL/min.

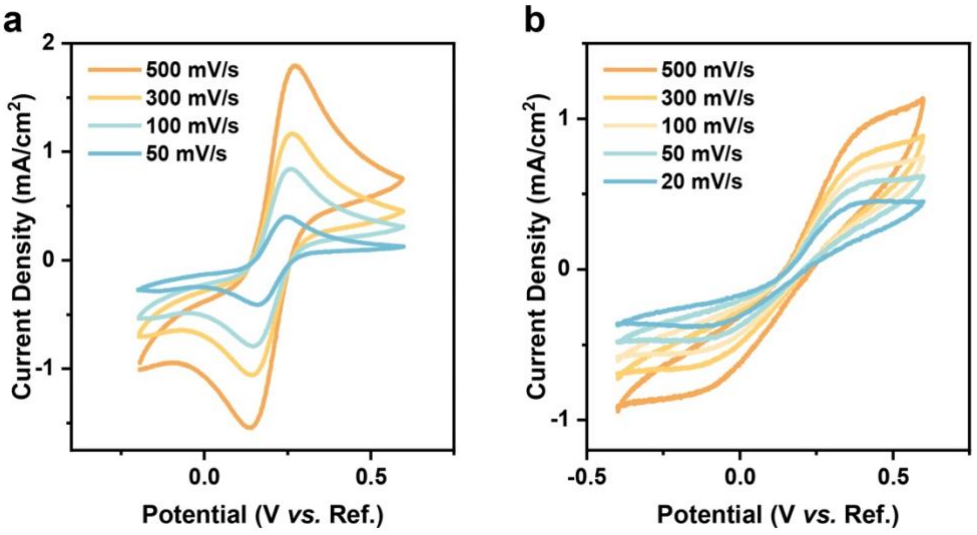


Figure S3.12. Calibration of the reference electrodes deployed in this study. a Cyclic voltammograms of Pt working electrode in Zobell solution[12] with the use of commercial Ag/AgCl (1M KCl) reference electrode. Pt wire, counter electrode. The reference electrode's potential was determined to be 0.227 V vs. RHE. **b** Cyclic voltammograms of Au IDEs as the working electrode in Zobel solution with the use of Ag-paste reference electrode. ITO, counter electrode. The reference electrode's potential was determined to be 0.270 V vs. RHE.

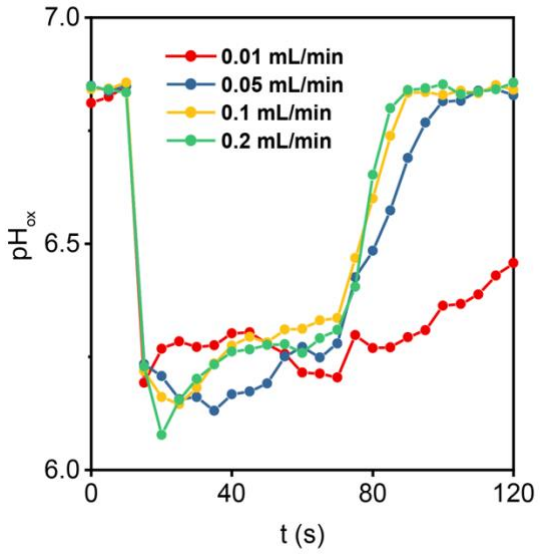


Figure S3.13. The effect of flow rate on temporal response of pH profiles. Temporal change of the local pH near the anode (pH_{ox}) under different flow rates (mL/min) and the corresponding fluidic linear velocity (μm/s). red, 0.01 mL/min and 13 μm/s; blue, 0.05 mL/min and 63 μm/s; yellow, 0.1 mL/min and 125 μm/s; green, 0.2 mL/min and 250 μm/s. Fast temporal pH response was observed at all flow rates except the slowest one (0.01 mL/min).

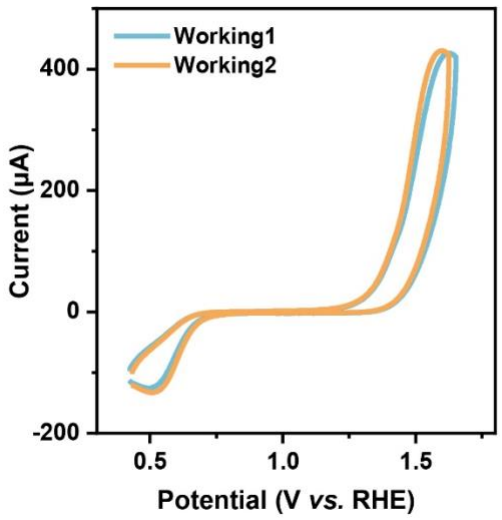


Figure S3.14. Cyclic voltammetry (CV) of DHBS on gold interdigitated electrode (gap =10 µm). The two working electrodes (blue and orange) in the same pair of interdigitated electrode are shown here. Reference: Ag paste (270 mV); Counter: ITO glass; flow device, 0.1 ml/min; DHBS: 20 mM; 10 mM phosphate-buffered succinate medium; C-SNARF-4 dye: 10 µM., after iR correction.

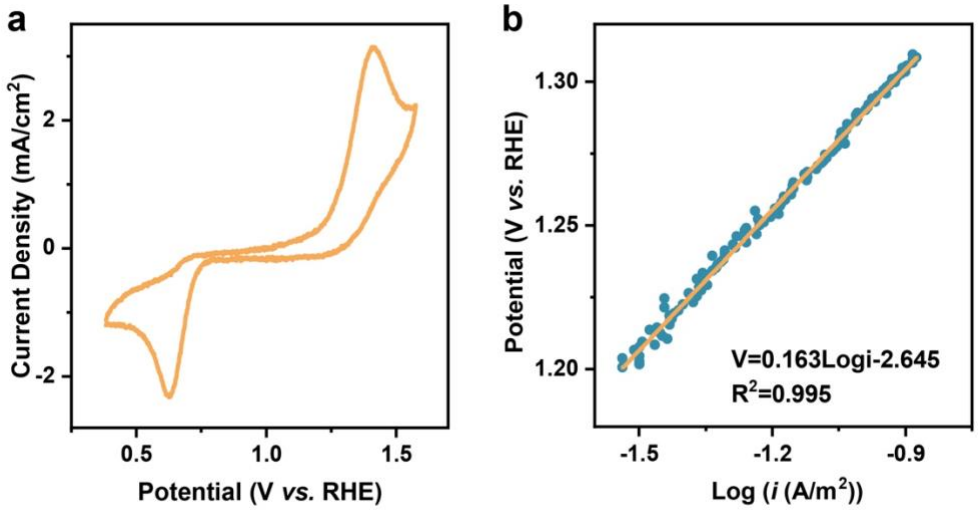


Figure S3.15. Extracting exchange current density of Au electrode for numerical simulation. **a** Cyclic voltammogram of 5 mM DHBS on Au disk electrode (2 mm diameter). 500mV/s, medium 1.1 in Table S1. The equilibrium potential of DHBS was calculated as 1.02 V *vs.* RHE by the mean of anodic and cathodic peak potentials. **b** The corresponding Tafel analysis in the voltage range between roughly 1.2 and 1.3 V *vs.* RHE. The exchange current density i_0 in the Method session was determined as 2.27×10^{-3} A/m^2 based on the Tafel analysis.

Supplementary References

1. Liu, F., Kolesov, G. & Parkinson, B.A. Preparation, applications, and digital simulation of carbon interdigitated array electrodes. *Anal. Chem.* **86**, 7391-7398 (2014).
2. Rosenberg, B., Van Camp, L. & Krigas, T. Inhibition of cell division in *Escherichia coli* by electrolysis products from a platinum electrode. *Nature* **205**, 698-699 (1965).
3. Jung, H.S. et al. CMOS electrochemical pH localizer-imager. *Sci. Adv.* **8**, eabm6815 (2022).
4. Fomina, N. et al. An electrochemical platform for localized pH control on demand. *Lab Chip* **16**, 2236-2244 (2016).
5. Wei, H. et al. Aerosol microdroplets exhibit a stable pH gradient. *Proc. Natl. Acad. Sci. U.S.A.* **115**, 7272-7277 (2018).
6. Hausfeld, A.D. Isoelectric focusing: pH gradients established with simple buffers and a cation-selective membrane. *Anal. Biochem.* **212**, 237-246 (1993).
7. Kim, T., Pinelis, M. & Maharbiz, M.M. Generating steep, shear-free gradients of small molecules for cell culture. *Biomed. Microdevices* **11**, 65-73 (2009).
8. Zhuang, J., Wright Carlsen, R. & Sitti, M. pH-taxis of biohybrid microsystems. *Sci. Rep.* **5**, 11403 (2015).
9. Luo, X. et al. In situ generation of pH gradients in microfluidic devices for biofabrication of freestanding, semi-permeable chitosan membranes. *Lab Chip* **10**, 59-65 (2010).
10. Kirchhof, K. et al. Polyelectrolyte multilayers generated in a microfluidic device with pH gradients direct adhesion and movement of cells. *Lab Chip* **11**, 3326-3335 (2011).

11. Nawa-Okita, E., Nakao, Y., Yamamoto, D. & Shioi, A. A molecular assembly machine working under a quasi-steady state pH gradient. *Bull. Chem. Soc. Jpn.* **93**, 604-610 (2020).

12. Nordstrom, D.K. Thermochemical redox equilibria of ZoBell's solution. *Geochim. Cosmochim. Acta* **41**, 1835-1841 (1977).

Chapter 4. Concluding Remarks

The work I have presented in this dissertation highlights my work throughout my graduate student career in electrochemical control of concentration gradients with high spatiotemporal resolution. Throughout my graduate studies, I have demonstrated the utility of electrochemical techniques in generating controllable gradients of various biomolecules, thereby facilitating a deeper understanding of bacterial responses to both static and dynamic local environments.

Our work has effectively utilized electrochemical catalysis to establish and program concentration profiles of O_2 and H_2O_2. We demonstrated a machine learning-based inverse design approach for tailoring these gradients to desired conditions and validated this concept through a closed-loop protocol with custom microwire electrodes. This approach has achieved concentration differences and spatial resolutions well-suited for microbiological research. The inverse design framework developed could be further adapted to other electrochemical systems that are compatible with neural network analysis.

In addition, we have achieved a novel modulation of spatiotemporal pH environments using a quinone/hydroquinone redox couple, specifically designed to be compatible with biological systems and orthogonal to other biological molecules. This system allows for precise electrochemical control of local pH within a microfluidic channel featuring interdigitated electrodes. Our approach achieves pH gradients within biologically relevant ranges with superior spatial and temporal resolution compared to existing methods. This platform demonstrates the ability to control pH profiles with high precision, offering a robust tool for perturbing extracellular pH microenvironments at the single-cell level.

Looking ahead, several promising directions emerge for future research. One avenue involves

exploring bacterial responses to the finely tuned gradients generated by our electrochemical platforms. Investigations into spatial gradients could include studying phenomena such as chemotaxis, where bacterial movement is directed by gradient shapes, or examining the interplay between aerobic and anaerobic respiration in varying O_2 gradients. Temporal changes in the microenvironment could also be studied, particularly how bacteria respond to sudden perturbations or oscillations in pH or O_2 concentration. The rapid kinetics of our electrochemical systems permit high-resolution temporal studies, potentially revealing new insights into bacterial adaptation and metabolic shifts.

Future research could also extend these electrochemical designs to other biomolecules, such as signaling molecules like NO or extracellular metabolites. Designing controllable gradients for these substances could further elucidate the complex interactions between microbial cells and their microenvironments, advancing our understanding of these systems with unprecedented precision.